

EVOLUTION OF INTRINSIC POINT DEFECTS IN FLUORITE-BASED MATERIALS:
INSIGHTS FROM ATOMIC-LEVEL SIMULATION

By

DILPUNEET SINGH AIDHY

A DISSERTATION PRESENTED TO THE GRADUATE SCHOOL
OF THE UNIVERSITY OF FLORIDA IN PARTIAL FULFILLMENT
OF THE REQUIREMENTS FOR THE DEGREE OF
DOCTOR OF PHILOSOPHY

UNIVERSITY OF FLORIDA

2009

© 2009 Dilpuneet S. Aidhy

To my parents with love and gratitude

ACKNOWLEDGMENTS

At this very juncture of my life, where I now bridge my educational and professional career, I want to take this opportunity to thank some very important people who have made my PhD a wonderful journey.

I express my deepest gratitude towards my mentor Prof. Simon Phillpot, whose advising skills, besides scientific knowledge, I find to be exceptional. His enthusiasm towards science, trust and patience with students blended with a great sense of humor has made my PhD thoroughly enjoyable. He has always provided liberty to explore things even not directly related to research and has shared his wisdom. I feel fortunate to have him as an advisor, responsibility of which, he fulfilled perfectly.

I also want to thank Dr. Dieter Wolf with whom I have had many thought-provoking discussions from which this thesis has benefited immensely. I have never met a more humble person than him. I admire his love for nature and thank him for stimulating me to explore western US. I also thank Dr. Paul Millet, Dr. Tapan Desai and Srujan, with whom I enjoyed our collaborative work on nuclear materials. Thanks to the friends I made in Idaho, their generosity and warmth softened the blow of Idaho winters.

Many thanks to my committee members, Profs. Susan Sinnott, Juan Nino, Eric Wachsman and Jason Weaver for serving on my committee and providing valuable suggestions to my research work. Special thanks to Prof. Sinnott for co-advising me, Prof. Nino for teaching me crystallography and Prof. Wachsman for keeping me honest from experimental standpoint.

I want to mention some of the very dear friendships that I feel fortunate to have developed during the years. Special thanks to Tabassum for giving me moral support especially during the semester-ending result times, Rakesh for his always-welcome attitude and

exceptionally delicious food, and Sankara for being a perfect roommate. Besides, all current and past members of the Sinpot group, thanks also to Priyank, Chan-Woo, Taku, Peter and Tao. All of you did bear me very kindly.

In the end, I want to mention my dad and my mom, to thank whom I do not have enough words. They have been the supporting pillars of my life and have never let the distance of seven seas interfere in keeping their warmth of love around me. I am indebted to you, dad, especially for letting me to pursue a degree in the US, exactly a month after you underwent heart surgery, and you mom, for being especially strong during that time. I do not want to forget my little sister who throughout these years looked forward more to souvenirs than me.

It would be inappropriate to not to thank the Almighty for making this journey easy and fruitful.

TABLE OF CONTENTS

	<u>Page</u>
ACKNOWLEDGMENTS.....	4
LIST OF TABLES.....	10
LIST OF FIGURES	11
ABSTRACT	15
 CHAPTER	
1 GENERAL INTRODUCTION	17
1.1 Sources of Energy	17
1.2 Energy and Environment	19
1.3 Clean Technology	20
1.4 Challenges in Materials Science	22
1.5 Motivation for This Work	23
1.6 Significance of Simulation	24
1.7 Objective of This Work	25
1.8 Organization of Dissertation	26
2 DEFECTS IN SOLIDS	27
2.1 Introduction	27
2.2 Intrinsic Point Defects	27
2.2.1 Frenkel Defect	28
2.2.2 Schottky Defect	29
2.2.3 Thermodynamics of Point Defects: Equilibrium Concentration	29
2.3 Transport.....	32
2.3.1 Atomistic Theory of Diffusion	32
2.3.2 Diffusion Mechanisms	34
2.3.2.1 The vacancy mechanism	34
2.3.2.2 The interstitial mechanism	34
2.3.2.3 The interstitialcy mechanism	35
2.4 Crystallography of Materials.....	36
2.4.1 Fluorite Crystal Structure: δ -Bi ₂ O ₃ and UO ₂	36
2.4.2 Rocksalt Crystal Structure: MgO	37
2.4.3 Space Group $Fm\bar{3}m$	37
2.4.4 Body-Centered Cubic: Space Group $Im\bar{3}m$	39
3 SIMULATION METHODOLOGY	40
3.1 Simulation Methodologies	40
3.2 Molecular Dynamics Simulation	41

3.3	General MD Algorithm	41
3.4	Periodic Boundary Condition	44
3.5	Interatomic Interactions	45
3.5.1	Long-range Interactions	47
3.5.2	Short-Range Interactions	53
3.5.3	Electronic Polarizability – Shell Model	55
3.5.4	Thermodynamic Conditions (ensemble) for Materials Simulation	56
4	IONIC CONDUCTIVITY OF SOLID-OXIDE FUEL CELL ELECTROLYTE.....	58
4.1	Fuel Cell	58
4.2	Solid Oxide Fuel Cell	59
4.3	Fluorite-Based Cubic Bismuth Oxide.....	61
4.3.1	A Model Material	61
4.3.2	δ -Bi ₂ O ₃ Limitations	63
4.3.3	Ionic Radii or Polarizability?.....	64
4.4	Simulation Methodology	66
4.5	Results.....	67
4.5.1	Polarizability Indeed	67
4.5.1.1	Polarizable and non-polarizable ions.....	69
4.5.1.2	Only-oxygen ions polarizable	71
4.5.1.3	Only-bismuth ions polarizable	72
4.5.2	Oxygen Diffusion Mechanism.....	73
4.6	Discussion.....	75
5	VACANCY-ORDERED STRUCTURE OF CUBIC BISMUTH OXIDE	77
5.1	Introduction	77
5.2	Ordering of the Vacancies: MD Simulation.....	80
5.2.1	Neighboring Vacancies of a Vacancy	81
5.2.2	Continuous Ordered Structure of Vacancies	83
5.2.3	Expansion and Contraction of the Tetrahedron.....	85
5.3	Density Functional Theory (DFT) Calculations of the Structure of Bi ₂ O ₃	86
5.3.1	DFT Methodology	86
5.3.2	Vacancy Ordering.....	87
5.3.3	Bonding and Charge Distribution.....	88
5.3.4	Electronic Structure of Vacancy-Ordered δ -Bi ₂ O ₃	91
5.4	Discussion.....	93
6	CRYSTALLOGRAPHIC ANALYSIS OF THE STRUCTURE OF CUBIC BISMUTH OXIDE	94
6.1	Introduction	94
6.2	Schematic Representation of the Structure of δ -Bi ₂ O ₃	94
6.2.1	Space Group Analysis	97
6.2.2	Bond Lengths.....	99
6.2.2.1	Bond lengths from DFT calculations	100

6.2.2.2	Cation displacements in the <111> vacancy ordered oxygen sub-lattices.	100
6.2.2.3	Cation displacements in the <110> vacancy ordered oxygen sub-lattice ..	101
6.2.2.4	Anion displacement	102
6.2.2.5	Bond lengths from Shannon radii	103
6.2.2.6	Sub-unit Cell Distortion.....	103
6.2.2.7	Comparison with Bixbyite Structure.....	106
6.3	Relation to Experiment	107
6.4	Discussion.....	109
6.5	Conclusion and Outlook	110
7	RADIATION DAMAGE IN MgO	112
7.1	Nuclear Energy.....	112
7.1.1	Nuclear Power	112
7.1.2	Challenges for Materials Science	112
7.2	Radioactivity	113
7.2.1	Alpha (α) Decay	114
7.2.2	Beta (β) Decay	115
7.2.3	Gamma (γ) Decay	116
7.2.4	Neutron Capture	116
7.3	Nuclear Fission.....	116
7.4	Radiation Damage.....	117
7.4.1	Standard Radiation Damage Methodology Using MD Simulation.....	118
7.4.2	Kinetically-evolving Irradiation-induced Defects Method.....	120
7.4.3	Materials Under Study	122
7.5	Interatomic Potential and MD Simulation.....	123
7.6	Results.....	124
7.6.1	FPs Only on One Sublattice.....	124
7.6.2	FPs on Both Sublattices	125
7.7	Cluster-Formation Mechanism.....	128
7.7.1	Crystallography of the Cluster.....	130
7.8	Discussion.....	132
8	RADIATION DAMAGE IN UO ₂	135
8.1	Introduction	135
8.2	Simulation Methodology	137
8.2.1	Interatomic Potential and Molecular Dynamics Method	137
8.2.2	Diffusion-controlled Kinetic Evolution of Defects	138
8.2.3	Frenkel-pair Defects on a Single Sub-lattice	139
8.2.4	FPs on Both U and O Sub-lattices.....	142
8.2.5	Vacancy Clustering: Schottky Defects	143
8.2.6	Interstitial Clustering: Cuboctahedral Clusters	145
8.2.7	Evolution of Disproportionately Defected Systems.....	150
8.3	Discussion.....	153
9	EVOLUTION OF POINT DEFECTS IN BCC MOLYBDENUM ¹	157

9.1 Introduction	157
9.2 Simulation Methodology	158
9.3 Vacancy and Interstitial Diffusivities	159
9.4 Grain Boundaries as Sources and Sinks	161
9.4.1 Grain Boundaries as Vacancy Sources	161
9.4.2 Source-strength Analysis	164
9.4.3 Grain Boundaries as Vacancy Sinks	167
9.4.4 Grain Boundaries as Interstitial Sinks.....	169
9.4.5 Discussion on GB Source/Sink Strength	171
9.5 Frenkel-pair Annihilation	172
9.5.1 FP Annihilation by Mutual Recombination.....	172
9.5.2 Frenkel Pair Annihilation in a Nanocrystalline Structure.....	174
9.6 Conclusion.....	177
10 SUMMARY AND FUTURE WORK	178
10.1 δ -Bi ₂ O ₃	178
10.1.1 Cation Polarizability.....	178
10.1.2 Oxygen Diffusion Mechanism	178
10.1.3 Bonding.....	179
10.1.4 Crystallographic Analysis of Structure	179
10.2 MgO, UO ₂ and Mo.....	180
10.2.1 Methodology.....	180
10.2.2 MgO Interstitial Clustering.....	180
10.2.3 UO ₂ Clustering	181
10.2.4 Defect Annihilation in Nanocrystalline Mo	182
10.3 Conclusions and Future Work.....	182
10.3.1 δ -Bi ₂ O ₃	182
10.3.2 Radiation Damage.....	185
LIST OF REFERENCES	188
BIOGRAPHICAL SKETCH	197

LIST OF TABLES

<u>Table</u>	<u>page</u>
4-1 Characteristics of different fuel cells.	59
4-2 Parameters for the short-range potential for δ -Bi ₂ O ₃ from Jacobs and Mac Donail	67
5-1 Relative stability of the ordered structures in 2x2x2 system.....	88
5-2 Bi-O bond length in Bi-centered $\langle 110 \rangle$ and $\langle 111 \rangle$ vacancy-ordered oxygen sub-lattice.....	89
5-3 Electronic charge on the ionic species.	91
6-1 Space group parameters of superstructure of δ -Bi ₂ O ₃	98
6-2 Bi-O bond lengths in the $\langle 110 \rangle$ and $\langle 111 \rangle$ vacancy ordered sub-lattice	105

LIST OF FIGURES

<u>Figure</u>	<u>page</u>
1-1 World's primary energy consumption by fuel-type in year 1973 and year 2004	17
1-2 Concentration of CO ₂ in the atmosphere over the last millennium.	19
1-3 Increase in the earth temperature over the last 150 years.	20
2-1 Point defects.	28
2-2 Point defects in ionic materials.	28
2-3 Diffusion by vacancy mechanism.	34
2-4 Diffusion by interstitial mechanism.....	35
2-5 Diffusion by interstitialcy mechanism.....	35
2-6 Fluorite crystal structure.	36
2-7 Rocksalt crystal structure.....	37
2-8 Three different symmetry operations.....	38
2-9 Body-centered crystal structure.....	39
3-1 Two-dimensional periodic system of a simulation cell	44
3-2 Inter-ionic potential between Zr ⁴⁺ and O ²⁻	46
3-3 Total Coulombic energy	49
3-4 Charge on the truncated sphere	50
3-5 Energies of the charge-neutralized and charged systems	51
3-6 Exact Madelung energy and approximate Madelung energy	51
3-7 Damped charge-neutralized and undamped charge-neutralized energy	52
4-1 Working of a SOFC	59
4-2 Conductivity versus temperature relationship.....	60
4-3 Fluorite crystal structure.	62
4-4 Relative conductivity of δ-Bi ₂ O ₃ doped with different dopants.....	65

4-5	Comparison of time constant for different doped $\delta\text{-Bi}_2\text{O}_3$ systems.....	65
4-6	Ionic radius and polarizability of different dopants added in $\delta\text{-Bi}_2\text{O}_3$	68
4-7	Oxygen ion diffusion through two Bi ions	68
4-8	Gradually increasing Bi polarizability	69
4-9	MSD of oxygen in polarizable and non-polarizable $\delta\text{-Bi}_2\text{O}_3$	70
4-10	MSD of the oxygen ions with gradually increasing oxygen polarizability	71
4-11	MSD of the oxygen ions with gradually increasing bismuth polarizability	73
4-12	Possible oxygen diffusion directions	74
4-13	Oxygen diffusion mechanism.....	75
5-1	Three different models of $\delta\text{-Bi}_2\text{O}_3$	79
5-2	Vacancy-vacancy pair-distribution function	81
5-3	Ordering of vacancies	82
5-4	A continuous network of vacancies in the oxygen sub-lattice	83
5-5	2x2x2 fluorite superstructure with vacancy ordering in $\langle 110 \rangle$ and $\langle 111 \rangle$ directions.....	84
5-6	Bi-Bi pair distribution function.....	85
5-7	Tetrahedron expansion and contraction.....	86
5-8	Possible vacancy-ordering mechanisms in $\delta\text{-Bi}_2\text{O}_3$	87
5-9	Two kinds of Bi-centered oxygen sub-lattice cubes	89
5-10	Electron lone-pair charge around two different Bi-centered cubes	90
5-11	Bi-O bonds in a tetrahedra in the unit cell.....	92
6-1	The 2x2x2 fluorite-related superstructure viewed from three different planes.....	95
6-2	Layered sequence of the structure of $\delta\text{-Bi}_2\text{O}_3$ along [001] direction	95
6-3	Layered sequence of the oxygen sub-lattice along [001] in 2x2x2 $\delta\text{-Bi}_2\text{O}_3$	96
6-4	Crystallographic sites of the space group $\text{Fm}\bar{3}$	99
6-5	$\langle 111 \rangle$ vacancy ordered oxygen sub-lattice.....	100

6-6	<110> vacancy-ordered oxygen sub-lattice.....	102
6-7	Distortion in the superstructure	104
7-1	Two phases of radiation damage.....	119
7-2	Typical Frenkel pair (FP) defects during radiation damage using PKA.....	119
7-3	Evolution of FPs on Mg sublattice.....	125
7-3	Evolution of FPs on O sublattice.....	125
7-5	Evolution of FPs on both sublattices.....	126
7-6	Total number of Mg FPs present in the simulation cell.....	127
7-7	Close-up of the all-interstitial cluster.....	128
7-8	Two distinct mechanisms controlling the growth of an interstitial cluster.....	129
7-9	A (MgO) ₄ octopolar.. ..	131
7-10	Crystallography of MgO rocksalt lattice.. ..	132
8-1	β -U ₄ O ₉ crystal structure.....	136
8-2	Evolution of the point defects present only on the oxygen sub-lattice	139
8-3	Number of O FPs present when the system is initialized with three different defect conditions.....	140
8-4	Evolution of the point defects present only on the uranium sub-lattice	141
8-5	Evolution of the point defects simultaneously present on both oxygen and uranium sub-lattices	142
8-6	Schottky-defect formation	144
8-7	Three different kinds of cuboctahedral (COT) clusters	145
8-8	Progressive formation cuboctahedral (COT) cluster	147
8-9	Clustering of oxygen interstitials in the absence of vacancies.....	148
8-10	Clustering of U and O vacancies.....	149
8-11	O FP evolution in a system initially containing 200 O FPs and fixed U FPs.....	150
8-12	Number of O FPs as a function of number of initially created U FPs	152

9-1	MSD for single-crystal structures	160
9-2	Arrhenius plot for D_i and D_v	161
9-3	Vacancy population within a single $d = 20$ nm grain at $T = 2900$ K	162
9-4	Nucleation of two lattice vacancies.....	163
9-5	Evolution of the vacancy concentration in the under- and over-saturated nanocrystalline structures	166
9-6	Vacancy population in a single grain of the over-saturated sample.....	168
9-7	Oversaturated interstitial distribution.....	169
9-8	Quantification of the time evolution of the self-interstitial concentration	170
9-9	Frenkel pair distribution in a single crystal.	173
9-10	Recombination rate in a single crystal	173
9-11	Evolving nanocrystalline structures over-saturated with the FPs	175
9-12	Vacancy and interstitial concentrations for the nanocrystalline structure	176

Abstract of Dissertation Presented to the Graduate School
of the University of Florida in Partial Fulfillment of the
Requirements for the Degree of Doctor of Philosophy

EVOLUTION OF INTRINSIC POINT DEFECTS IN FLUORITE BASED MATERIALS:
INSIGHTS FROM ATOMIC-LEVEL SIMULATION

By

Dilpuneet Singh Aidhy

May 2009

Chair: Simon R. Phillpot

Major: Materials Science and Engineering

Point defects play a significant role in materials properties. On the one hand, point defects are exploited in applications such as fuel cells; on the other hand, they are deleterious to performance of in such applications as nuclear fuels. To tailor materials with desired properties, it is thus important to understand point defect behavior in materials under specific environments/applications. This thesis is focused on understanding the evolution of point defects in materials, primarily fluorite-related, used in solid oxide fuel cell (SOFC) and nuclear applications. Molecular-dynamics simulation (MD) and density functional theory (DFT) are used as materials modeling tools.

Cubic bismuth oxide (δ -Bi₂O₃) is a promising SOFC electrolyte and a fluorite-based model material, in which, it is found that while intrinsic oxygen vacancies contribute in high oxygen diffusion, under certain circumstances, they themselves act as limiting factors by forming a $\langle 110 \rangle$ - $\langle 111 \rangle$ vacancy-ordered system. It is found that high cationic polarizability plays a significant role in achieving high oxygen diffusivity. It is also found that the oxygen diffusivity may be limited due to the formation of covalent character bonds by some Bi ions.

Fluorite-structured UO₂ is the fuel in almost all operating nuclear reactors. Due to irradiation, UO₂ undergoes damage resulting in the formation of Frenkel pairs (FPs) on both

uranium and oxygen sub-lattices. It is found that, while damage on oxygen sub-lattice alone is not deleterious, in that oxygen FPs annihilate by mutual recombination, presence of FPs on uranium sub-lattice cause long-lasting damage and make UO_2 less radiation tolerant. Regardless of FPs on oxygen sub-lattice, FPs on uranium sub-lattice nucleate new O FPs, which form clusters. The oxygen vacancies' sequestration by uranium vacancies is found to be the mechanism of cluster formation.

The point-defect evolution in rocksalt MgO is also elucidated. MgO is an important engineering material and has nuclear applications. As in UO_2 , it is found that when defects are present on both Mg and O sub-lattice, new FPs, in this case, both on Mg and O are formed. Defects present only on either Mg or O sub-lattice annihilate by mutual recombination.

While UO_2 and MgO studies are done on single crystals to elucidate FPs elimination by mutual recombination only, to understand their evolution in the presence of GBs, similar studies are done on nanocrystalline Mo. This allows elucidation of dominant mechanism of point-defect elimination. It is found that for the grain size and temperature under study, mutual recombination of FPs dominates and GBs have little effect on the point-defect elimination.

CHAPTER 1 GENERAL INTRODUCTION

1.1 Sources of Energy

Availability of different forms of energy is essential for the development of an economy. Affordable energy has enabled industrialization and human development. Since industrialization, man has used different forms of energy and explored more. On the one hand, the pursuit of energy has enabled the discovery of new materials, on the other, materials have been used to produce energy and convert it from one form to another; nuclear materials and photovoltaic silicon cells are respectively two good examples. Energy and materials therefore hold a very close relationship.

There are different fuels for energy production depending on their availability and affordability, e.g., coal, oil, hydro, nuclear. Figure 1-1 gives a graphical view of the energy derived from different sources/materials over the last 30 years.¹

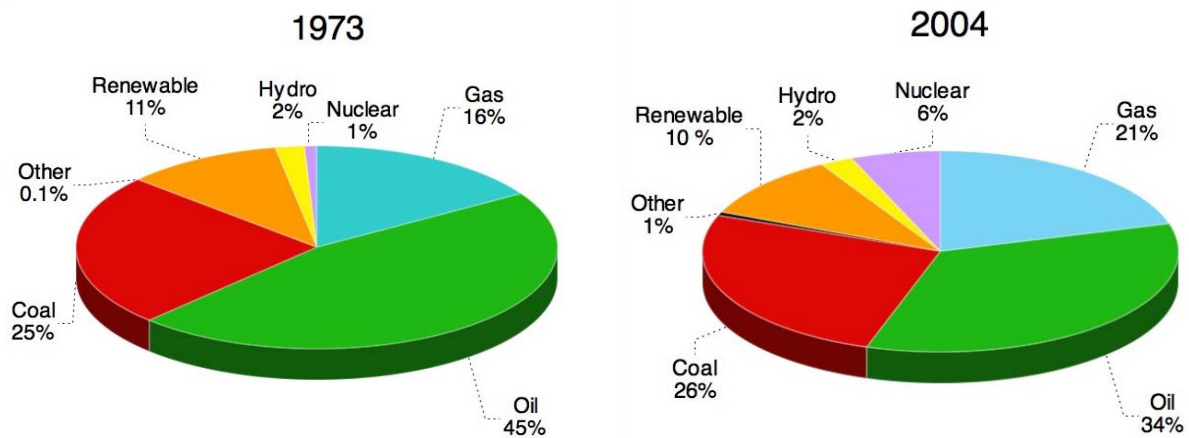


Figure 1-1. World's primary energy consumption by fuel-type in year 1973 and year 2004 (adapted from reference 1). It shows the world's significant dependence on the fossil fuels.

A comparison shows that there is only modest change of the energy consumed from one source to another. Coal and oil have been used as the major sources of energy for a

long period of time. Even now, coal continues to contribute the same share, primarily due to its widespread availability and developed infrastructure. In contrast, the dependence on oil has decreased by 10 % and the nuclear has risen by 6 %. Nevertheless, overall the graph shows that there is still significant dependence on the fossil fuels.

With fossil fuels being so indispensable, their depletion is worrisome as more countries industrialize. The energy consumption of the world has increased 20 times from year 1850 to 2000. In 2005, total energy consumption was estimated to be around 447 quads (quadrillion BTUs, or quads). If we continue to use resources at the same rate, the world is expected to run out of fossil fuels before end of the century. While coal is still expected to last for another 164 years,² other sources of energy are not so abundantly available. Uranium deposits are only sufficient for another 70-80 years.³ Similarly, with a 2% increase in production per year, the oil resources are likely to peak in the year 2016.⁴ The energy consumption is further compounded by the highly populous and fast-growing economies, in particular China and India. The demand for energy will increase tremendously as they make strides towards development. To put the energy situation into perspective, if people in these two countries were to enjoy the same transport-lifestyle as in the United States, the demand for oil would increase by 100 million barrels per day (BPD) above the present 83 million BPD.⁵ This exemplifies the enormous energy challenge that the world faces in the near future. To fulfill the energy needs of future generations, it is important to develop new methods and sources of energy production. In addition to the future energy problem, the world also faces an imminent problem of even bigger magnitude - *the challenge to maintain Earth's environment clean.*

1.2 Energy and Environment

The reliance on fossil fuels is causing long lasting damage to the environment. All combustible fossil fuels result in the production of greenhouse gases such as CO₂, CH₄ and N₂O. A major environmental concern with the emission of the greenhouse gases is entrapment of the additional energy in the environment at levels far above the pre-industrial levels. It is now widely accepted that the heat entrapment directly contributes to climate change; the most obvious effect is global warming. Figure 1-2 shows the concentration of the CO₂ in the atmosphere over the last millennium.⁶ Over the period 1000-1800, the CO₂ concentration remained virtually constant. In contrast, with the industrialization since then, the CO₂ concentration has gradually increased and is now reaching alarming concentrations.

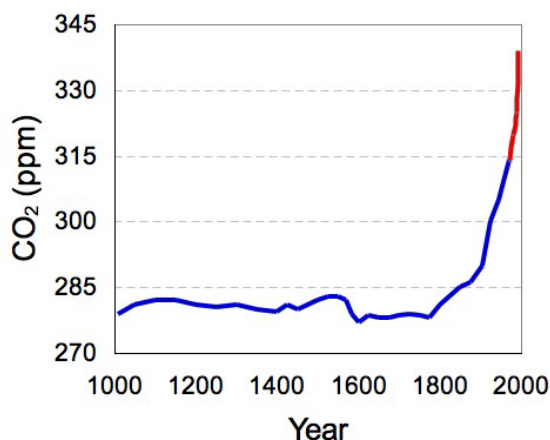


Figure 1-2. Concentration of CO₂ in the atmosphere over the last millennium. The concentration of CO₂ has increased exponentially over the last 50-100 years, matching the industrialization around the world. Red line indicates sharp increase in the last 150 years. (Adapted from reference 6)

This increase in the CO₂ concentration has led to global warming. It has been shown from various scientific studies that the earth temperature increased by 0.6 ± 0.2 °C in the 20th century.³ The plot in Figure 1-3 illustrates the increase in the temperature of

the Earth over a period of 150 years. There has been 0.2 °C increase per decade in the earth's temperature over the last 30 years. The Intergovernmental Panel for Climate Change estimates an increase of 1.8-4°C in the Earth's temperature within the next century.⁷ Another simulation study predicts that even with the greenhouse gases levels stabilized to year 2000 level, by the end of 21st century, the earth's temperature will increase by 0.5 °C.⁸ Clearly, the unchecked emissions of the greenhouse gases will severely raise sea levels and pose serious threats to people living on the coastal cities such as London, New York, Mumbai, Shanghai and other low-lying areas.

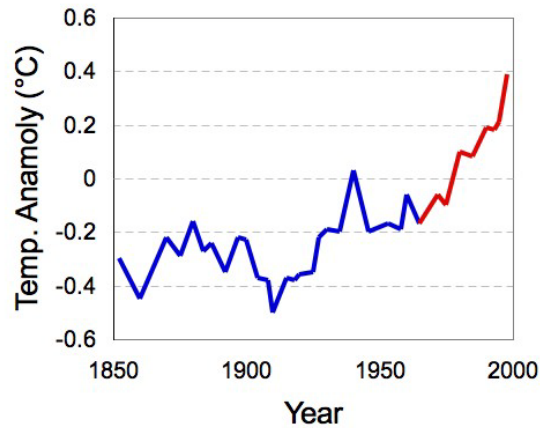


Figure 1-3. Increase in the earth temperature over the last 150 years. The increase in the temperature corresponds with the increase in the concentration of the CO₂. Red line indicates alarming increase in the last 30 years. (Adapted from reference 6)

1.3 Clean Technology

The projected impacts of CO₂ on the environment indicate that significant and immediate measures are required to save the planet from further environmental degradation. While there are measures for developing new technologies and improving upon current ones, reducing CO₂ concentration by alternative means is also among the prospective solutions. One of the proposed ways of reducing CO₂ from the environment

is its sequestration. Capturing CO₂ from industrial sites and burying it deep under the ground is being approached as a possibility. It can also be transported and stored deep under the oceans. These methods are still under consideration and some ongoing projects are in their initial stages. However, there are concerns for their success: besides the large-scale infrastructure required for such an effort, one of the key concerns is the long-term stability of CO₂ underground. Quite possibly, if the sequestered CO₂ reservoir breaks and CO₂ makes its way to the surface of earth, being heavier than air, it can displace oxygen from the surface.⁹ There are also concerns over the impacts to the marine life if CO₂ were to be stored deep inside the ocean.¹⁰ Research is still going on to make CO₂ sequestration a realizable prospect.

Current environmental demands, on the one hand, require a limited or diminishing use of the fossil fuels; ever-increasing energy demands on the other, entail development of environmental-friendly new feasible methods of energy production. A swift transition from the current energy system to an efficient and environment friendly one will require multiple technological advances. Some of the possible technologies are nuclear fission, solar, hydro, wind, natural gas, fuel cells. Some of these technologies have been used for a long period of time, while others are relatively new. However, by no measure are any of these capable of carrying the weight of the economy as a whole, some due to lack of availability while others due to their drawbacks. Nuclear fission provides high power density and small waste volume but the potential for groundwater contamination and nuclear accidents is worrisome. Solar photovoltaics have no significant air pollution but can lead to land competition. Hydropower has a sustainable energy supply but it can impact fish habitat and lead to loss of terrestrial habitat. Geothermal energy has no

significant air pollution; however, there can be potential impacts from brine disposal. Only a judicious use of the each will ensure that in pursuit of more energy and reducing greenhouse emission, they do not harm the environment significantly. We can say that driven by the huge energy demands, all of the technologies will have to advance simultaneously.

1.4 Challenges in Materials Science

Technological advancement in all these areas poses formidable challenges for materials science. If fossil fuels remain the most important sources of energy before other sources take the forefront, CO₂ levels have to be controlled. In industry, the CO₂ can be absorbed by materials and released during regeneration so that it can be sequestered underground. Amines are one class of promising materials; development of other low cost, more efficient materials is required.¹¹ To take advantage of wind energy, development of stronger and lighter materials for wind turbine blades is required. Currently, the blades are made of fiber composite materials. Off-shore installation requires much stronger materials that can withstand severe environmental conditions. Some of the other challenges are, providing sufficient stiffness to blades to prevent them from deflection, adequate fatigue life under variable wind load and prevention from bucking fracture.¹² Similarly, challenges lie ahead for the photovoltaics, which are very promising renewable sources of energy. Increased cell efficiency and reduced manufacturing costs are the foremost; application of thin films instead of silicon to reduce overall cost. Devices that can work for much larger wavelengths of sunlight spectrum are also needed for the realizing solar power as a dependable source of energy.¹³ Hydrogen is being looked as another major energy carrier in the future. However, to realize a hydrogen economy, better materials for transport through pipes,

storage without loss, easy accessibility, lightweight materials for car-fuel tanks, and efficient conversion of hydrogen into electricity are required. Improvement in the storage capacity of the batteries and faster recharging capability are also materials challenges in the battery industry. There are also significant challenges for the fuel-cell industry including high efficiency, longer lifetime comparable to that of the vehicle, reducing losses. Nuclear fission processes are very good energy producers but challenges lie for the safe and longtime storage of the nuclear wastes, the reuse of the spent fuel, and lower installation costs.

1.5 Motivation for This Work

There is extensive ongoing research in all the above-mentioned fields. (*For a review please see reference 14*). The research in this thesis is centered on two energy-related fields: solid oxide fuel cells (SOFCs) and nuclear materials. In particular, the focus is on understanding fundamental mechanisms in the evolution of the intrinsic point defects that play key role in materials performance.

Defects in materials play a very significant role in determining the properties of the materials. On the one hand, they can be deleterious to the strength of materials, whereas on the other, they can be useful in tailoring the materials' properties to desired performance. The advantages of the defects can be observed in the functioning of the SOFCs. The high diffusivity of the oxygen vacancies (point defects) in the electrolyte material is one of the keys in achieving high ionic conductivity, which is important for good power density. In contrast, due to certain structural (atomistic and electronic) changes, the oxygen diffusivity can be limited. To avoid such structural changes, it is therefore important to understand the fundamental mechanisms that lead to them.

In nuclear reactors, the point defects are highly deleterious as they damage the materials and its performance. UO_2 is used as a fuel in nuclear reactors. It is damaged under extreme environments by the irradiating particles, thus creating point defects. Severe damage due to high concentration of the point defects can limit the time of the fuel in the nuclear reactor. In order to enhance the radiation tolerance of UO_2 , the fundamental mechanism of damage, i.e., point-defect evolution under different conditions needs to be understood.

The challenges in materials science lie over various length scales; in this thesis, they are attacked from the atomistic scale (using computer simulation).

1.6 Significance of Simulation

Atomistic simulations play a significant role in complementing experiments by revealing mechanisms that are either interconnected and not easy to disentangle, or are not accessible on the experimental length and time scale. For example, dopants added to stabilize cubic phase of Bi_2O_3 lower its ionic conductivity, which ultimately reduces power density. The dopants have different atomic radii and ionic polarizability than the host cation (Bi). Experimentally, it is not clear if the conductivity decrease is due to the difference in the radii or the ionic polarizability of the dopant. Using atomistic simulations, artificial dopants can be created, in which the ionic polarizability can be varied while keeping the atomic radii constant and vice-versa. The dependence of ionic conductivity on polarizability or radii can then be disentangled.

In a nuclear reactor, irradiation events take place on a very short time scale (~nanoseconds); capturing them on the experimental time scale is not possible. Atomistic simulations are very helpful in not only capturing those events but are also capable in revealing the fundamental mechanisms of irradiation-induced processes.

Another exemplification of atomic simulation can be seen in understanding the role of the grain boundaries (GBs). It has been suggested that nanocrystalline materials are more radiation tolerant than their bulk counterparts.¹⁵ The point defects formed due to irradiation are eliminated by two mechanisms (1) by vacancy-interstitial recombination, (2) elimination at the GBs. Not only do these mechanisms occur a very short time scale but also take place simultaneously. Using simulations, it is possible to disentangle them and reveal the dominant mechanism between the two. In the following chapters the above examples are discussed in more detail.

1.7 Objective of This Work

This work is focused on understanding the evolution of the intrinsic point defects in three ceramic materials Bi_2O_3 , UO_2 and MgO , and one metallic material Mo. While to some extent, point defects are advantageous in fuel-cell electrolyte materials, they are certainly disadvantageous in nuclear materials. The objective of this work is to understand the fundamental materials' responses to point defects, thus revealing the conditions under which materials lose their desired properties. In Bi_2O_3 , while desirable oxygen vacancies act as charge carriers and enhance power density; under certain atomistic environments they themselves act as degradation agents. The environments that have not been understood from experiments until now are unraveled here. In nuclear materials, while the point defects are deleterious, they are not always damaging to materials. Only under specific atomistic environments do materials get damaged, understanding of such environments can help in tailoring better materials. During the course of this research, it was found that conventional radiation-damage MD simulation is not capable enough to reveal complete evolution of point defects. Hence, a new methodology is developed to perform such simulations. In addition to MD, density

functional theory (DFT) is also used to validate MD simulation results and to reveal certain electronic phenomena that are beyond MD. To characterize materials from structural viewpoint, crystallography is also used to illustrate the crystal structures.

1.8 Organization of Dissertation

The dissertation is organized on the basis of materials. It begins by giving some fundamentals of materials science relevant to this work in Chapter 2. Important aspects of MD simulation are provided in Chapter 3. Chapters 4, 5 and 6 are focused on Bi_2O_3 , where the point-defect evolution, oxygen diffusion and their effect on the structure of Bi_2O_3 are discussed in detail. Chapters 7 and 8 are focused on the fundamentals of radiation damage and point-defect evolution in MgO and UO_2 . Finally, the effect of microstructure on the evolution of point defects in BCC Mo is elucidated in Chapter 9. The conclusions of this work and envisioned future work are given in Chapter 10.

CHAPTER 2 DEFECTS IN SOLIDS

2.1 Introduction

On the atomic level, a crystalline material is a collection of atoms that are arranged in a periodic fashion providing three-dimensional long-range structural and chemical order. There are a large number of different crystal structures, varying from simple structures of pure metals to more complex ones found in ceramic materials. During processing of materials, it is very difficult to maintain an infinite three-dimensional long-range order. More often, this long-range order is disrupted by defects. These defects can be of different kinds classified by the spatial dimensions: point defects (zero-dimensional), dislocations and stacking faults (one-dimensional), grain boundaries and surfaces (two-dimensional), pores and cracks (three-dimensional). In this work, the effect of point defects on the materials behavior is studied.

2.2 Intrinsic Point Defects

Intrinsic Point defect involves one atom, which is either missing from a crystalline site or is additionally present in an open space in a crystal. An atom missing at its crystalline site is called a *vacancy*; an additionally present atom is known as an *interstitial*. Figure 2-1 (a) shows a two dimensional long range lattice of atoms. A missing atom in Figure 2-1 (b) shows a vacancy and an additional atom in the open space represents an interstitial (Figure 2-1 (c)). In this simple perfect lattice, all nearest neighbor atoms are equidistant from each other, whereas, the lattice is locally strained in the presence of the vacancy or interstitial. The vacancy creates an open space into which the neighboring atoms relax, as shown in Figure 2-1 (b). In contrast, the interstitial

constrains the neighboring atoms because the open space between the crystalline atoms is usually smaller than the size of the interstitial (Figure 2-1 (c)).

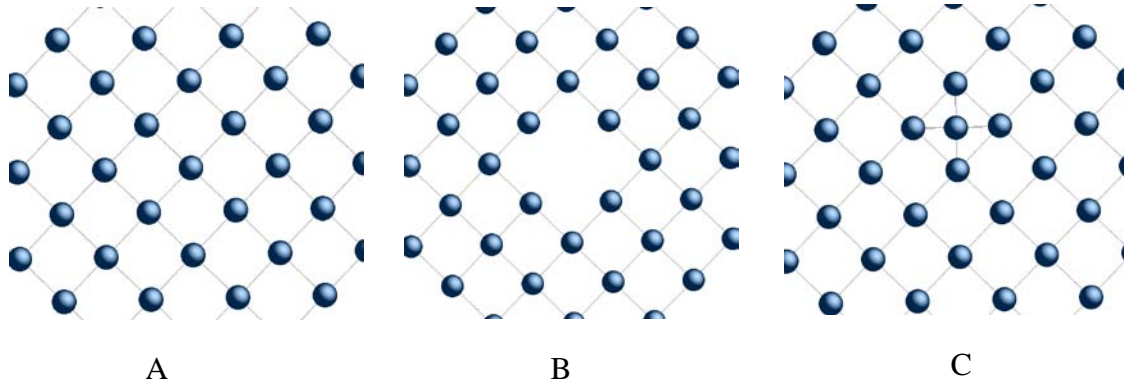


Figure 2-1. Point defects. A) 2-D lattice of atoms. B) a vacancy. C) an interstitial

2.2.1 Frenkel Defect

A Frenkel defect is a vacancy-interstitial pair formed when an atom jumps from its crystal lattice site to an interstitial site leaving behind a vacancy. A Frenkel defect is shown schematically in Figure 2-2 (a). It was first observed by a Russian scientist Yakov Frenkel in 1926, and hence the name.

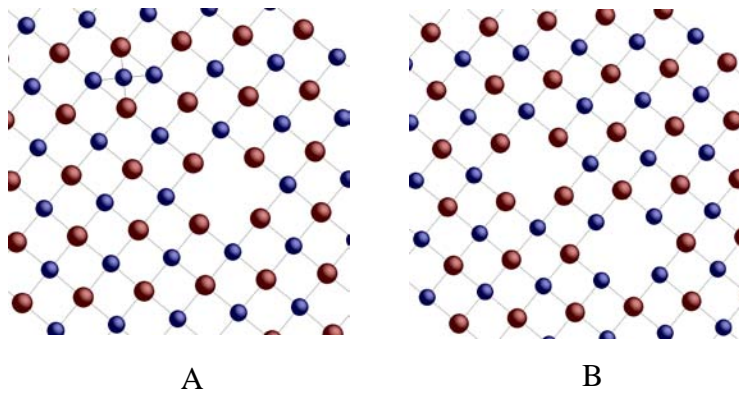


Figure 2-2. Point defects in ionic materials. A) Frenkel pair B) Schottky defect

Using Kröger-Vink notation, the Frenkel defect on the cation (Mg) lattice can be expressed as:



2.2.2 Schottky Defect

A Schottky defect occurs when a stoichiometric units of cation and an anion leave the crystal site and segregate at an external surface (grain boundary, surface, etc.) leaving behind a vacancy each on cation and anion site. A Schottky defect is shown in Figure 2-2 (b). This defect is unique to ionic materials and stoichiometric numbers of cations and anions have to be missing to maintain electroneutrality in the material. This defect was first discovered by German scientist Walter H. Schottky. The Schottky defect in MgO crystal can be expressed as:



There are other defects, both intrinsic and extrinsic, which are prevalent in the materials. However, we limit ourselves to the above two point defects that are most central to this thesis.

2.2.3 Thermodynamics of Point Defects: Equilibrium Concentration

Point defects are a part of the equilibrium state of a chemically pure ideal crystal. Any material under equilibrium has a specific concentration of point defects. It appears unintuitive because it would cost energy (enthalpy change, ΔH) to create a point defect, which will increase from the lattice energy of a defect-free crystal. However, the equilibrium state of the crystal is determined not by the lowest lattice energy but by the lowest total free energy. With the creation of a defect (say, a vacancy), there are entropy changes. The increase in the entropy of the crystal lowers the total free energy of the crystal, thereby, stabilizing the crystal by forming an equilibrium concentration of vacancies. For a given temperature, the equilibrium concentration of vacancies can be analytically calculated as shown below.¹⁶

Free energy of a perfect crystal

The free energy is given as:

$$G_{perf} = H_{perf} - TS_{perf} \quad (2-3)$$

where H is the enthalpy, S is the entropy and T is the absolute temperature of crystal.

The total entropy consists of contributions from two types of entropies, the configurational entropy and the vibrational entropy.

$$S = S_{config} + S_T \quad (2-4)$$

Configurational entropy is due to the different arrangements that the atoms can have. For a perfect crystal, $S_{config} = 0$ as there is only one way of arranging N atoms. In Equation 2-4, the vibrational entropy, S_T , is the contribution to the entropy due to the vibration of the atoms. In simple terms, it can be given by

$$S_T = Nk \left(\ln \frac{kT}{h\nu} + 1 \right) \quad (2-5)$$

where N is the number of atoms involved, k is the Boltzman's constant and ν is the vibrational frequency of the atoms in the perfect crystal. Therefore, putting back to Eq. 2-3,

$$G_{perf} = H_{perf} - NkT \left(\ln \frac{kT}{h\nu} + 1 \right) \quad (2-6)$$

Equation. 2-6 is used later to compare against the G_{def} to calculate the equilibrium concentration of vacancies for a given temperature. Now the attention is turned to the crystal with defects to formulate G_{def} .

Free energy of the crystal with defects

If it takes h_d joules to create one defect, and if the number of defects created are n_v then,

$$H_{def} = H_{perf} + h_d n_v \quad (2-7)$$

In the defected crystal, since there are n_v new crystal lattice sites, therefore, N atoms can now be distributed on $N + n_v$ sites. There is a change in the configurational entropy, which is represented as:

$$S_{config} = -k(N \ln \frac{N}{N + n_v} + n_v \ln \frac{n_v}{n_v + N}) \quad (2-8)$$

Due to the presence of the vacancies, the nearest neighbor atoms will essentially vibrate with a different frequency, ν' . If the coordination number of each vacancy is ζ , the total number of atoms affected by the creation of new vacancies is $n_v \zeta$. The vibrational entropy of term is given by:

$$S = k(N - \zeta n_v) \left(\ln \frac{kT}{h\nu} + 1 \right) + n_v \zeta k \left(\ln \frac{kT}{h\nu'} + 1 \right) \quad (2-9)$$

By combining Equations. 2-7 to 2-9, the free energy of a crystal containing defects is:

$$G_{def} = H_{perf} + n_v h_d - T(S_{config} + S) \quad (2-10)$$

The change in the free energy by creating the defects is given as:

$$\Delta G = G_{def} - G_{perf} \quad (2-11)$$

i.e.,

$$\Delta G = n_v h_d + kT n_v \zeta \ln \frac{\nu'}{\nu} + kT \left(N \ln \frac{N}{N + n_v} + n_v \ln \frac{n_v}{n_v + N} \right) \quad (2-12)$$

At a constant T , a ΔG versus n_v plot goes through a minimum which illustrates that the creation of defects lowers the free energy of the system thus making it energetically favorable. Beyond the equilibrium concentration of the defects, further increase in the defects is no longer energetically favorable and the free energy increases again. The equilibrium number of vacancies, n_{eq} , can be obtained at the minimum of the curve, i.e., when $\partial \Delta G / \partial n_v = 0$.¹⁶

$$\frac{n_{eq}}{N} \approx \exp\left(-\frac{h_d - T\Delta S_{vib}}{kT}\right) \quad (2-13)$$

Hence, the system is thermodynamically driven towards n_{eq} under equilibrium. This feature of point defects will be witnessed in Chapter 9 in which the creation of the vacancies from the grain boundaries driving the system towards equilibrium concentration of vacancies will be illustrated.

2.3 Transport

2.3.1 Atomistic Theory of Diffusion

Atoms constantly vibrate due the energy provided by the surroundings. At sufficiently high temperatures, the energy is high enough for a vigorous vibration, which can overcome the migration energies (and attempt frequencies) leading to diffusion of atoms. There are various materials' phenomenon that occur due to diffusion: carbonization, ionic conduction, creep to name a few.

Under a concentration gradient, the randomly diffusing atoms are directed in specific direction resulting in a flux. Fick's law gives the relationship between the flux of atoms under a concentration gradient. The flux of atoms, J , and the concentration gradient, dc/dx are related by:

$$J = -D \frac{\partial c}{\partial x} \quad (2-14)$$

where D is the self-diffusion coefficient.

The self-diffusion coefficient, D , of a diffusing ion or atom is given by:¹⁶

$$D = \Omega \lambda^2 \alpha \quad (2-15)$$

where Ω is the frequency of the successful jumps, λ is the elementary jump distance and α is a geometric constant. If the diffusion is by a vacancy mechanism, then, $\alpha = 1/\zeta$ (ζ is the coordination number of the vacancy).

The jump frequency, Ω , can be written in terms of the probability of having an energy to make a jump, ν , and θ , the probability that the adjacent site is vacant. That is

$$\Omega = \nu\theta \quad (2-16)$$

$$\nu = \nu_o \exp\left(-\frac{\Delta H_m}{kT}\right) \quad (2-17)$$

ν_o is the vibration of the atoms.

Since a vacancy can make a jump to any of the available sites surrounding it, $\theta \approx 1$.

Putting all the variables,

$$D_{vac} = \alpha\zeta\lambda^2\nu_o \exp\left(-\frac{\Delta H_m}{kT}\right) \quad (2-18)$$

In atomistic simulations, the self-diffusivity, D_A , of the atoms can be directly calculated from the mean square displacement (MSD) of the atoms.

$$D_A = \frac{1}{6t} \langle |r_i - r_o|^2 \rangle \quad (2-19)$$

The vacancy diffusivity D_v and the interstitial diffusivity D_i are given by:

$$D_v = \frac{D_A}{c_v f_v} \quad (2-20)$$

$$D_i = \frac{D_A}{c_i f_i} \quad (2-21)$$

where f_v and f_i are the correlation factors. Correlation factor depends upon the crystal structure and diffusion mechanism.

2.3.2 Diffusion Mechanisms

To understand the role of different atomistic species in diffusion, it is important to understand their diffusion mechanisms. Atoms, vacancies and interstitials have different diffusion mechanisms.¹⁷

2.3.2.1 The vacancy mechanism

An atom diffuses by a vacancy mechanism when it moves into a vacancy occupying a nearest neighbor lattice site. In this mechanism, the atom and the vacancy swap lattice sites; they move in the opposite direction to each other. Figure 2-3 shows the diffusion of an atom through the vacancy mechanism.

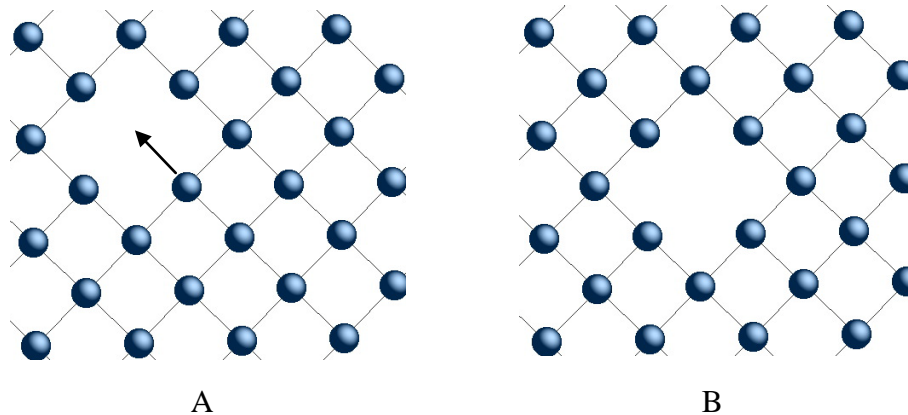


Figure 2-3. Diffusion by vacancy mechanism. An atom in (A) diffuses in the direction shown by arrow. (B) Atom and vacancy swap positions.

By this mechanism, the vacancy has a higher diffusivity than ion because the ion has to wait for a vacancy to come in its vicinity, whereas, a vacancy can exchange sites with any of the neighboring atoms.

2.3.2.2 The interstitial mechanism

In this mechanism, the defect (interstitial) occupies an interstitial site before and after the diffusion jump. Since the diffusing species and the defect are the same, they move in the same direction. Figure 2-4 shows the diffusion through the interstitial

mechanism. The interstitial can occupy the lattice site only if it comes across a vacancy (vacancy site).

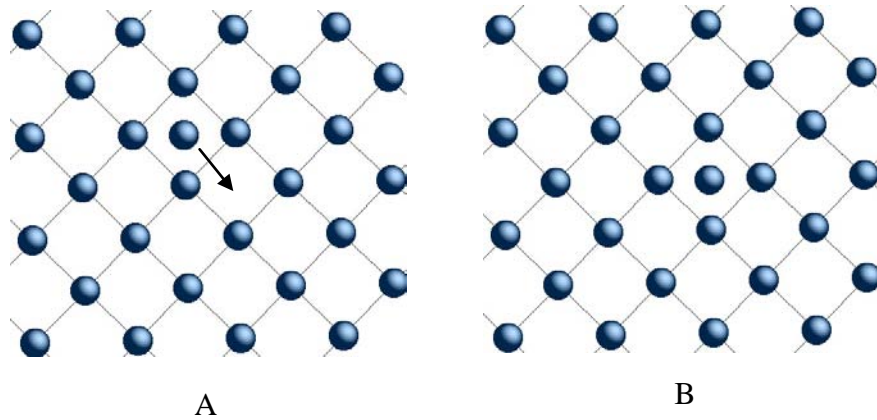


Figure 2-4. Diffusion by interstitial mechanism. An interstitial in (A) diffuses in the direction shown by arrow in (B).

2.3.2.3 The interstitialcy mechanism

This is a displacement diffusion mechanism in which an interstitial atom displaces a lattice atom from the site and occupies it. Each interstitial makes only one jump and has to wait for another interstitial to displace it from its lattice site.

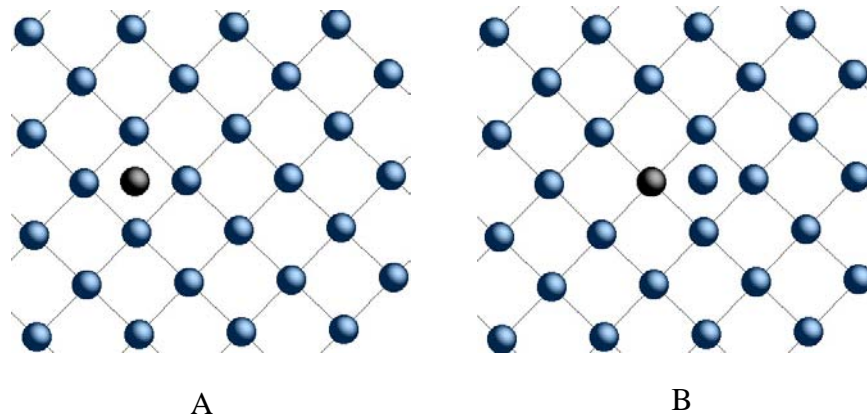


Figure 2-5. Diffusion by interstitialcy mechanism. An interstitial in (A) knocks a lattice atom and occupies the lattice site in (B).

Figure 2-5 shows the interstitialcy mechanism of diffusion.

2.4 Crystallography of Materials

In this section, the crystal structure of the materials under investigation is introduced. In this thesis, while the primary focus is on the evolution of point defects in the fluorite-based materials ($\delta\text{-Bi}_2\text{O}_3$ and UO_2), some key point-defect mechanisms are elucidated from other materials (MgO and Mo), which are used as general model materials. $\delta\text{-Bi}_2\text{O}_3$ and UO_2 have fluorite crystal structures, MgO has a rocksalt crystal structure, and Mo has body centered cubic (BCC) structure.

2.4.1 Fluorite Crystal Structure: $\delta\text{-Bi}_2\text{O}_3$ and UO_2

In the fluorite crystal structure, the cations form an FCC network with the anions occupying all the eight tetrahedral sites thereby forming a simple cubic lattice (Figure 2-6).

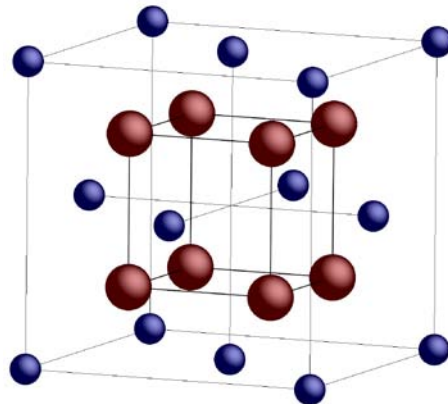


Figure 2-6. Fluorite crystal structure. The cations (shown in blue) form a FCC network and anions (in red) occupy the tetrahedral sites forming a simple cubic lattice. There are therefore four cations and eight anions in a fluorite unit cell. The coordination number of the cations is eight and that of anions is four. The space group of fluorite crystal structure is $Fm\bar{3}m$ (number 225). The cations occupy the Wyckoff site $4a$ and the anions occupy $8b$.

While UO_2 has fluorite crystal structure, $\delta\text{-Bi}_2\text{O}_3$ has a fluorite-related crystal structure. In $\delta\text{-Bi}_2\text{O}_3$, there are six anions instead of eight and remaining two anion sites are vacant. Due to the vacant sites, the crystal structure is distorted and has the lower symmetry space group, $Fm\bar{3}$. The structural implications will be discussed later in detail in Chapter 6. For now, $\delta\text{-Bi}_2\text{O}_3$ is analyzed within the $Fm\bar{3}m$ space group.

2.4.2 Rocksalt Crystal Structure: MgO

In the rocksalt crystal structure, both cations and anions form interpenetrating FCC networks (Figure 2-7). In a rocksalt unit cell, there are equal number of cations and anions, therefore, the structure has a stoichiometric ratio of 1:1. The space group of rocksalt crystal structure is same as that of the fluorite, i.e., $Fm\bar{3}m$.

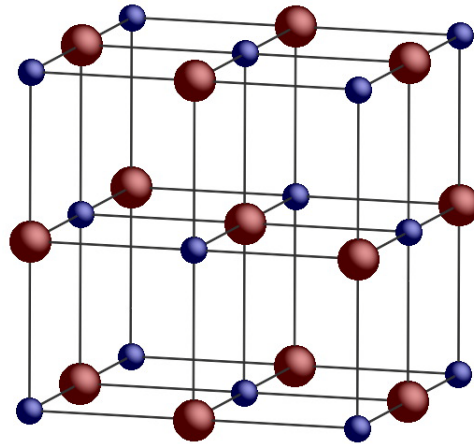


Figure 2-7. Rocksalt crystal structure.

Both cations and anions have a multiplicity of 4, therefore they occupy Wyckoff sites 4a and 4b respectively.

2.4.3 Space Group $Fm\bar{3}m$

All the three materials mentioned above have a space group of $Fm\bar{3}m$. The number of this space group is 225 and the point group symmetry is $m\bar{3}m$.¹⁸ $Fm\bar{3}m$ is more fully

written as $F \frac{4}{m} \bar{3} \frac{2}{m}$. The first letter, the centering type, represents the translational symmetry in three dimensions. Here, F represents a Face Centered Cubic symmetry operation. The three entries following the centering type are three kinds of symmetry directions of the lattice belonging to the space group. According to their position in the sequence, the symmetry directions are referred to as primary, secondary and tertiary directions. For the cubic lattice, the primary symmetry directions are $\langle 100 \rangle$, i.e., $[100]$, $[010]$ and $[001]$; the secondary symmetry directions are $\langle 111 \rangle$; and the tertiary symmetry directions are $\langle 110 \rangle$.

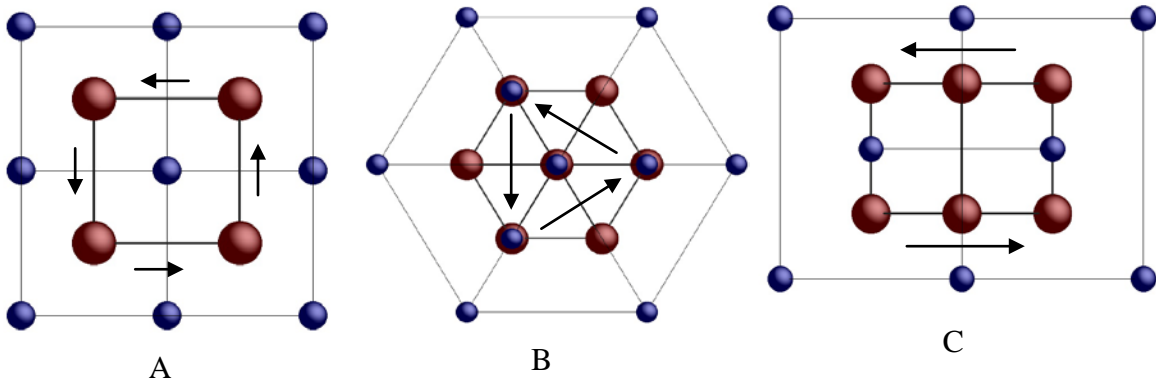


Figure 2-8. Schematics showing three different symmetry operations represented by the space group $F \frac{4}{m} \bar{3} \frac{2}{m}$. A) A four-fold rotation symmetry along $[100]$. B) A three-fold inversion symmetry along $[111]$. C) A two-fold rotation symmetry along $[110]$.

In the $F \frac{4}{m} \bar{3} \frac{2}{m}$ symmetry, $4/m$ represents four-fold rotational symmetry along the primary direction and two perpendicular mirror planes in perpendicular direction to rotation. $\bar{3}$, represents the roto-inversion along the body diagonal of the unit cell which is also the secondary direction. The symmetry operation $2/m$ represents the two-fold rotation along the edge of the unit cell (tertiary direction) along with two perpendicular

mirror planes in perpendicular direction to the rotation. The symmetry operations for four-fold rotation, three-fold roto-inversion and two-fold rotation are given schematically in Figures 2-8 (a), (b) and (c) respectively using a fluorite crystal structure.

2.4.4 Body-Centered Cubic: Space Group $Im\bar{3}m$

Mo has a BCC crystal structure with one atom occupying the center of a cubic unit cell. The schematic representation is given in Figure 2-9. The space group of BCC crystal structure is $Im\bar{3}m$. The space group number is 229, the Wyckoff position is $2a$, and the point group symmetry is also $m\bar{3}m$.¹⁸ In this space group, I represents body-centered translational symmetry. The rest of the symmetry directions are same as the fluorite crystal structure.

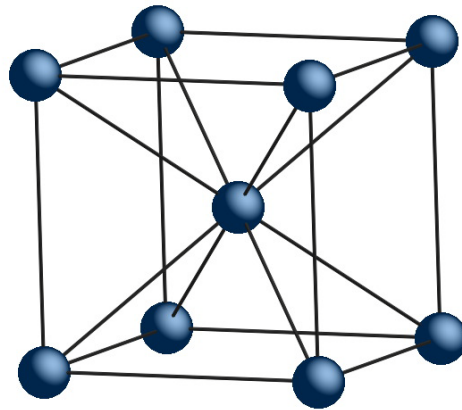


Figure 2-9. Body-centered crystal structure.

CHAPTER 3 SIMULATION METHODOLOGY

3.1 Simulation Methodologies

In principle, all properties of materials are describable by using quantum mechanics (QM).¹⁹ However, unraveling all materials properties from QM is unrealistic due to small system sizes ($10^2 - 10^3$ atoms) that QM can handle; materials engineering, in contrast, involve larger length scales upto of the order of 10^{22} atoms. To elucidate various materials' behaviors over wide length scale, different simulation methodologies are used to bridge this gap. At the engineering scale (10^{-3} m and above), macroscopic stresses, large temperature gradients, etc., that drive the materials behavior are captured by continuum simulation methods.²⁰ One step down the length scale is the mesoscale ($10^{-6} - 10^{-3}$ m); grain boundaries (GBs), voids, etc. that govern the properties of materials at this scale are modeled by kinetic Monte Carlo²¹ and phase-field methods.²² Further down the length scale lie atomistic scale, modeling of which is done by using molecular dynamics simulation ($10^{-10} - 10^{-6}$ m) using interatomic potentials^{23,24} and force fields.²⁵ Atomic diffusion, dislocations and other atomistic phenomenon are accurately captured by this method. At the lowest level lies the electronic scale ($10^{-12} - 10^{-10}$ m), modeling of which is done by QM methods to elucidate various electronic phenomenon such as atomic bonding and surface adhesion.²⁶ While electronically and atomistically-informed multiscale modeling is an area of intense study, individual methods are widely used to understand specific properties in more detail.

The work in this thesis focuses primarily on the atomistic scale, hence, molecular-dynamics (MD) simulation is used to understand materials' behavior. However, to develop a profound understanding and to validate the hypothesis derived at various

junctures from MD, the electronic-level simulation using density functional theory (DFT) is also used.

3.2 Molecular Dynamics Simulation

MD simulation involves modeling of atoms as point particles, the interactions among which are defined by an empirical potential (plus Coulombic interactions if particles are charged). The dynamics is obtained from the Newton's equations of motion. The system of atoms is set-up with basic initial conditions like temperature, pressure and number of particles. Each atom is assigned a mass, charge and position, and the evolution of the system is obtained by advancing time using an integration scheme. With progressing time, the evolution of the system is followed and various properties including radial distribution functions, dynamics structure factor, phase-diagrams, thermal-expansion coefficient, diffusion, plastic deformation can be calculated. The accuracy of the calculated properties, however, depends entirely upon the fidelity of the interatomic potential used to model the material. Before discussing the potential and its implications, general MD simulation algorithm is discussed.

3.3 General MD Algorithm

In MD simulation of a crystalline solid, all atoms are initially assigned with the positions that define the crystal structure of the material. The atoms are also assigned random velocities based on the temperature given by the expression:

$$\frac{1}{2}mv^2 = \frac{3}{2}k_B T \quad (3-1)$$

where, m and v are the mass and velocity of the atoms, k_B is the Boltzman's constant and T is the desired temperature. Before beginning the simulation, the angular momentum is set to zero.

The forces on the atoms are calculated from the interatomic potential (described later) as:

$$\vec{F}_i = -\frac{\partial U}{\partial \vec{r}_i} \quad (3-2)$$

where, U is the potential energy that an atom i experiences due to atom j , r_i is the distance between the two atoms, and \vec{F}_i is the force. The motion of the atom i , is expressed by the second law of motion where the force, \vec{F}_i is related to the acceleration as

$$\vec{F}_i = m_i \vec{a}_i \quad (3-3)$$

where, m_i and a_i is the mass and acceleration of atom i .

Equation 3-2 may also be written as

$$m_i \frac{\partial^2 \vec{r}_i}{\partial t^2} = \vec{F}_i \quad (3-4)$$

The velocity and position of atoms at a time t , can be calculated from the acceleration of atoms. To advance time by a small increment dt , an integrator is used to obtain the position, velocity and acceleration of the atoms. There are various types of integrating algorithms available including Verlet,²⁷ leap-frog,^{28,29} velocity-Verlet, Beeman's,³⁰ predictor-corrector³¹ and symplectic integrators;^{32,33} they differ by accuracy and computational load. In this thesis, a 5th-order Gear predictor-corrector method³⁴ is used as an integrating method built in our in-house MD code. This method uses a higher-order Taylor expansion of the atomic position about the current position, $x(t)$, up to the 5th derivative. The positions of the atoms at the next time increment are predicted by using the current position, velocity, acceleration, third, fourth and fifth order derivatives of $x(t)$ given as:

$$x^p(t+dt) = \vec{x}(t) + \vec{v}(t)dt + \frac{1}{2!} \vec{a}(t)dt^2 + \frac{1}{3!} \frac{d^3\vec{x}}{dt^3}(t)dt^3 + \frac{1}{4!} \frac{d^4\vec{x}}{dt^4}(t)dt^4 + \frac{1}{5!} \frac{d^5\vec{x}}{dt^5}(t)dt^5 \quad (3-5)$$

Similarly, velocity, acceleration and higher order derivatives are also predicted. This prediction is not very accurate as it is mere a Taylor expansion. The second step in the predictor-corrector method is the force evaluation step. Here, the forces on the atoms are evaluated using the predicted positions. Using this force, the correct accelerations $a^c(t+dt)$ may then be calculated. The error between the predicted acceleration $a^p(t+dt)$ and the correct acceleration $a^c(t+dt)$ can be given by:

$$\Delta\vec{a}(t+dt) = \vec{a}^c(t+dt) - \vec{a}^p(t+dt) \quad (3-6)$$

The position, velocity and higher order derivatives are then corrected based on the corrected acceleration. The corrected position, velocity and acceleration is be given by:

$$\vec{x}^c(t+dt) = \vec{x}^p(t+dt) + c_0\Delta\vec{a}(t+dt) \quad (3-7)$$

$$\vec{v}^c(t+dt) = \vec{v}^p(t+dt) + c_1\Delta\vec{a}(t+dt) \quad (3-8)$$

$$\vec{a}^c(t+dt) = \vec{a}^p(t+dt) + c_2\Delta\vec{a}(t+dt) \quad (3-9)$$

where, c_0 , c_1 , c_2 are empirically-determined numerical constants 3/20, 251/360 and 1 respectively. The higher order derivatives are corrected similarly.

The predictor step provides an initial guess to which the successive corrective step should converge to correct trajectories. Iterative corrective steps can be employed to obtain a highly accurate answer; in MD however, only one or two corrective iterations are performed to save the computation time. This process is repeatedly followed for a desired amount of time or until the system reaches equilibrium or the dynamical behavior of interest has taken place.

The time step used for advancing the simulation time is one of the most crucial entities. To capture the atomic motion correctly, time step, dt , is typically taken to be 1 fs.

It is however necessary to calculate the correct time step from test simulations by checking the conservation of the energy.

3.4 Periodic Boundary Condition

There are two major types of boundary conditions:³⁵ isolated boundary condition (IBC) and periodic boundary condition (PBC). In IBC, the atoms are surrounded by vacuum and are assumed to be far away from any kind of external forces. IBC is generally suited for studying clusters of atoms. In contrast, PBC is more prevalent boundary condition for studying bulk materials. In PBC, the cubic super-cell is replicated in three dimensions thus filling the space to form an infinite lattice (Figure 3-1).

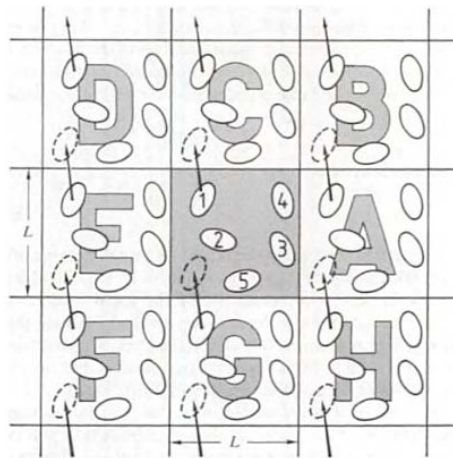


Figure 3-1. Two-dimensional periodic system of a simulation cell. The shaded box is the actual simulation box; surrounding boxes are its periodic images. Also shown is the displacement of atom (marked as 1) by an arrow going out of the box. Due to PBC, its images also displace in same fashion and another atom enters the simulation box from bottom. (Reproduced from reference 34)

By applying PBC, the problem of surfaces is overcome. In a PBC simulation, if an atom moves in the super-cell, its image also moves exactly in the same way in the neighboring super-cells. Further, if an atom leaves the super-cell, its image enters from the other side of the super-cell. PBC also allows traveling waves in the system thus allowing the system to behave like a large medium. In this manner, PBCs allow to

model a three-dimensional bulk system. However, if applied incorrectly, an atom can interact with its own image and cause artifact in the results. It is particularly true in the case of defects. To prevent such interaction, a large enough system of atoms is therefore necessary to model materials such that the images are fairly separated and do not interact with each other. (*For a detailed discussion on PBC, reader is directed to reference 34*).

3.5 Interatomic Interactions

The origin of interatomic-forces theory can be traced back to the work of Maxwell, Clausius and others (before 1900). It was around that time that an understanding of the atom was being fully accepted, though it was still thought as indivisible. Certainly before that time, the understanding on the origin of the interatomic forces was not prevalent. Clausius introduced the virial theorem in which he showed that the virial coefficients depend (B , C , etc.) on the forces that atoms exert on each other.³⁶

$$pV = RT\left(1 + \frac{B}{V} + \frac{C}{V^2} + \dots\right) \quad (3-10)$$

B is due to collision between pair of atoms, C is due to tertiary collision, etc. The nature of forces was however not known. Van der Waals first showed that the interaction energy between the atoms in a gas consisting of attractive and repulsive potential can be approximated by:

$$\left(p + \frac{a}{V^2}\right)(V - b) = nkT \quad (3-11)$$

He suggested that atoms could not come close beyond certain distance without overcoming the repulsive forces. It became clearer that at smaller distances, repulsive forces were the dominant forces and an inverse power law could be used to represent the interatomic potential.

$$U(r) = \frac{C_1}{r^n} - \frac{C_2}{r^m} \quad (3-12)$$

where, C_1 and C_2 are constants, n and m are integers ($n > m$) and r is the distance between two atoms. The first term is the repulsive term and second term is the attractive term.

(The Lennard-Jones R-6 potential is based on the same form). More broadly though, the origin of the attractive and repulsive forces was still not clear. The fundamental understanding was later developed by the theories from Pauli (1925), London (1930) and others when the quantum nature of particles was recognized. They will be discussed later in some detail.

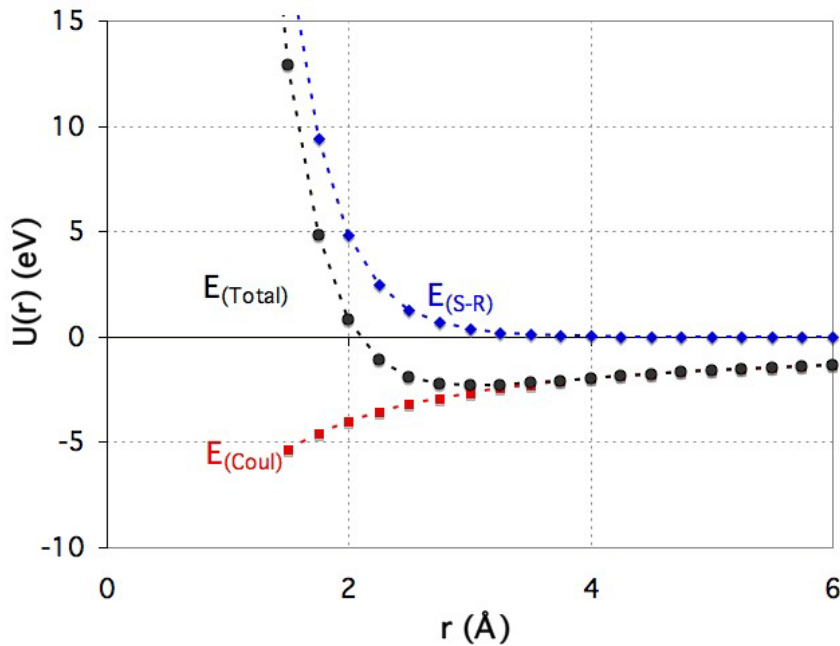


Figure 3-2. Inter-ionic potential between Zr^{4+} and O^{2-} as a function of distance between the two ions. The total potential (E_{Total}) is a sum of short-range (E_{S-R}) and Coulombic (E_{Coul}) potential. The short-range potential is mainly repulsive and the Coulombic is attractive. The parameters for the potential are taken from Khan *et al.*³⁷

The above discussion is based only on the short-range interatomic forces, which were then being understood in small molecules, primarily gases like H_2 , N_2 and noble gases.

During the same period, theory behind ionicity of materials was also being developed

with the first works done by Madelung and Born.¹⁶ It was realized that in the ionic crystals, that atoms were charged and therefore also interacted through Coulombic forces. These interactions are long-range and go beyond nearest neighbors. Hence, ionic materials not only have the short-range interactions but also long-range Coulombic interactions. To illustrate both types of potentials and their effective sum, the inter-ionic potential energy as a function of distance between Zr^{4+} and O^{2-} ions is shown in Figure 3-2. Since this thesis primarily deals with ionic materials, the origin of both kinds of potentials will be delved into. The long-range, difficult to calculate, Coulombic interactions are discussed first.

3.5.1 Long-range Interactions

The long-range forces arise from the Coulombic interaction of the charged ions, here shown are Zr^{4+} and O^{2-} . In ionic system, ions are periodically arranged with all cations being at a specific distance from anions. To arrange the atoms in the periodic fashion, the work done to bring ions from infinity to a distance r apart is given by the Coulombic law:

$$E_{Coul} = \frac{q_1 q_2}{r} \quad (3-13)$$

where, and q_1 and q_2 are the charges of the ions (here, +4 and -2) and E_{Coul} is the Coulombic energy in eV and r is the inter-ionic spacing in Å. If two ions are oppositely charged, there is an attractive force between them and the Coulombic energy is negative. If the ions are of the same charge, then they repel each other and the Coulombic energy is positive. The Coulombic interactions are not limited to the closest neighbors but span large distances, as illustrated by the long E_{Coul} tail in Figure 3-2. To accurately calculate E_{coul} experienced by every ion, one has to essentially extend to very long (virtually

infinite) distances, which under is not computationally feasible. As a result, one has to truncate the Coulombic interactions at a certain distance, R_c , which can lead to non-convergence (discussed later). To overcome non-convergence, there are methods to accurately calculate E_{Coul} term. Two prevalent methods are the Ewald method³⁴ and direct summation method.³⁸ Ewald summation method is more precise but is also more computationally cumbersome than the direct-summation method. The computational load, in the Ewald summation method, increases as an order of N^2 in comparison to N in the direct-summation method. Since throughout this thesis, the focus is on understanding the equilibration of point defects, which occurs on longer MD time scale, a relatively less expensive, direct-summation method is chosen. The method has been shown to work well not only for crystalline but also disordered systems.³⁸

Direct-summation method

The foremost problem that causes non-convergence is that with choice of any truncation radius (R_c), the system summed over is practically never charge neutral.

To overcome this problem, in the direct-summation method,³⁸ charge neutrality is achieved by viewing an ionic crystal system as a charge-neutral molecule consisting of Bravais lattice sites such that the molecules are never broken so as to preserve charge neutrality. For example, instead of considering NaCl as two interpenetrating FCC networks of Na and Cl, it is thought of as $(\text{NaCl})_4$ molecule. When it is truncated at radius R_c , the molecule as a whole is retained. To achieve this, in the direct-summation method, the net charge on the truncation sphere is neutralized by adding extra charge on the surface of the truncation sphere of every ion, thus enabling good energy convergence. Lets discuss by taking examples, both, for the problem and its remedy from reference 38.

Without applying any convergence criteria, Figure 3-3 shows a comparison between the energy per ion as a function of cut-off radius, R_c , and a fully-converged value ($R_c \rightarrow \infty$). The energy for cut-off R_c is shown as open circles and the fully converged result is shown as a horizontal broken line. It is clear that the energy deviates considerably from the correct value when the system is left charged after truncation.

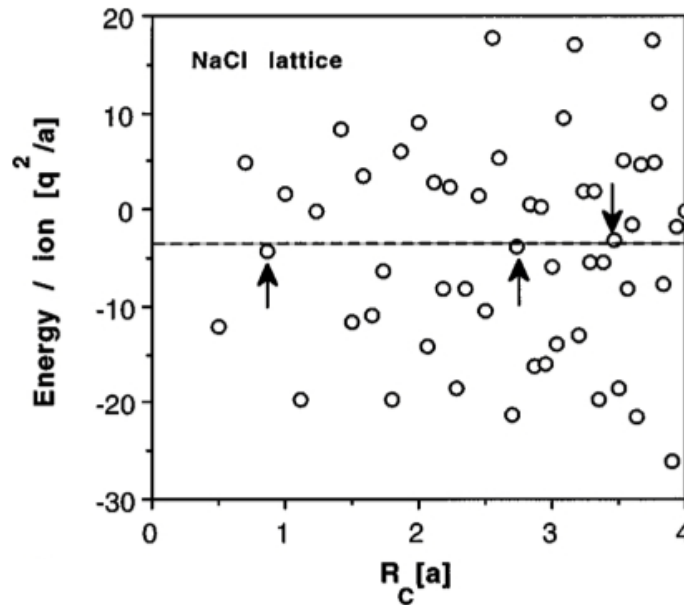


Figure 3-3. Total Coulombic energy per ion obtained by summing the Coulomb pair potential over a cut-off radius R_c (shown in open circles). The straight line indicates the fully converged value ($R_c \rightarrow \infty$). The arrows mark those truncations that have exactly or nearly neutral systems. (Reproduced from reference 38)

Some of the data points that lie on the line (shown by arrows) are those that are summed over neutral or nearly neutral units. The solution proposed in the direct-summation method is to place neutralizing charges on the surface of the truncation sphere, such that all those ions that are incomplete molecules can form charge-neutral molecules. This is shown in Figure 3-4. The correct energy (E^{Mad} : Madelung energy) can then be calculated by subtracting the neutralizing energy from the calculated energy before neutralizing.

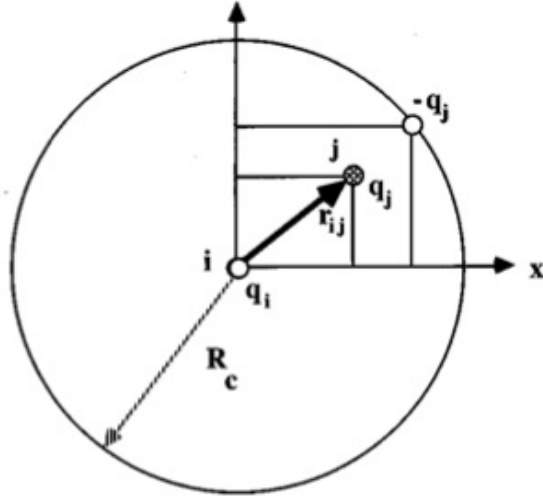


Figure 3-4. For every charge q_i , an opposite charge q_j is placed on the surface of the truncation sphere of radius R_c . (Reproduced from reference 38)

It can be represented as:

$$E_{tot}^{Mad}(R_c) = E^{tot}(R_c) - E_{tot}^{neutr}(R_c) \quad (3-14)$$

$$\approx \frac{1}{2} \sum_{i=1}^N \sum_{\substack{j \neq i \\ (r_{ij} < R_c)}} \frac{q_i q_j}{r_{ij}} - \frac{1}{2} \sum_{i=1}^N \sum_{\substack{j=1 \\ (r_{ij} < R_c)}} \frac{q_i q_j}{R_c} \quad (3-15)$$

With the neutralizing charges, there is a dramatic effect on the Madelung energy of the spherically truncated sphere. A comparison between the charged-neutralized and charged truncated sphere is shown in Figure 3-5. The plot shows a significant decrease in the energy fluctuation. However, even with the charge-neutralization scheme, the approximated Madelung (from equation 3-15) is still not comparable with the exact Madelung energy. A comparison between the two is shown in Figure 3-6, in which the solid circles are same as in Figure 3-5 but on much finer scale. The approximate Madelung energy oscillates about the exact Madelung energy in a slightly damped manner.

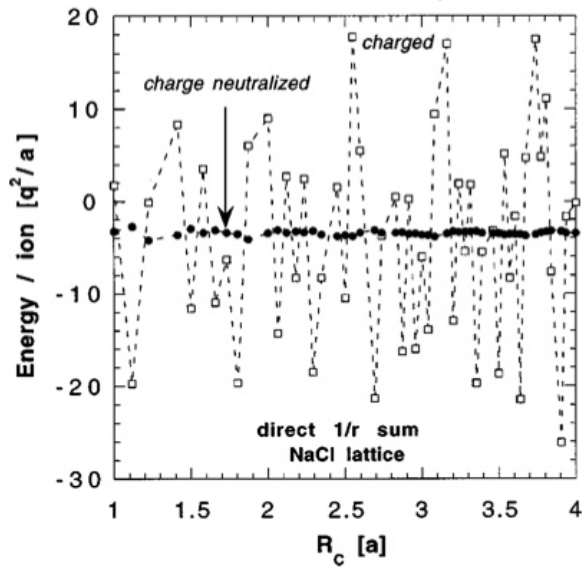


Figure 3-5. A comparison between the energies of the charge-neutralized and charged systems. The solid spheres represent charge-neutralized system and the open spheres represent charge system. (Reproduced from reference 38)

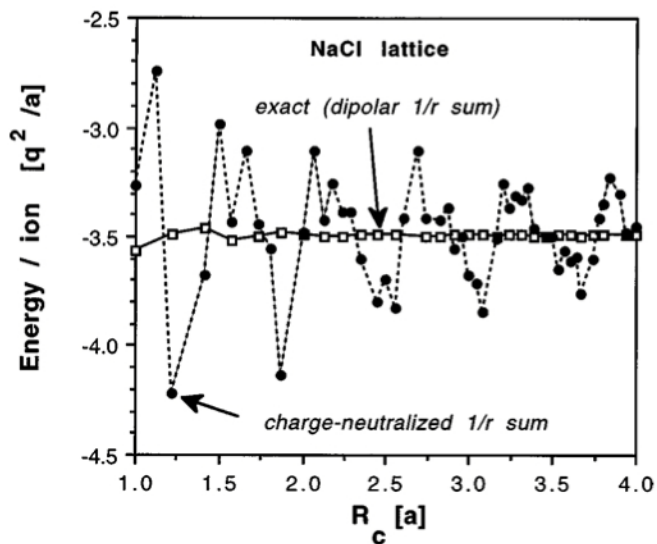


Figure 3-6. A comparison of the exact Madelung energy with the approximate Madelung energy. The approximate Madelung energy oscillates about the exact Madelung energy in a slightly damped manner. (Reproduced from reference 38)

In order to decrease the fluctuation, a damping function is introduced via the complementary error function. In simple terms, the damped, charge-neutralized coulomb pair potential can be expressed as:

$$E_{tot}^{Mad}(R_c) \approx \frac{1}{2} \sum_{i=1}^N \sum_{\substack{j \neq i \\ (r_{ij} < R_c)}} \left(\frac{q_i q_j \text{erfc}(\alpha r_{ij})}{r_{ij}} - \lim_{r_{ij} \rightarrow R_c} \left\{ \frac{q_i q_j \text{erfc}(\alpha r_{ij})}{r_{ij}} \right\} \right) - \left(\frac{\text{erfc}(\alpha R_c)}{2R_c} + \frac{\alpha}{\pi^{1/2}} \right) \sum_{i=1}^N q_i^2 \quad (3-16)$$

where α is the damping parameter. The damped charge-neutralized Madelung energy can now be compared with the undamped charge-neutralized (Figure 3-6). Such comparison is shown in Figure 3-7. The damped charge-neutralized energy oscillates much as in comparison to the undamped charge-neutralized energy. Further, the energy converges well to the exact Madelung energy within a distance of two lattice parameters.

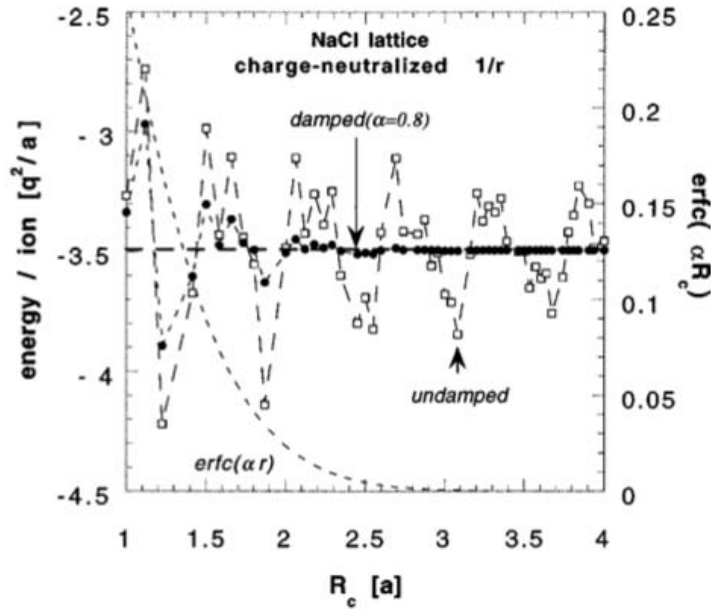


Figure 3-7. A comparison of the damped charge-neutralized Madelung energy with the undamped charge-neutralized energy. The plot also shows the exact Madelung energy represented by broken horizontal line. (Reproduced from reference 38)

The direct-summation method is built into our in-house MD code and has been used throughout the thesis.

3.5.2 Short-Range Interactions

Previously, it is discussed that the short-range interactions are mainly repulsive. However, there are also small attractive forces that act between the atoms. (*The short-range potential between Zr^{4+} and O^{2-} is shown in Figure 3-2, represented by diamonds in blue*). In this section, the origin of both the short-range interaction types, including the classic works of Pauli, Debye, Lennard-Jones,^{39,40} Buckingham,⁴¹ Born and London⁴² will be discussed.

From equation 3-13, the long-range attractive potential between the oppositely charged ions should bring the two atoms closer to each other such that as the distance between them goes to zero, the atoms should collapse and fuse! However, this does not happen. It follows that there must be some repulsive potential that keeps the two atoms certain distance apart.

To understand the repulsive forces, one has to go back to Pauli's exclusion principle,²⁶ which states that no two electrons can have the same quantum numbers. From the orbital viewpoint, there can be only two electrons in one orbital and they have to be of opposite spin. It follows that when two atoms are brought closer to each other, the electron clouds (orbitals) of both atoms penetrate into each other, which creates high density of electrons in a small region, thus, increasing the energy. The charged electron clouds repel each other giving rise to repulsive potential. This is the repulsive potential that is expressed as first term in the Lennard-Jones expression, C/r^n . The repulsive energy increases rapidly as the two atoms are brought close to each other. Hence, the interpenetration of the electronic clouds is the reasoning behind the short-range repulsive forces.

By using quantum methods to analyze noble gases, Bleick and Mayer³⁶ later gave a more refined form that shows that the repulsive energy follows as exponential form rather than power law. With this in mind, equation 3-11 can now be given as:

$$U(r) = C_1 e^{-\alpha r} - C_2 r^{-6} \quad (3-17)$$

where, C_1 , C_2 and α are the adjustable parameters. This is the form given in the Buckingham potential widely used in the ionic systems.

While the understanding on the repulsive forces was primarily achieved after the advent of the quantum mechanics, some understanding on the attractive part of the Van der Waals forces was established before the development of quantum theory. In 1912 and later, Keesom suggested that the dipole moment, μ , was the most important constant of the forces between two molecules.⁴² The *orientation* of the two dipoles was regarded as the interaction force between the two molecules, and was given as the interpretation for the attractive part in the Van der Waals forces. Later, Debye and Falckenhagen (1920-1922) suggested that apart from orientation effect, there is also an *induction effect*; that the charge distribution around a molecule changes in the presence of an electric field (due to polarizability α).⁴² At this point, London (1930) questioned both concepts and argued from quantum mechanics that rare gases were spherically symmetrical and none showed these interactions. He showed that interaction between the rare molecules could only be explained by the *dispersion effect*.⁴² (For detailed discussion, please refer reference 42). The sole reasoning was based on the uncertainty principle that a particle cannot be at absolute rest. He considered two spherically symmetrical isotropic harmonic oscillators with no permanent moment, and each with polarizability α . Using elastic and dipole

interactions energies, and the harmonic oscillator with frequency ν , he showed that the attractive energy between two rare gas molecules is given by:

$$U = -\frac{3}{4} \frac{h\nu_o\alpha^2}{r^6} \quad (3-18)$$

According to London, this is the force that illustrates the Van der Waals attractive force between the two uncharged rare atoms, the existence of which is without any permanent dipole or higher multiple preconditioning. The attractive force here is proportional to r^{-6} , which is the second (attractive) term in the Lennard-Jones expression, or for that matter, in the Buckingham potential form.

Hence, by combining all forces acting on an atom due to the surrounding atoms, the energy expression can be given as:

$$U(r) = \frac{q_1q_2}{r} + A \exp\left(-\frac{r}{\rho}\right) - \frac{C}{r^6} \quad (3-19)$$

where, the first term is the long range Coulombic term, second term is the short-range repulsive term and third term is the Van der Waals attractive term. A , ρ and C are adjustable parameters. In this thesis, this potential form has been used to model all ionic materials.

3.5.3 Electronic Polarizability – Shell Model

The electronic polarizability, α , is a measure of the effectiveness of an electric field E , in polarizing a material. It can be expressed as

$$\alpha = \frac{p}{E} \quad (3-20)$$

where, p is the dipole moment. To account for the electronic polarizability of the atoms in MD simulation, the shell model devised by Dick and Overhauser⁴³ is often used. In the shell model, an atom is described as consisting of a core and a shell. It is analogous to a

real atom, which has a nucleus surrounded by a cloud of electrons. In the shell model, core and shell represent nucleus and inner core electrons, and valence electrons of the atom respectively. The core and shell carry charge $X \bullet e$ and $Y \bullet e$ respectively; the total charge of the atoms is given by $(X+Y) \bullet e$. The shell is attached to the core by a spring of force constant k , such that the polarizability of the atom can be given by

$$\alpha = \frac{1}{4\pi\epsilon_0} \left(\frac{Y^2}{k} \right) \quad (3-21)$$

or,

$$\alpha = 14.3994 \left(\frac{Y^2}{k} \right) \quad (3-22)$$

where, ϵ_0 is the permittivity of the free space. The units of polarizability are \AA^3 .

3.5.4 Thermodynamic Conditions (ensemble) for Materials Simulation

In an MD simulation, certain pre-conditions are set to model materials, which replicate the environmental conditions for a real material. That is, the number of atoms, their position and chemical identity, temperature, pressure, volume are pre-defined in simulation to obtain certain physical properties. A system under a fixed number of atoms (N), constant volume (V) and temperature (T), is a simulation under canonical ensemble (NVT). Similarly, fixed number of atoms, constant pressure (P) and constant temperature constitute an isothermal-isobaric ensemble. There are other system conditions, such as micro-canonical ensemble (NVE), grand-canonical ensemble (μ VT) and isobaric-isoenthalpic ensemble (NPH) under which systems can be simulated.³⁴ Here, μ and H represent chemical potential and enthalpy respectively. In this work, all the simulations have been performed using the isothermal-isobaric ensemble (NPT), the methodologies for which are discussed in brief.

There are various algorithms that can be applied to maintain constant pressure.^{44,45} In the extended Lagrangian method given by Andersen,⁴⁴ one can imagine a set of pistons of certain mass is attached to the system of atoms. The force on the pistons is varied which changes the volume of the simulation box and maintains a constant pressure. The time scale for the box-volume fluctuations is roughly the same as the time for the sound waves to cross the simulation box.⁴⁴ This method applied pressure hydrostatically to the simulation cell. Parrinello and Rahman^{46,47} later extended this method to allow changes in shape and size of the box. In this thesis, the P-R method is used to simulate the system under NPT conditions.

To control the temperature of the atoms in the simulation box, a thermostat is used. The working of the thermostat is based on equation (3-1). To achieve a desired temperature, the velocities of the atoms are rescaled such that the total kinetic energy matches the desired temperature. One of the simplest of the many thermostats^{48,49,50} is the velocity-rescaling thermostat. In this method, to achieve a desired temperature T_d , the rescaled velocity v_s of the atoms is given by:

$$v_s = \sqrt{\frac{T_d}{T}} v_i \quad (3-23)$$

where, v_i is the initial velocity of the atoms and T_i is the initial temperature. Other widely used methods to control temperature of the system are Nosé-Hoover,^{48,51} Berendsen⁵² and generalized Langevin.⁵⁰

CHAPTER 4 IONIC CONDUCTIVITY OF SOLID-OXIDE FUEL CELL ELECTROLYTE

4.1 Fuel Cell

A fuel cell is a device that converts electrochemical energy into electricity. Generally, the sources of electrochemical energy are oxygen/air and hydrogen, or oxygen/air and hydrocarbons. The reaction between the hydrogen and oxygen ions releases electrons, flow of which generates electricity. The main byproducts of the reaction are water and heat. Compared to conventional (non-renewable) sources of energy, byproducts of the fuel cell are relatively more environmental friendly. Also to some extent, fuel cells can decrease our dependability on the non-renewable sources of energy, particularly, coal and oil.

There are various kinds of fuel cells, such as phosphoric acid fuel cell (PAFC), polymer electrolyte membrane fuel cell (PEMFC), molten carbonate fuel cell (MCFC), and solid oxide fuel cell (SOFC). The fuel cells are characterized by the electrolyte used in them. For example, in PAFCs, the electrolyte used is phosphoric acid, in PEMFCs, the electrolyte used is a polymer. Similarly, in MCFCs, the electrolyte used is molten carbonate and in SOFCs, a solid ceramic electrolyte is used. Fuel cells can also be distinguished by the ion that carries the charge. PAFCs and PEMFCs rely on hydrogen ion whereas MCFCs and SOFCs use oxygen transport. In the working of a fuel cell, the transporting ion diffuses through the electrolyte that is sandwiched between a cathode and an anode. If hydrogen is the charge carrier ion, it reacts with oxygen on the cathode. Otherwise, if the transporting ion is oxygen, it reacts with hydrogen on the anode. In both cases, the reaction between hydrogen and oxygen produces electrons, which travel through the outer circuit producing electricity. The general characteristics of these fuel

cells are listed in Table 4-1. Since these fuel cells have widely ranging power productions, they have different applications. Broadly speaking, PEMFCs are used for transportation energy generation and small communication devices; MCFCs can be used in marine equipments while PAFCs and SOFCs have anticipated applications in distributed-electricity generation. This thesis is focused on SOFCs.

Table 4-1. Characteristics of different fuel cells.

Fuel Cell	Electrolyte	Charge Carrier	Operating Temperature (°C)	Fuel
PAFC	Phosphoric Acid	H^+	100 - 200	H_2
PEMFC	Polymer	H^+	90	H_2
MCFC	Molten Carbonate	CO_3^{2-}	650	CH_4
SOFC	Ceramic	O^{2-}	600 - 800	CH_4

4.2 Solid Oxide Fuel Cell

A SOFC is shown schematically in Figure 4-1. At the cathode, oxygen molecules (O_2) ionize to form oxygen ions ($2O^{2-}$). The oxygen ion transports through the solid electrolyte to the anode where it reacts with hydrogen to produce water and electrons as shown in the schematic. The electrons travel through the outer circuit thus producing electricity.

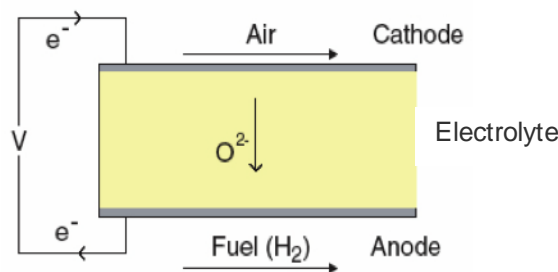


Figure 4-1. Working of a SOFC. (Reproduced from reference 53)

Fast transport of the oxygen ion through the high conducting electrolyte is important for achieving high power density in the SOFC. Efficient conductors are

therefore required to achieve high oxygen conductivity. Doped zirconia is one such high-oxygen conducting electrolytes and is widely used in current SOFCs. A comparison of the conductivity-temperature plot of yttria-stabilized zirconia (YSZ) with other electrolytes is shown in Figure 4-2. In addition to high conductivity, it also has good chemical stability in both the oxidizing and reducing environments that commonly occur in SOFCs.^{54,55} Hence, for working temperatures around 1000 °C, YSZ is a very good SOFC electrolyte.

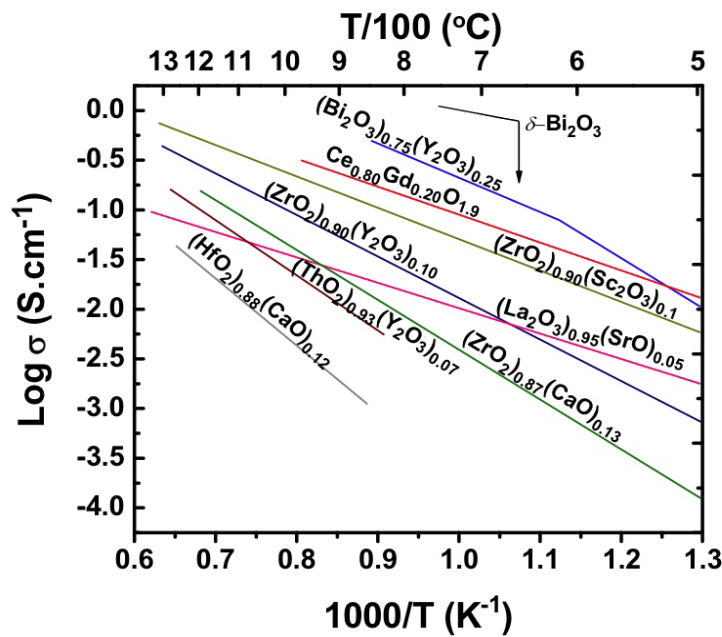


Figure 4-2. Conductivity versus temperature relationship of various electrolytes used in SOFCs. (Adapted from Reference 56, courtesy S. Omar⁵⁷)

However, such high temperatures cause problems including degradation of electrode due to demixing.⁵⁸ More importantly, it requires an all-ceramic construction, as metals cannot withstand such high temperatures. This in turn raises cost of the fuel cell.

To avoid these problems, intermediate temperatures, i.e., 500-700 °C, are therefore the desirable working temperatures of SOFCs. While intermediate temperatures prevent materials degradation, on the downside, the conductivity of the electrolyte also

decreases. Therefore, one of the foremost challenges in SOFC design is to develop materials that can maintain high conductivity at intermediate temperatures. Doped ceria (gadolinium-doped ceria (GDC) shown in Figure 4-2) is one such material. However, it has associated problem of low transference number. Transference number, $t_i = \sigma_i / (\sigma_i + \sigma_e)$, σ_i and σ_e are ionic and electronic conductivities respectively, i.e., it shows appreciable electronic conductivity, thus decreasing the open-circuit potential (OCP) of the cell.

δ -Bi₂O₃ is a material that does not suffer from either of these problems. It has higher conductivity than both YSZ and stabilized ceria (plot for δ -Bi₂O₃ in Figure 4-2) and also has a high transference number.⁵⁹ Because of these properties, it is a candidate material for electrolyte in SOFCs. However, it has other associated problems that are discussed later.

4.3 Fluorite-Based Cubic Bismuth Oxide

4.3.1 A Model Material

Cubic bismuth oxide (δ -Bi₂O₃) serves as a model material to understand oxygen diffusion and other atomistic phenomenon in the fluorite-based materials.

Fluorite-structure materials, e.g., ZrO₂ and CeO₂ cannot be directly used as electrolytes in SOFCs. In the operating oxygen partial pressure conditions, since the oxygen conduction takes place by vacancy mechanism, to facilitate conduction, oxygen vacancies are required. In a non-primitive fluorite unit cell, for example ZrO₂, there are four Zr⁴⁺ cations and eight O²⁻ anions (Figure 4-3 (a)). As such there are no inherently present oxygen vacancies. Oxygen vacancies are therefore extrinsically created. A standard procedure to create stoichiometric vacancies is by doping with trivalent oxides

(e.g. lanthanides: Y_2O_3 , Er_2O_3 , Gd_2O_3). An electrochemical reaction for doping of ZrO_2 by Y_2O_3 using Kröger-Vink notation can be given as:



When a trivalent dopant oxide (Y_2O_3) is introduced into tetravalent oxide (ZrO_2), the fewer number of oxygen atoms present in dopant oxide are balanced by oxygen vacancies to maintain stoichiometry. The positively-charged oxygen vacancies mediate in oxygen conduction. However, incorporation of the dopant creates charge and size imbalance on the cation sites. The doped cation sites (negatively charged) and vacant anion sites (positively charged) tend to associate with each other through electrostatic

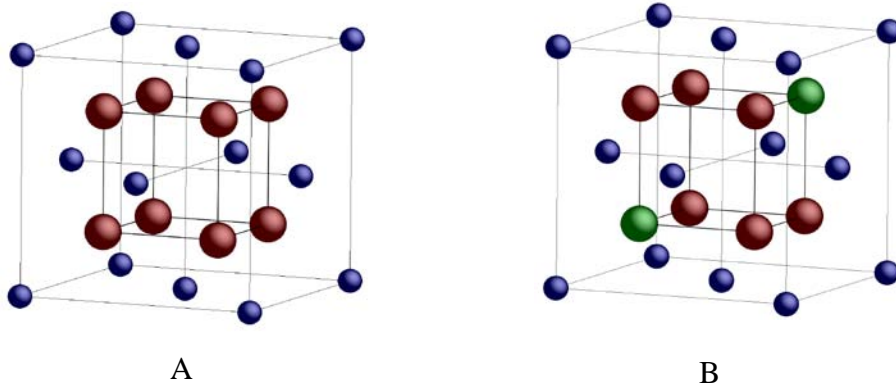


Figure 4-3. Fluorite crystal structure. A) ZrO_2 . B) $\delta-Bi_2O_3$. Ideal fluorite crystal structure in (a) has all eight oxygen sites filled, in contrast to (b) which has two vacant oxygen sites (vacancies). Color scheme – in blue are cations, in brown are anions and in green are oxygen vacancies.

Coulombic interactions. Consequently, it leads to formation of associated defect structures such as $Y'_{Zr} - V^{**}_O - Y'_{Zr}$.⁶⁰ In contrast, it has been shown recently that oxygen vacancies tend to associate with Zr^{4+} ions instead of Y^{3+} ions and is due to larger size of Y^{3+} ion.⁶¹ Regardless of the underlying mechanism, oxygen vacancy association limits oxygen diffusion and hence, decreases conductivity. Hence, although dopants provide vacancies for oxygen conduction, the oxygen conductivity gets limited due to associated

phenomena. Furthermore, dopant cation has different polarizability (usually lower) than host cation that also contributes in decreasing conductivity.

The delta phase of bismuth oxide, $\delta\text{-Bi}_2\text{O}_3$, is a very convenient model material for doped fluorite electrolytes in that it allows these individual effects to be understood separately. $\delta\text{-Bi}_2\text{O}_3$ has a fluorite-based crystal structure but it has six oxygen ions instead of eight (Figure 4-3(b)). Since Bi is a trivalent cation, for every two Bi cations, only three oxygen ions are required to balance it stoichiometrically. Therefore, the structure can be considered as a fluorite structure with an intrinsic deficiency of two oxygen atoms per unit cell. Although not strictly crystallographically correct since they are an intrinsic part of the structure, it is convenient to refer to the two unoccupied crystallographic sites that would be occupied in fluorite as “vacant sites” or “vacancies”. Because these vacancies are present in a stoichiometric structure, they are charge neutral. The presence of these intrinsic oxygen vacancies in $\delta\text{-Bi}_2\text{O}_3$ means that it has the oxygen vacancy density of a highly doped fluorite structure, however without the dopants themselves. As a result, in pure $\delta\text{-Bi}_2\text{O}_3$ the effects of dopant cation size and polarizability are absent, allowing the effects of the oxygen vacancies on the structure to be determined in isolation. In addition to being a model for highly-doped fluorite electrolytes, doped- Bi_2O_3 itself has considerable potential as SOFC material. In particular, DyWSB (Dy_2O_3 and WO_3 co-doped Bi_2O_3) has the highest ionic conductivity⁶² (0.53 S/cm at 500°C) among all the fluorite-based materials thus far characterized.

4.3.2 $\delta\text{-Bi}_2\text{O}_3$ Limitations

Although $\delta\text{-Bi}_2\text{O}_3$ is a promising material, it has still not found wide applications. One of the noticeable limitations from the conductivity plot (Figure 4-2) is its limited

phase stability. Pure δ - Bi_2O_3 fluorite phase is stable only over the very short temperature range between 825 °C and 730 °C; it melts beyond 825 °C⁶³ and transforms to a monoclinic phase below 730 °C.^{64,65} For its use in intermediate-temperature SOFC (IT-SOFC), melting is not as much a problem as is the phase transformation, upon which, the oxygen conductivity decreases considerably. Hence, the high conducting fluorite phase has to be stabilized at intermediate temperatures. Lanthanide dopants are added to δ - Bi_2O_3 to stabilize its high temperature fluorite phase at lower temperatures. However, doping concomitantly decreases its conductivity. A conductivity profile of yttria-stabilized δ - Bi_2O_3 in Figure 4-2 shows lower conductivity than pure δ - Bi_2O_3 . Nevertheless, it is still higher than other materials justifying its usage.

4.3.3 Ionic Radii or Polarizability?

Doping decreases the ionic conductivity of δ - Bi_2O_3 . A relative conductivity plot as a function of time (in hours) for different doped δ - Bi_2O_3 systems is shown in Figure 4-4. The conductivity profile for different dopants illustrates that time taken for decrease in conductivity varies for different dopants. While in Yb doped system, the relative conductivity decreases quickly, in Dy-doped system, the conductivity decay is less marked. As discussed above, two possible factors for decreased conductivity are different dopant radius and polarizability from host cation. To elucidate their individual effect, Figure 4-5 shows plots of the conductivity decay time constant as a function of dopant radius (Figure 4-5(a)) and polarizability (Figure 4-5(b)). Time constant is defined as the time taken for significant conductivity decrease. Both plots show that the time constant follows a linear dependence on the cation radius and polarizability. Collectively, it means that as the ionic radii and polarizability are increased, the conductivity decrease is less

severe. However, the individual effect of either radii or polarizability cannot be elucidated separately as both increase linearly and simultaneously for any given dopant.

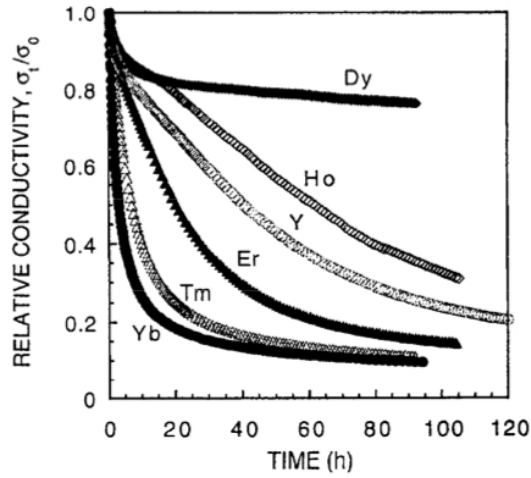


Figure 4-4. Relative conductivity of δ - Bi_2O_3 doped with different dopants. The time taken for conductivity decrease varies for different dopants. (Reproduced from reference 66)

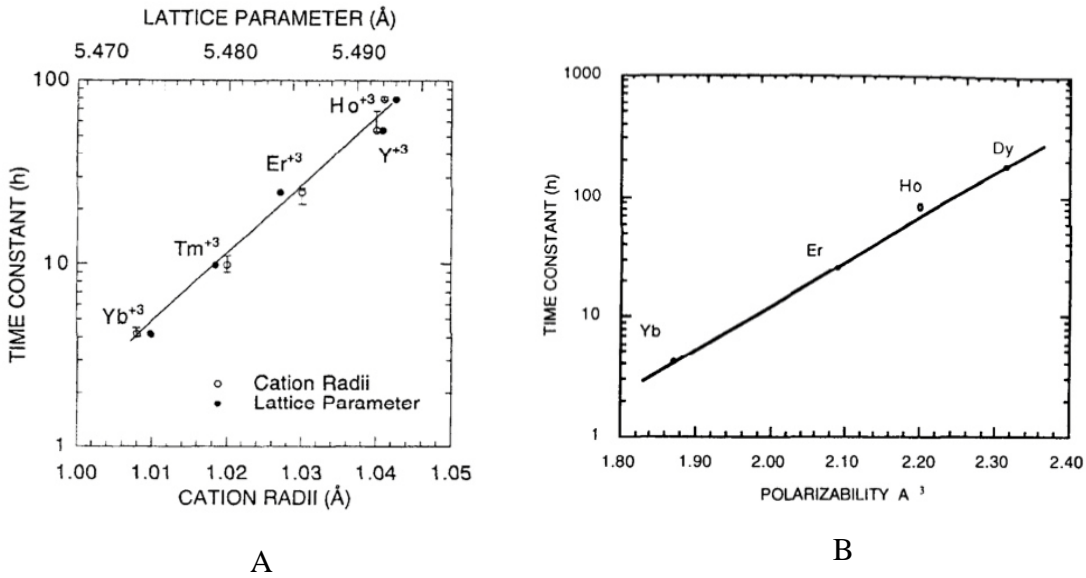


Figure 4-5. Comparison of time constant for different doped δ - Bi_2O_3 systems. The dopants are characterized based on (A) cation radii and (B) polarizability. (Reproduced from references 67 and 66)

To engineer better materials for longer-lasting conductivity, understanding the individual effect of either is necessary; while experiments are limited on this front, computer simulations prove very useful.

4.4 Simulation Methodology

Conventional MD simulation methods as discussed in chapter 3 are used with the interactions between ions described by a combination of electrostatic interactions between the ions, and empirical potentials to describe the short-ranged, mainly repulsive, interactions. The form of Jacobs and MacDónaill,⁶⁸ is adopted in which the interactions are:

$$V(r) = \frac{Z_1 Z_2 e^2}{r} + A \exp\left(-\frac{r}{\rho}\right) + B \exp\left(-\frac{r}{\sigma}\right) - \frac{C}{r^6} \quad (4-3)$$

As discussed in chapter 2, the first term in the potential describes the Coulombic interactions; r is the separation between two ions of charges Z_1 and Z_2 respectively; e is the charge on an electron. The second and third terms are short ranged repulsive interactions, parameterized by A , B (energy scales for the repulsive interactions), and ρ and σ (the range of the repulsive interactions). The last term is the attractive Van der Waals interactions characterized by C . The parameters A , B , ρ , σ and C were fitted to experimental values of pertinent physical properties, including the lattice parameter, high frequency dielectric constant for α and γ phases, and the cohesive energies. The details of the potential can be found in Jacobs and Mac Dónaill.⁶⁸ The potential parameters for the Bi-Bi, Bi-O, and O-O are given in Table 4-2. The polarizability of the ions can be accounted for via the shell model,⁴³ as discussed in Chapter 3; the atom consists of a shell of charge Y/e which moves with respect to the massive core of charge X/e .

Table 4-2. Parameters for the short-range potential for δ -Bi₂O₃ from Jacobs and Mac Donail⁶⁸

	A (eV)	ρ (Å)	B (eV)	σ (Å)	C (eV/Å ⁶)
O ²⁻ - O ²⁻	1290.0	0.3011	47683.4	0.14438	71.3
Bi ³⁺ - Bi ³⁺	15983.1	0.25643	3087441.4	0.10406	40.36
Bi ³⁺ - O ²⁻	323.0	0.41631	5745.0	0.27279	0.00

The shell and the core are attached by a harmonic spring with force constant k . In the presence of an internal or external electric field, the displacement of the shell with respect to the core describes the polarizability of the ion, given by equation 3-22. The values of Y and k are also taken from Jacobs and Mac Dónail.⁶⁸ For Bi³⁺, $Y=-30.0$ and $k=6600.0$ eV Å⁻² and for O²⁻, $Y=-3.0$ and $k=33.0$ Å⁻².

The simulation cell consists of a cubic arrangement of 4x4x4 non-primitive cubic unit cells, each cell containing four bismuth and six oxygen atoms for a total of 640 atoms. Periodic boundary conditions are applied in all three spatial directions. Before starting the simulation, the oxygen vacancies are randomly distributed on the tetrahedral sites. The time step of 0.05 fs is smaller than is typically used, so as to ensure good energy conservation in microcanonical ensemble simulations.

4.5 Results

4.5.1 Polarizability Indeed

Using shell model⁴³ MD simulation, it is possible to create artificial dopants in which the ionic polarizability can be varied while keeping the ionic radii constant, and vice-versa. Keeping one constant and varying the other can disentangle the individual effect of either. Figure 4-6 shows a plot of the ionic radii and calculated polarizabilities of corresponding ions. The radii of the ions are taken from Shannon⁶⁹ and the polarizabilities

are derived from the relationship between polarizability α , and ionic radius r , (to account for Coulombic screening of outer electrons by $4f$ electrons) as given by Shirao *et al.*:⁷⁰

$$\alpha_{\infty} = -1.375 + 3.176r^3 \quad (4-2)$$

Using this relationship, the plot illustrates that the dopants added to $\delta\text{-Bi}_2\text{O}_3$ have radius and polarizability considerably less than Bi.

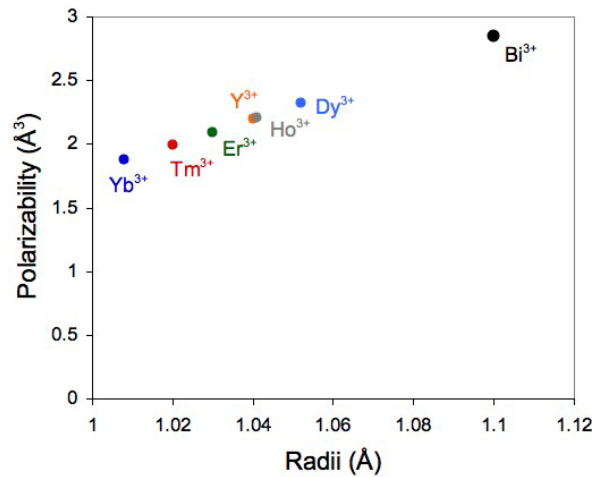


Figure 4-6. Ionic radius and polarizability of different dopants added in $\delta\text{-Bi}_2\text{O}_3$. Both radius and polarizability of all dopants are considerably less than Bi.

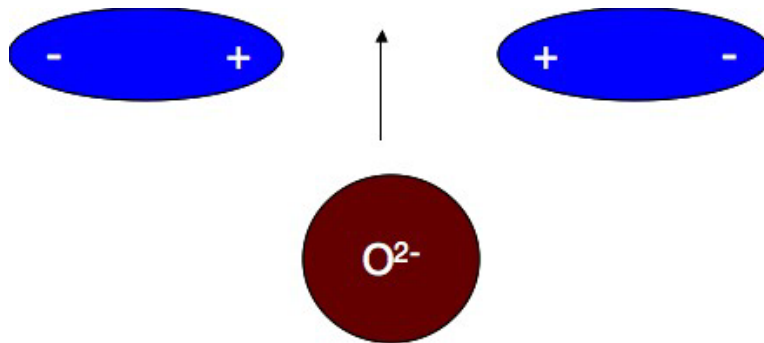


Figure 4-7. Oxygen ion diffusion through two Bi ions (shown in blue). The displacement of electronic cloud by Bi ions facilitates oxygen diffusion.

To understand a physical effect of polarizability, a schematic representation of oxygen ion diffusion through two Bi ions is shown in Figure 4-7.

If Bi ions are polarizable, one can imagine that diffusion of a negatively-charged oxygen ions would be facilitated if the negatively-charged electronic cloud of Bi ions can displace itself away from the oxygen ion. With away electronic displacement, oxygen ion faces less repelling force and hence can easily diffuse through two Bi ions. Therefore, higher ionic polarizability may facilitate higher oxygen diffusion. This is characterized in the next section.

4.5.1.1 Polarizable and non-polarizable ions

Using MD simulation, two different systems distinguished by ionic polarizability are modeled. In one system, the ions (Bi and O in $\delta\text{-Bi}_2\text{O}_3$) are kept fully polarizable, while in the other, both are treated as completely non-polarizable. A varying degree of polarizability can be understood from the schematic representation Bi ion in Figure 4-8. A rigid ion model in Figure 4-8 (a) represents a non-polarizable Bi ion with $\alpha_{\text{Bi}} = 0$. Figures 4-8 (b) and (c) represent weakly and strongly polarizable models of Bi ions respectively.

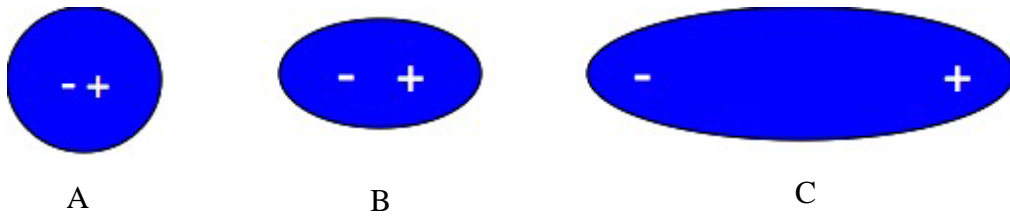


Figure 4-8. Gradually increasing Bi polarizability. A) non-polarizable, B) weakly polarizable and C) strongly polarizable.

In the presence of electric field, the electronic cloud of a non-polarizable model remains un-effected. . In contrast, a weakly polarizable and a strongly polarizable models alter their electric fields corresponding to their degree of polarizability.

A fully-polarizable $\delta\text{-Bi}_2\text{O}_3$ model represents real $\delta\text{-Bi}_2\text{O}_3$, whereas, a non-polarizable system represents an idealized case of lower polarizable dopant system. In the simulations, the radii of the ions are kept constant in both systems. Mean square displacement (MSD) of the oxygen ions is used as the physical property to distinguish the effect of ion radii or polarizability on oxygen diffusion. MSD is related to diffusivity by the relationship given in equation 2-19. During the simulation, oxygen ions are the only ones that diffuse; since bismuth ions have no vacant sites for diffusion, they vibrate at their respective positions. The MSD profiles of oxygen in two systems are given in Figure 4-9. As expected, a fully-polarizable system ($\alpha_{\text{Bi}} = 2.85\text{\AA}^3$ and $\alpha_{\text{O}} = 3.92\text{\AA}^3$) allows continuous oxygen diffusion, as given by a linear MSD profile (Figure 4-9(a)).

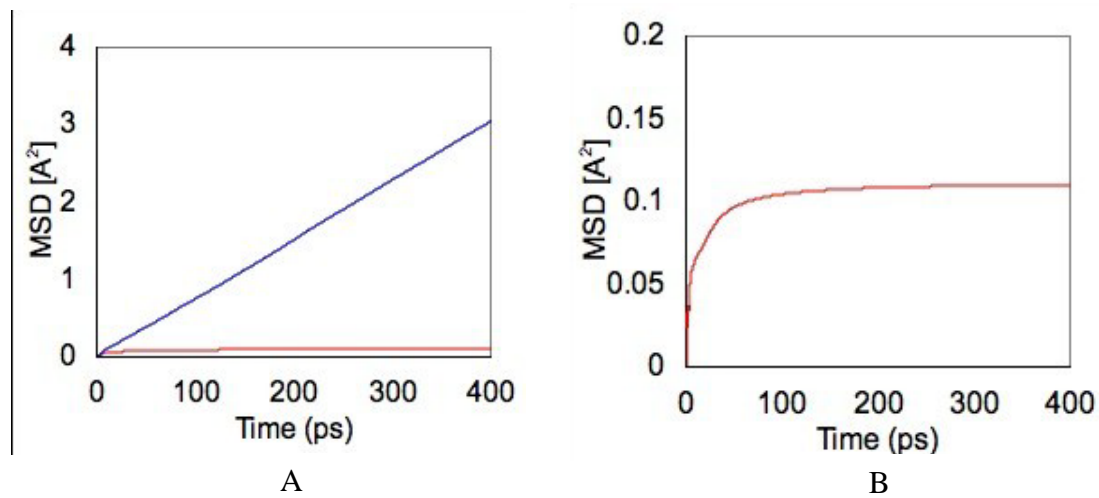


Figure 4-9. Mean-squared displacement (MSD) of oxygen in polarizable and non-polarizable $\delta\text{-Bi}_2\text{O}_3$. A) Constant increase in MSD is observed in polarizable $\delta\text{-Bi}_2\text{O}_3$ compared with non-polarizable $\delta\text{-Bi}_2\text{O}_3$ where the diffusion stops after < 150 ps. B) A magnified view of the oxygen MSD in the non-polarizable $\delta\text{-Bi}_2\text{O}_3$.

In contrast, oxygen diffusion is very limited in the non-polarizable system. The oxygen atoms diffuse only for first few pico-seconds (< 150 ps) during which the system equilibrates. After equilibration, the oxygen diffusion essentially ceases as shown by the

plateau in the MSD plot (Figure 4-9 (b)). As characterized later in chapter 5, this rapid cessation of oxygen diffusion is a result of the development of a vacancy-ordered structure. By contrast, in the polarizable $\delta\text{-Bi}_2\text{O}_3$, there is no such vacancy ordering on the time scale of MD simulations (0.5 nanoseconds). This qualitative difference in the behavior of the polarizable and non-polarizable systems clearly identifies the polarizability of the ions as being a determinant of the diffusion behavior.

4.5.1.2 Only-oxygen ions polarizable

To further distinguish the effect of the cation and anion polarizability, similar simulations are performed in which, one of the ions (either cation or anion) is treated as polarizable and other is treated as non-polarizable.

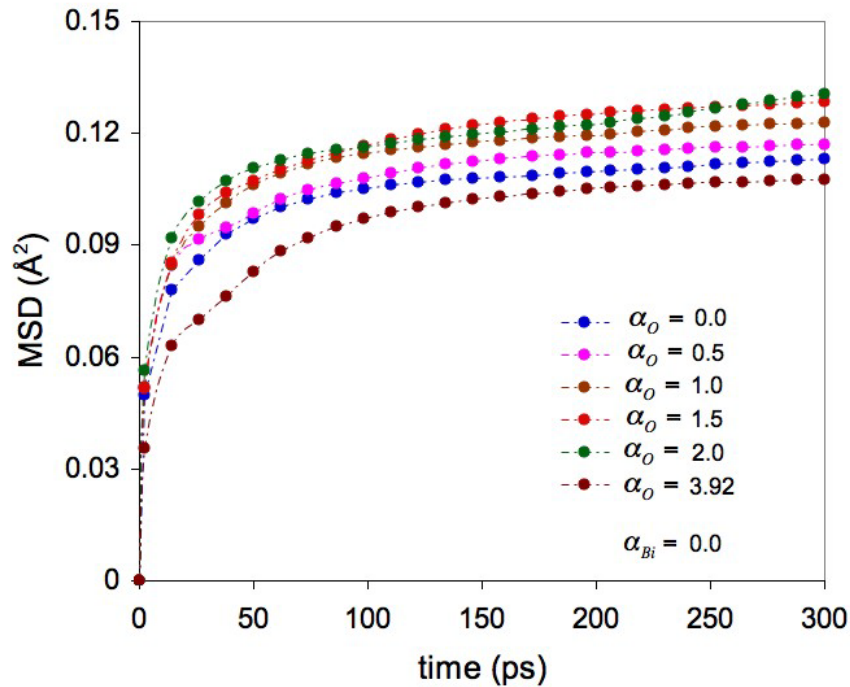


Figure 4-10. MSD of the oxygen ions in different systems with gradually increasing oxygen polarizability. Bismuth ions are kept non-polarizable. MSD profile matches with the Figure 4-9 (b) suggesting that oxygen polarizability has little effect on oxygen diffusion.

Figure 4-10 shows the MSD of the oxygen ions for the system where bismuth ions are treated as non-polarizable ($\alpha_{Bi} = 0$) and the oxygen polarizability is increased gradually in different systems. To put into context, $\alpha_{Bi} = 0 \text{ \AA}^3$ means that the Bi ions are treated as rigid atoms and the electron cloud (or the shell in shell-model) does not respond at all to the electric field. In the same way, $\alpha_O = 0 \text{ \AA}^3$ treats oxygen as a rigid atom. $\alpha_O = 3.92 \text{ \AA}^3$ is the real oxygen polarizability observed experimentally.⁷¹ The MSD profile for various systems shows a similar behavior to that of the non-polarizable system in Figure 4-9 (b). Once the vacancy ordered structure is formed, the oxygen diffusion ceases after the system equilibrates and MSD reached a plateau. This illustrates that oxygen polarizability does not control oxygen diffusion. In contrast, when polarizability on ions is reversed, i.e., when bismuth ions are gradually polarized and oxygen ions are treated as non-polarizable, it reveals a different behavior.

4.5.1.3 Only-bismuth ions polarizable

A gradual increase in the bismuth polarizability gradually increases oxygen diffusion. Figure 4-11 shows oxygen MSD for the gradually increasing bismuth polarizability while keeping zero oxygen polarizability ($\alpha_O = 0$). The bottom-most line in Figure 4-11 is the MSD profile for the non-polarized bismuth system, which is same as seen above in Figure 4-9 (b). Gradually increasing the Bi polarizability increases the oxygen diffusion by a corresponding amount. The most polarizable (shown in red) bismuth system's MSD matches with the fully polarizable system in Figure 4-9 (a). The simulations further indicate that there is a certain minimum ionic polarizability required to prevent vacancy ordering. In particular, below a critical polarizability, ordering takes place on an MD-accessible time scale, while for higher polarizabilities, there is

considerable diffusion, with no sign of vacancy ordering. This elucidates the reasoning behind the vacancy ordering observed experimentally when Bi_2O_3 is doped. Hence, this suggests that bismuth (cation) polarizability is most significant to oxygen diffusion.

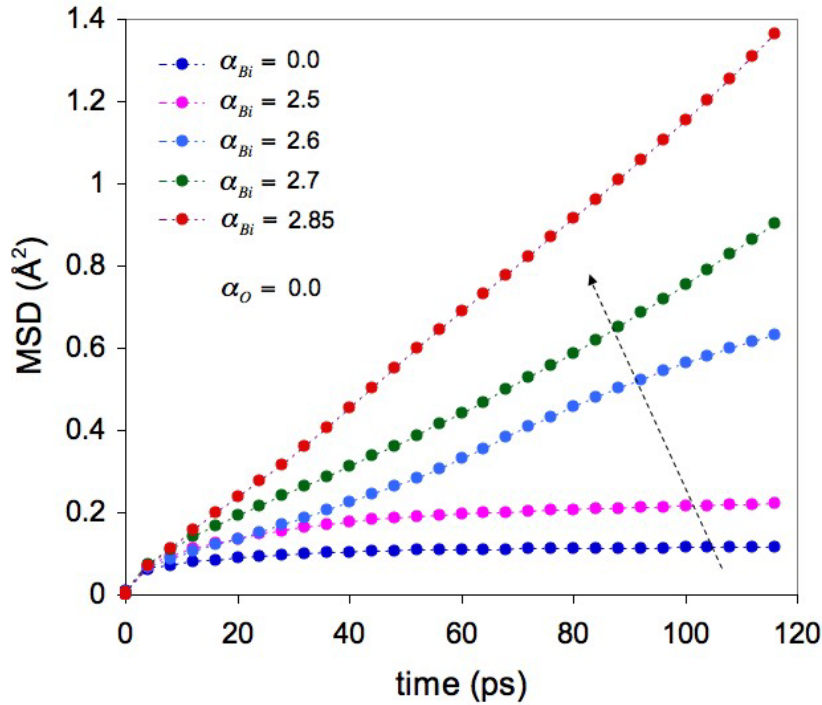


Figure 4-11. MSD of the oxygen ions in different systems with gradually increasing bismuth polarizability. Here, oxygen ions are kept non-polarizable. MSD profile increases gradually as bismuth polarizability is increases. The most polarizable bismuth system matches with Figure 4-9 (a) suggesting that bismuth polarizability is important for high oxygen diffusion.

Taken together, simulations elucidate that high polarizable dopants should be considered for phase stabilization to achieve high conductivity.

4.5.2 Oxygen Diffusion Mechanism

In this section, the oxygen diffusion in a crystallographic direction in Bi_2O_3 is discussed. In a Bi_2O_3 unit cell, to occupy a vacancy, oxygen atoms can diffuse in three different directions, (a) $\langle 100 \rangle$, (b) $\langle 110 \rangle$ and (c) $\langle 111 \rangle$. They are schematically shown in Figure 4-12. In Figure 4-12, any of the six oxygen atoms having sufficient activation

energy can make a jump to occupy either of the two available vacancies. In a unit cell, $\langle 100 \rangle$ is the shortest diffusion path ($=0.5a_0$), $\langle 110 \rangle$ has intermediate diffusion path length along the face diagonal of oxygen sub-lattice ($\sqrt{2}/2 a_0$) and $\langle 111 \rangle$ has the longest path length along the body diagonal of oxygen sub-lattice ($\sqrt{3}/2a_0$).

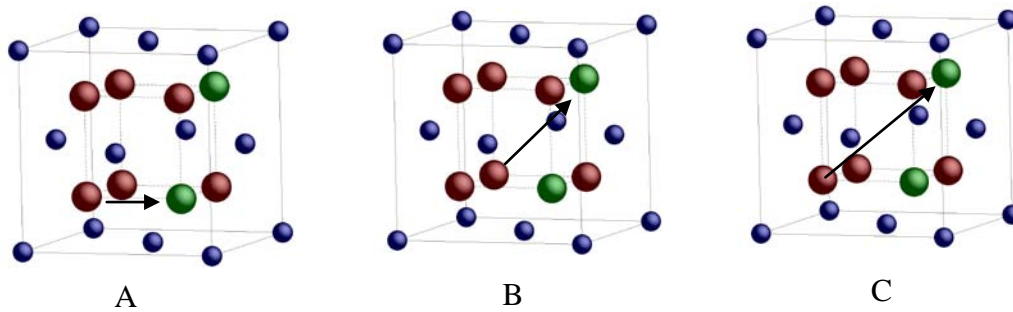


Figure 4-12. Possible oxygen diffusion directions. A) $\langle 100 \rangle$, B) $\langle 110 \rangle$ and C) $\langle 111 \rangle$.

Using MD simulations, the path of any migrating atom can be followed and the prominent diffusion direction can be statistically calculated. From multiple simulations, it is found that oxygen ion prefers to diffuse along $\langle 100 \rangle$ diffusion direction. A time averaged plot of Bi and O atoms in the unit cell is shown in Figure 4-13. A three-dimensional and a two-dimensional view of the unit cell are shown Figures 4-13(a) and 4-13 (b) respectively. The time-averaged path of all Bi atoms is shown in black color and all other colors represent oxygen atoms. The paths of all Bi atoms are limited around ideal Bi positions, thus illustrating only small atomic vibration with no diffusion jump. Similar to Bi atoms, the time-averaged path of five oxygen atoms, i.e., two shown in dark blue, one each in light blue and green, and one of the two in red show vibration at their corresponding sites. These five oxygen atoms do not diffuse for the MD time represented in this plot. The sixth oxygen atom in the unit cell undergoes two diffusion jumps marked as 1 and 2 and shown in pink and red lines respectively. In both diffusion processes,

oxygen jumps in $\langle 100 \rangle$ direction. Two-dimensional view of these diffusion processes clearly show $\langle 100 \rangle$ jumps.

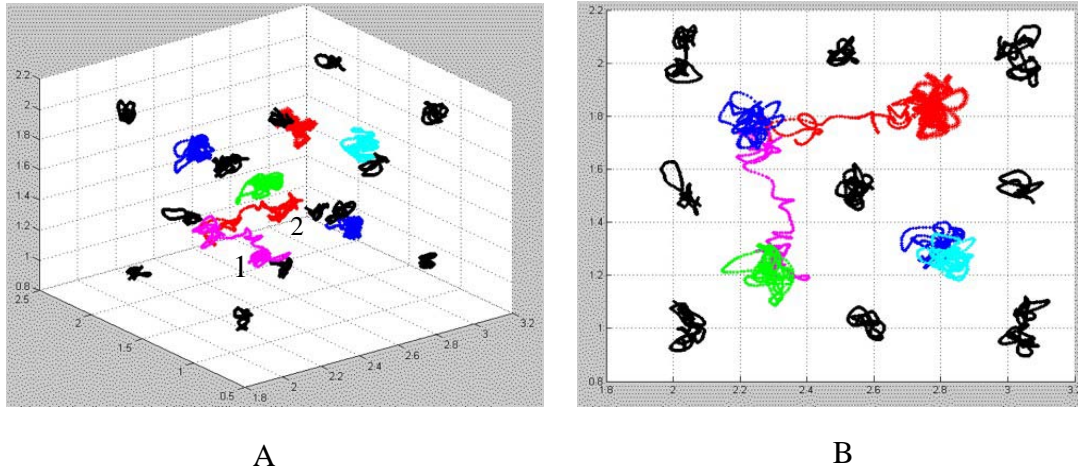


Figure 4-13. Oxygen diffusion mechanism. A) A 3-D representative view of time-averaged position of Bi and O atoms in a unit cell. Bi positions are shown in black and oxygen in other colors. Out of six oxygen atoms, five vibrate at their corresponding positions. One oxygen atom diffuses in $\langle 100 \rangle$ direction. It makes two jumps in the diffusion path shown by lines in pink and red. B) A 2-D plot of same oxygen atom making two jumps.

4.6 Discussion

According to Boyapati *et al.*,⁷² doped δ -Bi₂O₃ forms an ordered structure below 600°C in which the vacancies tend to order in $\langle 111 \rangle$ (occupational ordering), with concomitant oxygen displacement (positional ordering). The occupational and the positional ordering increase as smaller and less polarizable dopants (e.g., Yb³⁺ and Er³⁺) are added, which result in a decrease in the oxygen conductivity. These dopants have been observed to lead to shorter time constants for oxygen ordering than the time constants associated with bigger and more polarizable dopants, such as Dy³⁺. In addition, for Dy³⁺ doped systems Boyapati *et al.* did not observe complete ordering with ageing. This means that even at relatively low temperatures, the formation of vacancy ordered structure can be prevented by the presence of larger and more polarizable dopants. While the system simulated is different in that there are no dopants, the simulation results are

consistent with these experiments. The simulations show that polarizability is much more important for high conductivity. Further, the simulations for the fully-polarizable system show no indication of either kinds of ordering. In contrast, the non-polarizable system (the extreme limit of low polarizability; low polarizability ions Yb^{3+} and Er^{3+}) produce both occupational and positional ordering in doped Bi_2O_3 . Hence, MD simulation elucidates the reasoning behind loss of conductivity with time. The occupational ordering will be discussed (vacancy ordering) in Chapter 5. The implication of vacancy ordering on the structure will be discussed in Chapter 6 when the ions' displacement from crystallographic viewpoint is discussed. This constitutes positional ordering.

Oxygen diffusion direction was previously observed experimentally by Boyapati *et al.*⁷³ Similar to observation made here, they also observed $\langle 100 \rangle$ direction as prominent oxygen diffusion direction. They further showed that exact oxygen path is not along straight $\langle 100 \rangle$ direction but is curved, i.e., the oxygen atom diffuses through the empty octahedral position in the center of the unit cell. However, results observed here are partly in agreement. The preferential diffusion is along $\langle 100 \rangle$ essentially along straight line with no indication of oxygen passing through octahedral site. It is important to mention there that this diffusion illustration is for the non-polarizable system (Figure 4-8(b)). The exact oxygen diffusion path in the simulated polarizable system could differ, i.e., might occur through octahedral site, as was the case in the systems considered by Boyapati *et al.*

CHAPTER 5
VACANCY-ORDERED STRUCTURE OF CUBIC BISMUTH OXIDE

5.1 Introduction

In the previous chapter, using MD simulation, it is found that the non-polarizability of ions leads to oxygen diffusion cessation. In this chapter, the implications of cessation on the structure of $\delta\text{-Bi}_2\text{O}_3$ is discussed. Evidently, the cessation is related to the ordering of the vacancies intrinsically present in $\delta\text{-Bi}_2\text{O}_3$. On the one hand, diffusing oxygen vacancies contribute to high oxygen diffusivity; however, on the other, their ordering limits it. In this chapter, the focus is on the non-polarized ionic system of $\delta\text{-Bi}_2\text{O}_3$ to elucidate the vacancy-ordering mechanism, and the structural changes that occur in $\delta\text{-Bi}_2\text{O}_3$.

Up to this point, MD is used to analyze the system. It has allowed to observe oxygen diffusion at high temperatures in a large system of atoms. However, it is well known that MD methods are intrinsically limited in their materials fidelity. By contrast, electronic structure methods, particularly density-functional theory (DFT) approaches are known to give a much better description of materials structure. Hence, in this chapter, both MD and DFT are used to provide further corroboration for the structure determined from MD simulations and experiments.

A non-primitive unit cell of $\delta\text{-Bi}_2\text{O}_3$ is shown in Figure 4-3 (b). Similar to fluorite crystal structure, bismuth ions form a FCC network and oxygen ions sit at the tetrahedral sites. As also mentioned previously, $\delta\text{-Bi}_2\text{O}_3$ has six oxygen ions instead of eight, leaving two vacant sites (vacancies). These vacancies can be at any of the eight available anion sites. If the vacancies were to form a simple ordered array, it would seem likely that they would order along $\langle 100 \rangle$, $\langle 110 \rangle$ or $\langle 111 \rangle$ directions, i.e., $\langle 100 \rangle$ as first nearest

neighbors, $\langle 110 \rangle$ as second nearest neighbors, and $\langle 111 \rangle$ as third nearest neighbors. The structure of $\delta\text{-Bi}_2\text{O}_3$ has therefore been a subject of considerable discussion, and various models have been put forward with particular interest focusing on possible ordering of vacancies.^{63,68,74,75,76}

The Gattow model, posits equal possibility of tetrahedral site occupancy by oxygen ions, i.e., the oxygen sub-lattice is completely disordered and there is no preferential vacancy ordering (Figure 5-1 (a)). In contrast, according to the Sillen model the oxygen sub-lattice is completely ordered, i.e., vacancies are preferentially ordered in the $\langle 111 \rangle$ directions (Figure 5-1 (b)). These models are in complete disagreement to each other. Furthermore, they focus only on the site occupancy and do not discuss the possible oxygen displacements. The Willis model⁷⁴ accounts for such displacements that each oxygen ion is displaced from regular tetrahedral 8c site in $\langle 111 \rangle$ direction towards the face of the tetrahedron (Figure 5-1 (c)). In the unit cell, there are eight tetrahedral positions and each tetrahedron has four faces. There are therefore 32 equivalent positions (32f) to which oxygen ions can displace. Since, there are only six oxygen ions in the unit cell, it gives occupancy of 3/16. In this manner, the Willis model accounts for the oxygen displacement but lacks an accounting for the vacancy occupancy. Hence, in Figure 5-1 (c), only the displacement of oxygen in $\langle 111 \rangle$ direction towards one of the tetrahedron faces is shown, and not the positioning of vacancies. Hence, while the Willis model accounts for positional ordering (oxygen displacement), Gattow and Sillen models account for occupational ordering (vacancy ordering). Individually however, none of the three models are self-contained in describing the structure completely. Furthermore, these models do not discuss about the cation displacements.

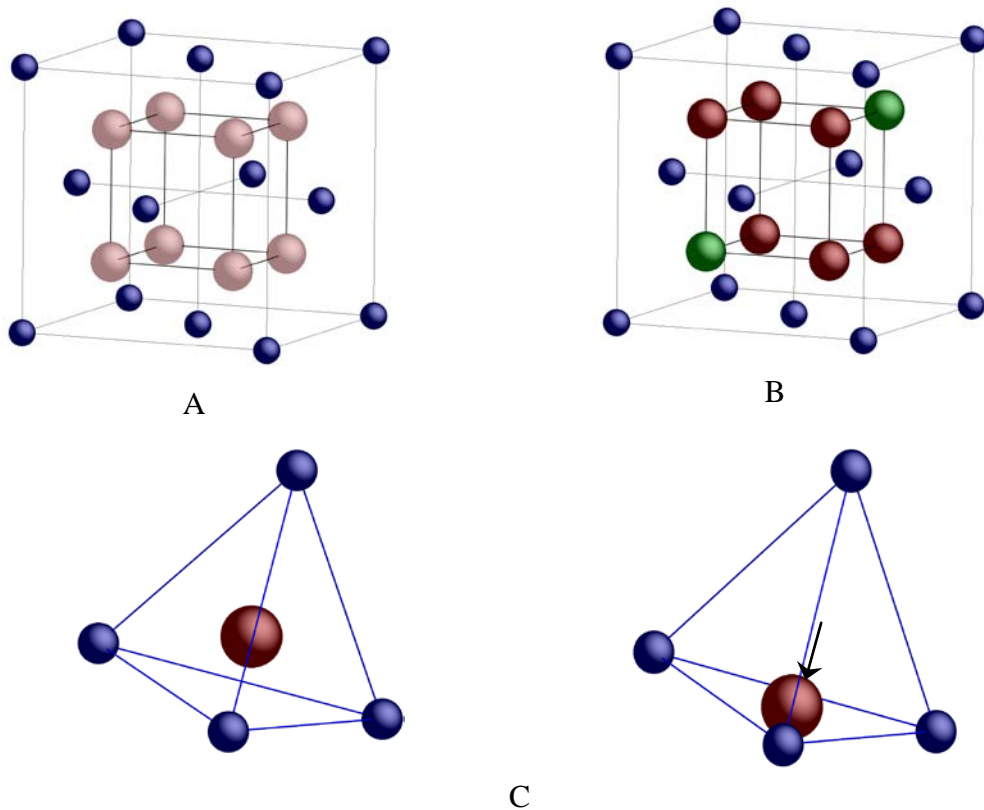


Figure 5-1. Three different models of $\delta\text{-Bi}_2\text{O}_3$. A) Gattow model – all sites have equal occupancy (in the schematic no vacancies are shown; equal probability is shown by oxygen in lighter color). B) Sillen model – vacancies order in $\langle 111 \rangle$ direction. C) Willis model – Oxygen displaces in $\langle 111 \rangle$ direction towards the face of the Bi tetrahedron. In (C), only the displacement of oxygen atoms is shown. Willis model does not account for the positioning of vacancies.

Recently, from analysis of neutron-diffraction experiments, Boyapati *et al.*⁷² concluded that the vacancies in doped- Bi_2O_3 order along $\langle 111 \rangle$ with additional ordering in $\langle 110 \rangle$ direction, thus accounting for occupational ordering. Moreover, neutron scattering showed that the oxygen ions are displaced from the 8c sites, with the data refinement being consistent with displacement to the 32f sites.⁷² This accounts for positional ordering. However, in contrast to these experiments, Walsh *et al.*⁷⁶ more recently reported from DFT calculations that the vacancies prefer nearest neighboring,

i.e., $\langle 100 \rangle$ ordering; they did not however explore the structure proposed by Boyapati *et al.* These results might not necessarily contradict each other because the experiments were performed on doped systems, while the DFT calculations were performed on pure $\delta\text{-Bi}_2\text{O}_3$. However, by exploring only three possibilities, i.e., $\langle 100 \rangle$, $\langle 110 \rangle$ and $\langle 111 \rangle$ and not the one observed by Boyapati *et al.*, it appears that although $\langle 100 \rangle$ could be energetically the lowest among the three, but perhaps not the lowest structure of all.

This inconsistency is explored by comparing the experimentally consistent MD results with DFT calculations. It is found that the vacancy ordering in combined $\langle 110 \rangle$ and $\langle 111 \rangle$ predicted by experiments and MD simulation is consistent with DFT calculations (shown later). Moreover, the results in the previous DFT calculations by Walsh *et al.* were due to small system size (only one unit cell) considered for calculations. It is found that diffusion cessation in non-polarizable ionic system forms combined vacancy ordering and it is this ordering that is observed in experiments consistent with DFT. Therefore, in this chapter, use both MD simulations and DFT calculations to provide a unified view of the defect structure of cubic $\delta\text{-Bi}_2\text{O}_3$.

5.2 Ordering of the Vacancies: MD Simulation

Recalling the MD simulation methodology, before starting the simulation, a $4 \times 4 \times 4$ unit cell system was generated by randomly placing the vacancies with no site preference. All the atoms were also placed at the crystallographic positions. This structure was then equilibrated at high temperature to allow oxygen diffusion. After only few oxygen jumps, the structure thus obtained after oxygen diffusion (in the tail end of Figure 4-9(b)) is the one that is analyzed here.

5.2.1 Neighboring Vacancies of a Vacancy

For the purpose of this analysis, the vacancies are assumed to sit at the crystallographic site (8c) of the missing oxygen atom. The vacancy sub-lattice is then defined by the pattern of ordering of the vacancies. To understand the nature of this ordering, the focus is on the vacancy-vacancy neighbors. A pair distribution function (PDF), averaged over all vacancies, for the neighboring vacancies of a vacancy is given in Figure 5-2. Because the vacancies are randomly placed in the initial structure (non-equilibrated structure) the resulting PDF in Figure 5-2(a) is exactly what one would expect from a statistical analysis of such a random structure, with peaks at all the cubic neighbor distances of 0.5, 0.707, 0.866, 1.0 a_0 etc., with heights in accord with statistical expectations.

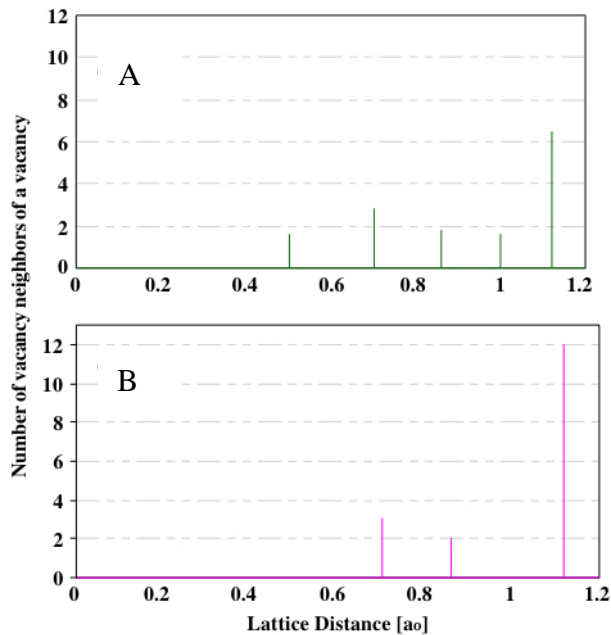


Figure 5-2. Vacancy-vacancy pair-distribution function. A) Non-equilibrated structure. B) equilibrated structure.

As is evident from Figure 5-2(b), the equilibrated structure is very different. The PDF of each individual vacancy is identical to that shown in Figure 5-2(b), demonstrating that all

vacancies are crystallographically identical to each other. Particularly important is the absence of peaks at $0.5a_0$ and $1a_0$; this indicates that there are no vacancy-vacancy nearest neighbors along $\langle 001 \rangle$. On the other hand, every vacancy has three vacancy neighbors in the $\langle 110 \rangle$ directions. These $\langle 110 \rangle$ vacancies form an equilateral triangle with the central vacancy (CV) at the center, as shown in Figure 5-3. In addition, there are two vacancies in the $\langle 111 \rangle$ directions normal to the plane of $\langle 110 \rangle$ vacancies, and in opposite directions relative to the CV (Figure 5-3). Hence, the structure of $\delta\text{-Bi}_2\text{O}_3$ has a combined ordering of the vacancies in $\langle 110 \rangle$ and $\langle 111 \rangle$ directions.

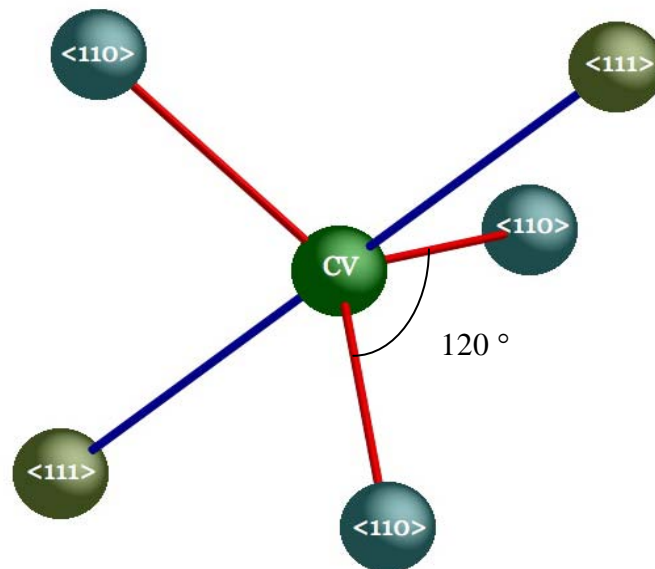


Figure 5-3. A central vacancy (CV) is surrounded by three $\langle 110 \rangle$ vacancies and two $\langle 111 \rangle$ vacancies. This is a repeating configuration of the vacancies throughout the system.

This vacancy ordering mechanism is consistent with the “occupational ordering” observed in neutron scattering experiments⁷³ of doped $\delta\text{-Bi}_2\text{O}_3$. Recalling the result from Walsh *et al.* where $\langle 100 \rangle$ was suggested to be the prominent vacancy-ordering mechanism, the high temperature equilibration MD simulations show that in fact $\langle 100 \rangle$ does not exist at all. Instead a combination of other two ordering directions is prevalent.

5.2.2 Continuous Ordered Structure of Vacancies

Neighboring vacancies do not form clusters but a continuous network throughout the system both in $\langle 111 \rangle$ and in $\langle 110 \rangle$ directions. To represent the continuous network of $\langle 110 \rangle$ vacancies, the oxygen sub-lattice is focused. Since, there are three $\langle 110 \rangle$ vacancy neighbors of a vacancy, continuous chains of vacancies are present in all three $\langle 110 \rangle$ directions. Two such chains are shown in Figure 5-4(a). Two of the three $\langle 110 \rangle$ vacancy neighbors of every vacancy are shown here; the third neighbor is in the direction normal to the plane of the figure. The network formed by the $\langle 111 \rangle$ ordered vacancies is shown in Figure 5-4(b).

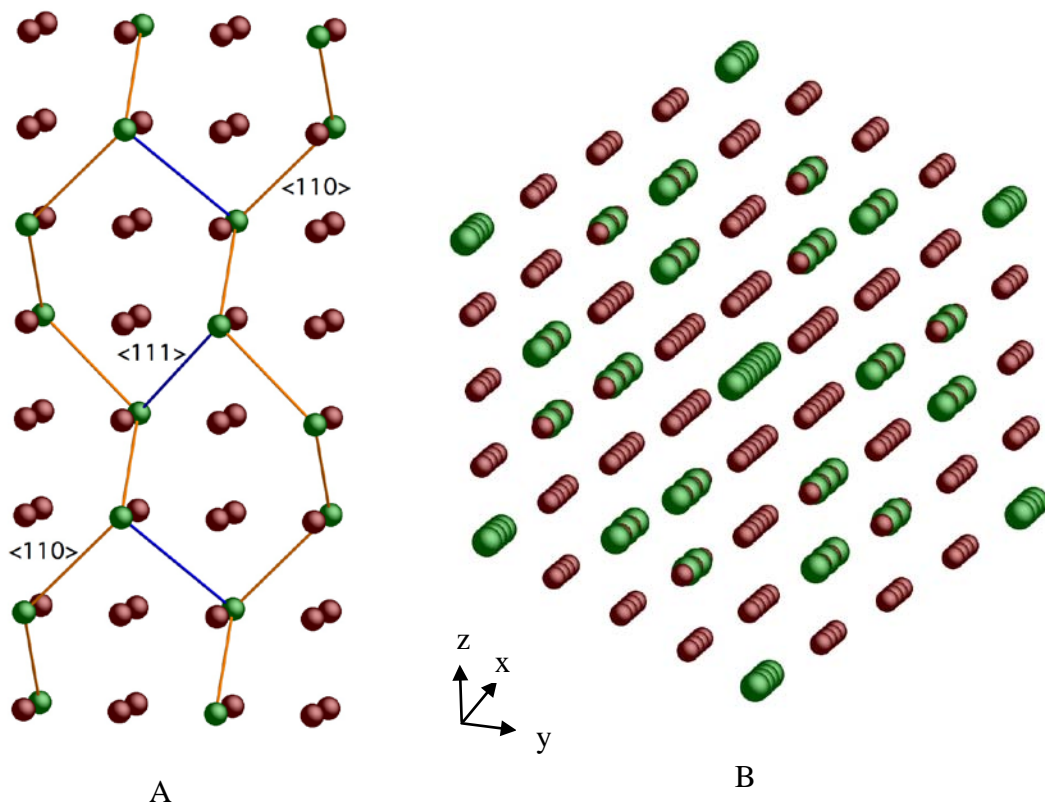


Figure 5-4. A continuous network of vacancies in the oxygen sub-lattice. A) Two parallel chains of $\langle 110 \rangle$ network of vacancies (shown in orange) connected by $\langle 111 \rangle$ -ordered vacancies (shown in blue). B) $\langle 111 \rangle$ network of vacancies creating an open channel through the system.

This continuous network of vacancies in $\langle 111 \rangle$ is simultaneously present in all the four families of $\langle 111 \rangle$ directions. The $\langle 111 \rangle$ network of vacancies acts as a connection between two parallel chains of $\langle 110 \rangle$. As a result, one ordering network is directly connected to another. It is important to recognize that although there are open channels of vacancies available for easy oxygen diffusion along the $\langle 111 \rangle$ network, the oxygen diffusion is limited by preferential oxygen diffusion in $\langle 100 \rangle$ directions. Because a combined ordering in $\langle 110 \rangle$ and $\langle 111 \rangle$ is not possible in a single unit cell, a $2 \times 2 \times 2$ system of unit-cells is required to observe the complete ordering phenomenon. This is the reason that while working with only one unit cell, Walsh *et al.* did not observe this combined ordering mechanism.

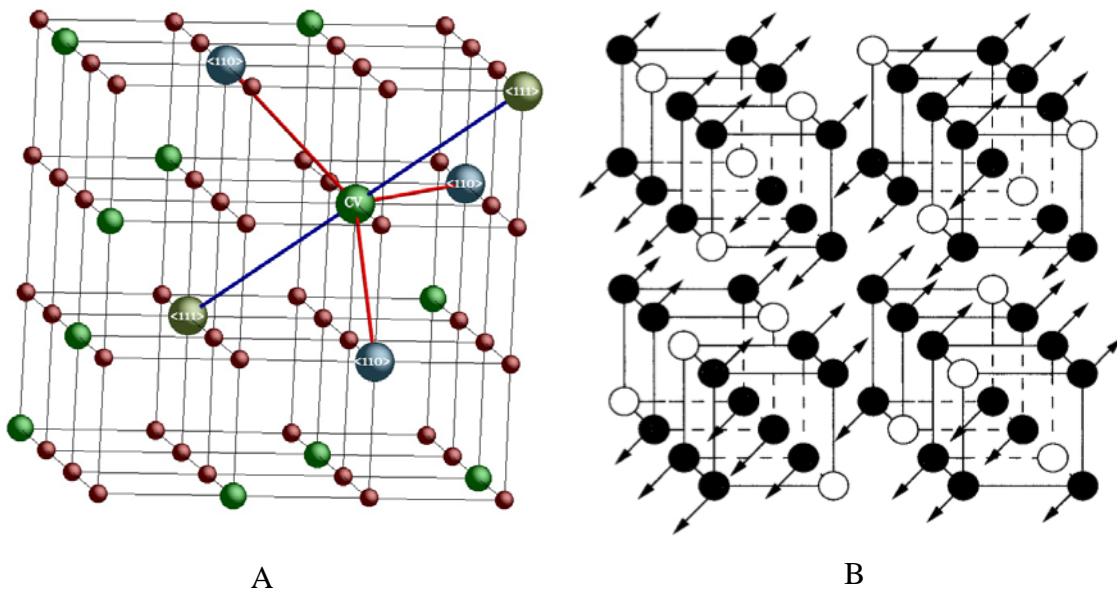


Figure 5-5. A $2 \times 2 \times 2$ fluorite superstructure with a combined vacancy ordering in $\langle 110 \rangle$ and $\langle 111 \rangle$ directions. A) Simulation. B) Experiment (reproduced from reference 75). The vacancy-ordering mechanism from MD simulation agrees with experiment.

The 2x2x2 fluorite-related superstructure determined from simulations is shown in Figure 5-5; this superstructure is completely consistent with the structure determined from the analysis of electron⁷⁵ and neutron diffraction experiments.⁷²

5.2.3 Expansion and Contraction of the Tetrahedron

Although there are numerous ways in which the structure of $\delta\text{-Bi}_2\text{O}_3$ can be visualized, it is particularly instructive to consider the tetrahedron formed by four bismuth atoms. Each of these tetrahedrons encloses either an oxygen atom or a vacancy. Every Bi atom sits at the corner of eight tetrahedron, six of which contain oxygen atoms, two of which contain vacancies. The Bi-Bi inter-atomic distances are different in the two cases. Figure 5-6 shows the Bi-Bi PDF for the equilibrated system.

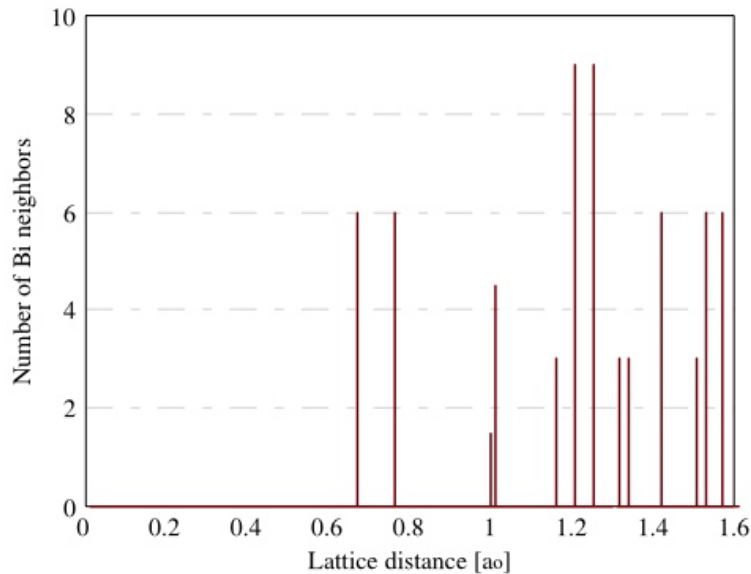


Figure 5-6. Bi-Bi pair distribution function. Two different first nearest neighbors distances are represented by the first two peaks of equal height.

There are two distinct nearest-neighbor distances, corresponding to Bi-Bi separations of $0.67a_0$ and $0.76a_0$ in comparison to one $0.707a_0$. If there is an oxygen atom inside the tetrahedron (Figure 5-7(a)) then four out of the six Bi-Bi inter-atomic distances are short ($0.67a_0$) while two are long ($0.76a_0$). The short bonds are shown by full lines

whereas the long bonds are shown by broken lines. On the other hand, if there is a vacancy inside the tetrahedron (Figure 5-7(b)), all the six Bi-Bi inter-atomic distances are long. The volume of the empty tetrahedron is thus larger than that of the full tetrahedron; this is physically very reasonable since the oxygen ion has strong attractive Coulombic interactions with the Bi ions surrounding it. When an oxygen atom and the vacancy are juxtaposed, the two tetrahedrons share a longer Bi-Bi distance between them (Figure 5-7(c)).

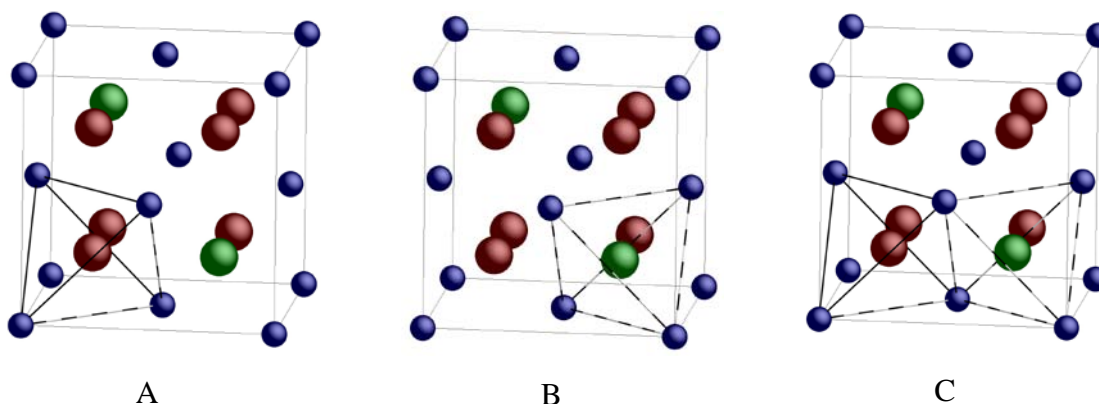


Figure 5-7. Tetrahedron expansion and contraction due to a vacancy and an oxygen atom, respectively. A) Oxygen present inside the tetrahedron. Oxygen-tetrahedron has four short and two long Bi-Bi interatomic distances. B) Vacancy inside the tetrahedron. Vacancy-tetrahedron has all six long Bi-Bi interatomic distances. C) A vacancy tetrahedron juxtaposed with an oxygen tetrahedron share a long Bi-Bi interatomic distance.

5.3 Density Functional Theory (DFT) Calculations of the Structure of Bi_2O_3

In this section DFT is used to provide further corroboration for the structure determined from experiment and from the MD simulations.

5.3.1 DFT Methodology

Vienna *Ab initio* Simulation Package (VASP) is used for these calculations.^{77,78,79}

In particular, the GGA exchange-correlation functional in PW91⁸⁰ form is used. The projector augmented wave method (PAW)⁸¹ was applied to the core electrons (Bi

[Xe]4f¹⁴5d¹⁰), O[He]). A plane wave cutoff of 500eV was used with a k-points grid of 6*6*6 for systems containing 1x1x1 non-cubic unit cells and 3*3*3 k-points grid for 2x2x2 systems. The positions of the atoms were optimized such that the force on each atom had converged to less than 0.0005 eV/Å. Periodic boundary conditions were applied in all the three directions.

5.3.2 Vacancy Ordering

Walsh *et al.*⁷⁶ have recently used DFT to examine defect-ordered structures in δ -Bi₂O₃. As a check on the implementation, these calculations are repeated with vacancies aligned in the <100>, <110> and <111> (see Figure 5-8). These calculations require a simulation cell containing only a unit-cell of two Bi₂O₃ stoichiometric units, i.e., a total of 10 atoms. The geometry optimization was performed using the experimentally obtained lattice parameter of 5.644 Å.⁸²

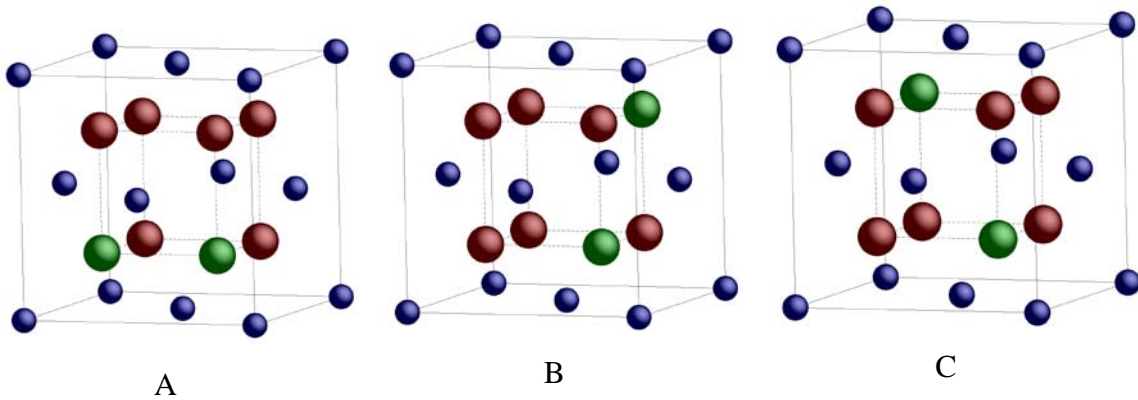


Figure 5-8. Possible vacancy-ordering mechanisms in δ -Bi₂O₃. A) <100> B) <110> and C) <111>.

The lattice parameter, the *a/c* value, cell volume and the relative energies were found to be in quantitative agreement with the previously published results. In particular, in agreement with the Walsh *et al.*,⁷⁶ it is found that <100> and <110> vacancy-ordered structures show a tetragonal distortion whereas the <111> vacancy-ordered structure

maintains cubic symmetry. The relative energy differences are also consistent, predicting $\langle 100 \rangle$ ordered as the most stable structure. However, this result is in disagreement with the earlier analyses both from theory^{68,83} and experiments.^{75,84} This work has extended the DFT work by examining a simulation cell containing 2x2x2 unit cells. Simulations, with $\langle 100 \rangle$, $\langle 110 \rangle$ or $\langle 111 \rangle$ ordering showed the same energy trends as for the 1x1x1 systems.

Table 5-1. Relative stability of the ordered structures in 2x2x2 system.

Ordering	Relative Energy (eV/Bi)
$\langle 100 \rangle$	0.000
$\langle 110 \rangle$	0.066
$\langle 111 \rangle$	0.542
$\langle 110 \rangle \langle 111 \rangle$	-0.225

The energy of the structure predicted by the MD simulations and obtained from the analysis of the experiments, i.e., the network of $\langle 110 \rangle$ and $\langle 111 \rangle$ ordering is also calculated. As Table 5-1 shows, this combined ordering in $\langle 110 \rangle$ and $\langle 111 \rangle$ is significantly lower in energy than any of the three previously considered structures.

5.3.3 Bonding and Charge Distribution

To characterize the bonding in the system, the electron density in the structure is examined. The electron density contour maps for the individually ordered structures in $\langle 100 \rangle$, $\langle 110 \rangle$ and $\langle 111 \rangle$ were found to be consistent with those shown by Walsh *et al.*⁷⁶

It is useful to examine the structure from the perspective of the Bi ion, which is in an octahedral environment with respect to the oxygen-vacancy sub-lattice. Walsh *et al.* found that when the vacancies are in a $\langle 100 \rangle$ or $\langle 110 \rangle$ arrangement, the Bi electron lone-pair charge is directed towards the vacancies. By contrast, when the vacancies are in a $\langle 111 \rangle$ arrangement, no lone pair is formed and the charge is essentially evenly distributed around the Bi ion.

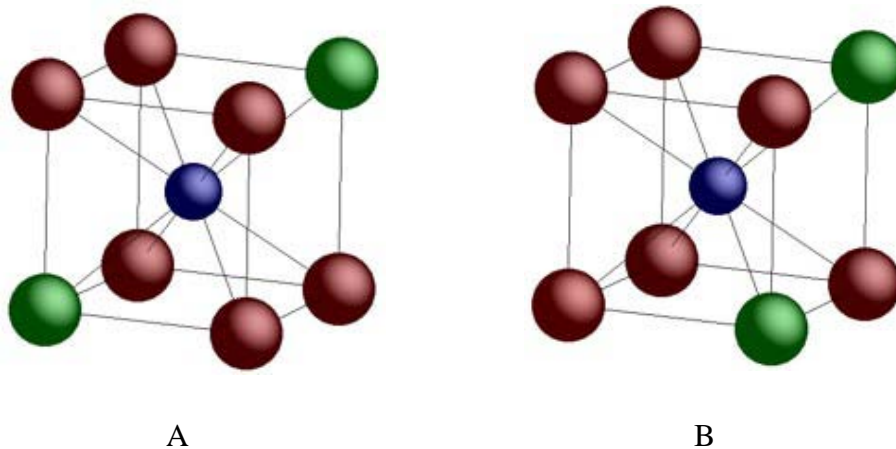


Figure 5-9. Two kinds of Bi-centered oxygen sub-lattice cubes are present in the combined vacancy-ordered structure. A) Bi surrounded by $\langle 110 \rangle$ vacancy ordering. B) Bi surrounded by $\langle 111 \rangle$ vacancy ordering.

The distribution of the electron lone-pair charge in the combined vacancy ordered structure, i.e., $\langle 110 \rangle$ and $\langle 111 \rangle$, maintains an analogous charge distribution to that observed in the individual vacancy ordered structures.

Table 5-2. Bi-O bond length in Bi-centered $\langle 110 \rangle$ and $\langle 111 \rangle$ vacancy-ordered oxygen sub-lattice

	$\langle 110 \rangle$		$\langle 111 \rangle$
Bi – O (Å)	Bi – O5, Bi – O6	2.303	2.426
	Bi – O1, Bi – O2	2.399	
	Bi – O3, Bi – O4	2.559	

However, in the combined vacancy-ordered structure, there are two different environments around the Bi atoms, with some Bi atoms surrounded by $\langle 110 \rangle$ ordered vacancies and some by $\langle 111 \rangle$ ordered vacancies (i.e., in the arrangements shown in Figures 5-9(a) and 5-9 (b)). As a result, there are varying bond lengths (Table 5-2) and different electron lone-pair charge distributions (Figure 5-10). The charge distribution is represented in two (110) planes perpendicular to each other, both passing through the central bismuth ion. All of the Bi-O bonds are of equal length as shown in Table 5-2.

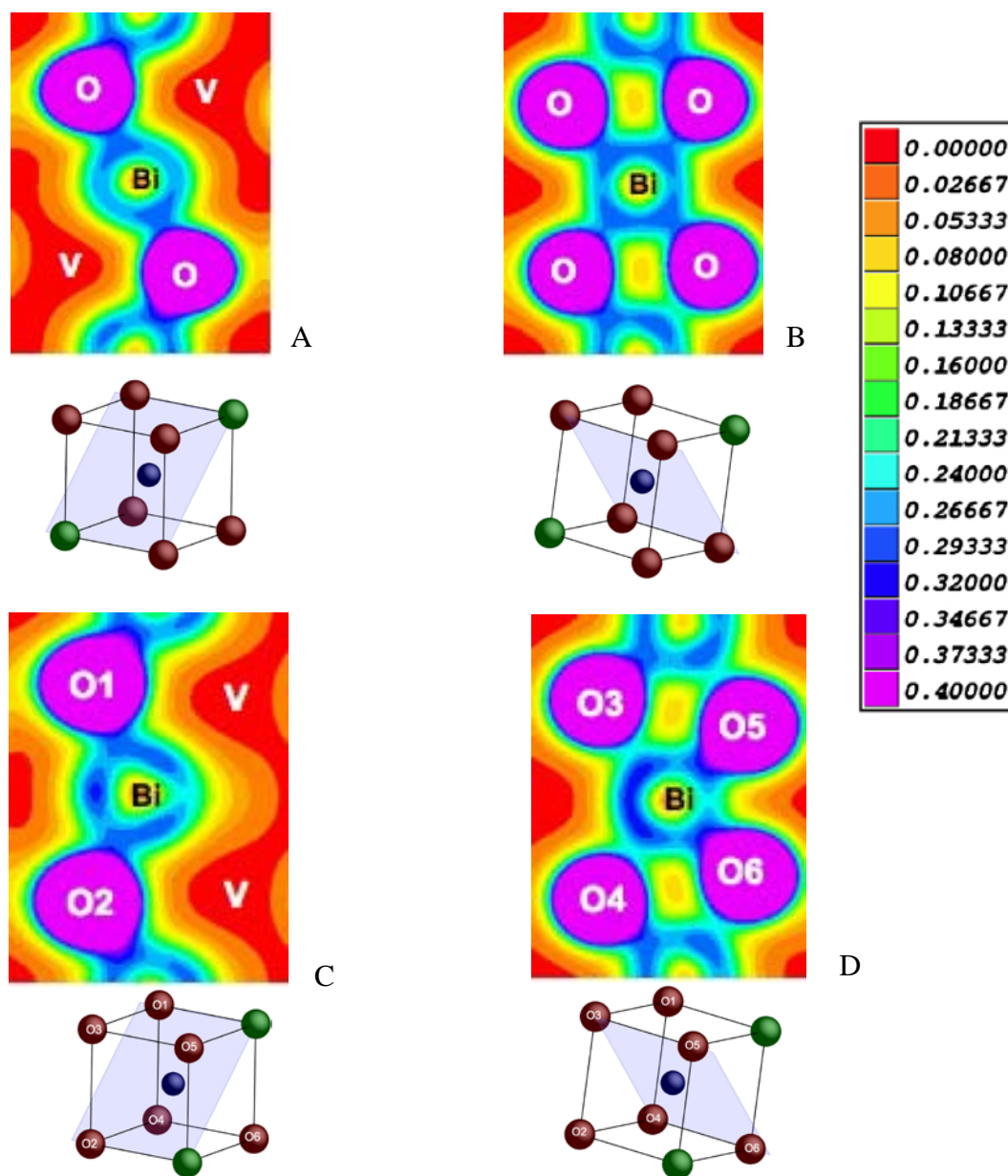


Figure 5-10. Electron lone-pair charge around two different Bi-centered cubes. One of the perpendicular (110) planes in the oxygen sub-lattice is shown for both $\langle 111 \rangle$ and $\langle 110 \rangle$ vacancy-ordered Bi-centered cubes. A) In $\langle 111 \rangle$ vacancy-ordered oxygen sub-lattice, the electron lone-pair charge is equally distributed. B) All four Bi-O bond lengths are same. C) $\langle 110 \rangle$ vacancy-ordered oxygen sub-lattice; electron lone-pair charge is directed toward the vacancies. D) Shorter and longer pairs of bond lengths predicting the distorted oxygen sub-lattice with an evidence of lesser bonding between Bi-O3 and Bi-O4. (Contour levels are between $0.0 e/\text{\AA}^3$ (red) and $0.4 e/\text{\AA}^3$ (pink).

Due to the symmetric ordering of vacancies in $\langle 111 \rangle$ cubic sub-lattice (Figures 5-10(a) and 5-10(b)), the electron lone-pair charge is equally distributed to form the Bi-O

bonds. In contrast, the Bi centered $\langle 110 \rangle$ ordered oxygen sub-lattice has different bond lengths, which occur in pairs. The two perpendicular (110) planes for $\langle 110 \rangle$ ordered sub-lattice are shown in Figure 5-10(c) and 5-10(d). The plane containing the two vacancies here (in Figure 5-10(c)) has a Bi-O bond length that is the same as in the $\langle 111 \rangle$ ordered oxygen sub-lattice.

However, in the perpendicular plane (Figure 5-10(d)), two of the Bi-O bonds are shorter and two are longer thus distorting the Bi centered $\langle 110 \rangle$ oxygen sub-lattice. As expected, there is a directional distribution of the electron lone-pair charge towards the vacancies. In this distorted sub-lattice, there is further an evidence of weaker bonding between the Bi-O5 and Bi-O6.

5.3.4 Electronic Structure of Vacancy-Ordered $\delta\text{-Bi}_2\text{O}_3$

Due to two different vacancy-ordered environments around the Bi ions, there are different Bi-O bond lengths. The ionicity of the ions and the surrounding atomic environment affects the bond length. The charge distributions associated with the Bi and O ions are characterized using Bader charge analysis^{85,86} of the electronic structure determined from DFT (Table 5-3). If Bi_2O_3 were fully ionic, the Bi and O ions would have formal charges of +3e and -2e respectively. Instead, Bader charge analysis shows that the Bi ions inside $\langle 111 \rangle$ ordered vacancies have a DFT atomic charge of +2.1232e while the Bi ions inside $\langle 110 \rangle$ ordered vacancies have a charge of +2.8411e.

Table 5-3. Electronic charge on the ionic species.

Vacancy-ordering environment	Ion	Charge (e)
$\langle 111 \rangle$	Bi	+2.1232
$\langle 110 \rangle$	Bi	+2.8411
	O	-1.77

While Bi ions with charge $+2.84 e$ is very similar to the valence charge of $+3$ and show ionic character, the Bi ions with charge $+2.12 e$ is significantly deviated and hence shows a degree of covalency. The charge on the O ions is $-1.77e$. Numerically, the deviation of the DFT atomic charge from the formal charge gives the amount of charge associated with covalent bonding.

It is useful to characterize the charge distribution from the perspective of the Bi tetrahedra (Figure 5-11(a)). As shown in Figure 5-11(b), each oxygen ion present inside the tetrahedron is bonded to three Bi ions of higher ionic charge $+2.84e$, and one of more “covalent character: charge $+2.12e$.”

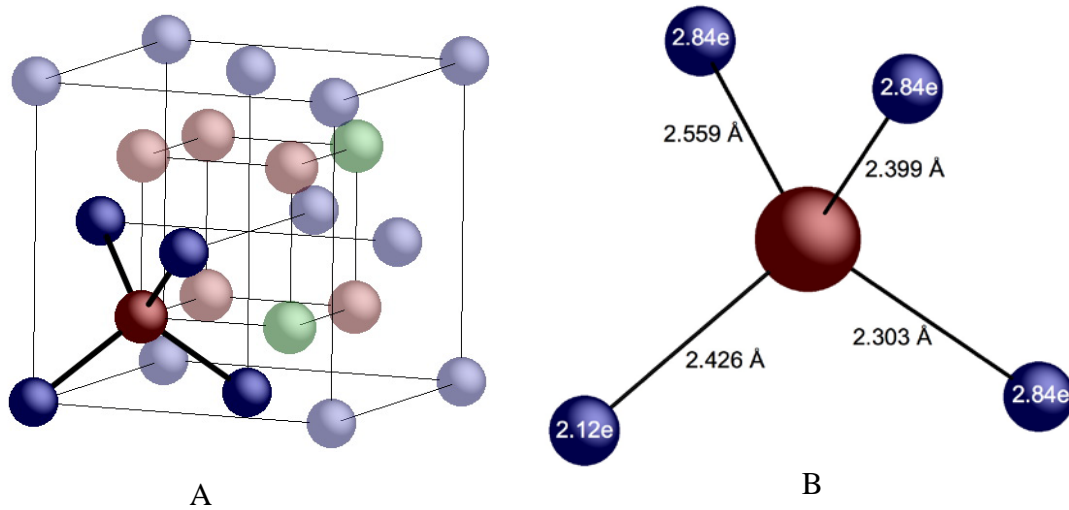


Figure 5-11. A) A tetrahedra in the unit cell. B) Each bismuth tetrahedra is formed by three Bi (surrounded by $\langle 110 \rangle$ ordered vacancies) of charge $2.84e$ and one Bi (surrounded by $\langle 111 \rangle$ ordered vacancies) of charge $2.12 e$. All four Bi-O bonds are of different lengths.

The four different bond lengths observed previously in Table 5-2 are shown here. All four Bi-O bonds inside the tetrahedra have different lengths. The tetrahedral configuration of Bi ions is same even around the vacancies.

5.4 Discussion

According to Larrif and Theobald,⁸⁷ oxygen diffusion in δ -Bi₂O₃ occurs in the direction of the lone pair of electrons. DFT calculations in this thesis predict the existence of a directional lone pair of electrons when Bi has vacancy neighbors in the $\langle 110 \rangle$ direction, and an isotropic electron distributions in Bi has vacancy neighbors in the $\langle 111 \rangle$ direction. It appears that the electronic charge distribution plays a significant role in limiting the diffusion. Since a covalent bond is directional and difficult to break, it is speculated that the covalent Bi–O bond is the limiting factor in the oxygen diffusion in the vacancy ordered system. As such, it is anticipated that variations in the covalent Bi–O bond characteristics might be the key crystallochemical variable chiefly responsible for tailoring the ionic conductivity of bismuth oxide based electrolytes. A corresponding argument may well be applicable to ZrO₂ and CeO₂ based electrolyte materials.

CHAPTER 6 CRYSTALLOGRAPHIC ANALYSIS OF THE STRUCTURE OF CUBIC BISMUTH OXIDE

6.1 Introduction

In the previous chapter, it is found that a $2 \times 2 \times 2$ superstructure is required to completely define the vacancy ordering mechanism (occupational ordering) in $\delta\text{-Bi}_2\text{O}_3$. Due to the ordering, it is observed that there are two different kinds of Bi ions surrounded by different vacancy ordering environments for which the bonding environments from charge-distribution viewpoint is established. In this chapter, the structural distortion that occurs due to the vacancy ordering, i.e., the positional ordering (displacement) of the oxygen ions and the cation displacements (which have until now remained subtle in the wide literature on $\delta\text{-Bi}_2\text{O}_3$) is established. A systematic crystallographic analysis of the vacancy-ordered structure of pure $\delta\text{-Bi}_2\text{O}_3$ is also presented.

This Chapter begins by presenting a schematic of the $2 \times 2 \times 2$ super-structure followed by the space group of $\delta\text{-Bi}_2\text{O}_3$, which due to the vacancy ordering differs from the conventional fluorite space group. This will lead to the discussion on the consequent ionic displacements and structural distortion in the sub-structures.

6.2 Schematic Representation of the Structure of $\delta\text{-Bi}_2\text{O}_3$

As a way to begin describing the $2 \times 2 \times 2$ superstructure which contains 32 Bi atoms and 48 O atoms, the plane views of the structure obtained from DFT simulation are presented along the (100), (010) and (001) in Figure 6-1. All the columns of cations contain cations that are displaced from the column axis. However, there are certain cations, which do not move with respect to the positions of an ideal double fluorite structure. For example, cations #'s 1, 5, 9 and the cations behind them in Figure 6-1(a) do not displace when viewed from either of the planar directions. On the other hand,

some cations such as, #'s 3 and 7 which are not displaced in the (100) plane (Figure 6-1(a)) are in fact displaced along (001), as can be seen from the other perspectives.

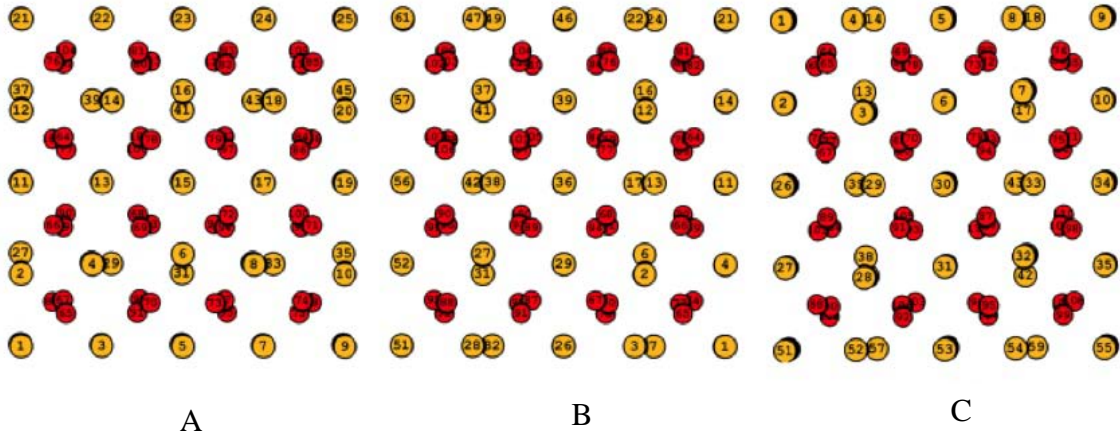


Figure 6-1. The 2x2x2 fluorite-related superstructure viewed from three different planes. A) [100], B) [010] and C) [001]. Bi ions are shown in gold and oxygen ions are shown in red.

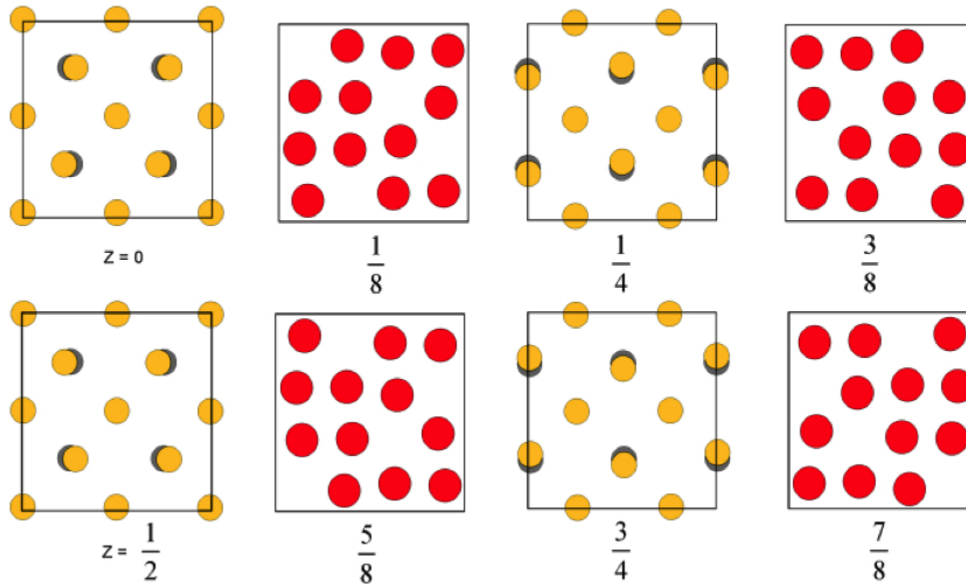


Figure 6-2. Layered sequence of the structure of $\delta\text{-Bi}_2\text{O}_3$ along [001] direction showing the relative displacement of the bismuth ions with respect to the original fluorite positions and the distortion of the oxygen sub-lattice.

Furthermore, it is found that the cations move in pairs in different directions. For instance, when viewed from one of the planes (e.g., Figure 6-1(a)), a (010) displacement

of the cations (atoms # 2 & 27 or 12 & 37) is followed by a displacement in (001) (e.g., atoms # 4 & 29 or 39 & 14).

In Figure 6-2, a layer sequence of the structure along the $\langle 001 \rangle$ direction is presented using the same convention as Galasso⁸⁸ when describing the pyrochlore structure (another fluorite-related $2 \times 2 \times 2$ superstructure). Schematic shows relative displacement of the bismuth ions relative to the exact fluorite positions (shown in grey). The oxygen ions are also displaced from their respective fluorite positions. The layered positioning of the oxygen and vacancies are shown in Figure 6-3. The oxygen displacements are not shown here.

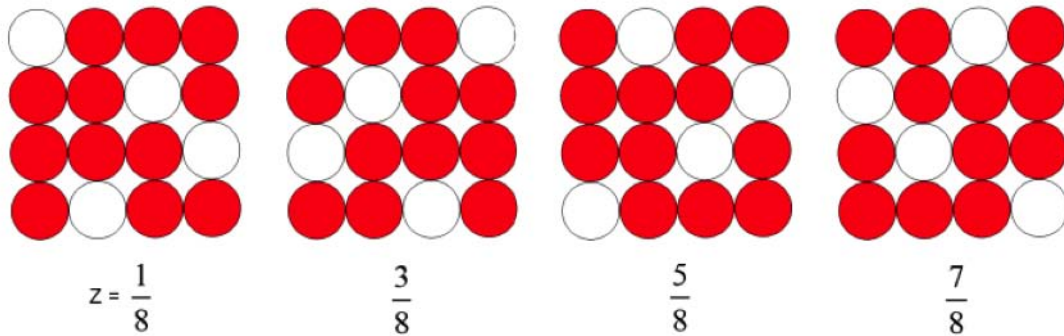


Figure 6-3. Layered sequence of the oxygen sub-lattice along $[001]$ in $2 \times 2 \times 2$ $\delta\text{-Bi}_2\text{O}_3$. The displacements of the ions are not shown. Oxygen ions are shown in red and vacancies are shown in white.

The above schematics, Figures 6-1 and 6-2, show exact positions of the cations and anions in the $2 \times 2 \times 2$ fluorite-related structure of $\delta\text{-Bi}_2\text{O}_3$. Figure 6-3 shows the arrangement of vacancies in different planes. These schematics give an overview of the structure of $\delta\text{-Bi}_2\text{O}_3$. Due to the vacancies' ordering and ionic displacements, the structure differs from the ideal fluorite space group.

6.2.1 Space Group Analysis

In agreement with experiments, the DFT simulations predict a defect-derivative fluorite crystal structure with ordering in the unoccupied anion sites in the $\langle 110 \rangle$ and $\langle 111 \rangle$ directions.

The space group of an ideal fluorite cubic structure is $Fm\bar{3}m$ (225). In $\delta\text{-Bi}_2\text{O}_3$, the overall cubic symmetry is maintained. However, the lattice parameter is very close to twice that of normal fluorite structures: 11.19761 Å as determined from the DFT calculations. The unit cell contains 16 Bi_2O_3 stoichiometric units rather than two as in the fluorite unit cell. The experimentally reported lattice parameter of a unit-cell of $\delta\text{-Bi}_2\text{O}_3$ is 5.644 Å,⁸² which corresponds to 11.288 Å for the $2\times 2\times 2$ superstructure. This DFT error of 0.8% may be taken as representative of the degree of quantitative accuracy that can be expected in the analyses below. The superstructure lowers the symmetry to space group of $Fm\bar{3}$ (202). It is important to recall that $Fm\bar{3}$ is a maximal non-isomorphic t -subgroup of $Fm\bar{3}m$, where all translational symmetry is maintained but the order of the point group is reduced (from 48 to 24).¹⁸ In essence, $Fm\bar{3}$ is derived from the $Fm\bar{3}m$ in that the 4-fold rotation along $\langle 100 \rangle$ is reduced to a 2-fold rotation, and that the 2-fold rotation along $\langle 110 \rangle$ and the associated perpendicular mirror planes are lost. The reduction in the 4-fold rotation to 2-fold rotation is due to the displacement of the Bi ions in $\langle 100 \rangle$. However, this loss in symmetry is neither a consequence of the vacancies nor their ordering. The resulting space group parameters of the $\delta\text{-Bi}_2\text{O}_3$ are presented in Table 6-1. This superstructure contains three crystallographically distinct Bi sites, Bi(1)

at 4a, Bi(2) at 4b and Bi(3) at 48h, and two crystallographically distinct O sites, O(1) and O(2), both at 96i.

Table 6-1. Space group parameters of superstructure of δ -Bi₂O₃ determined from density functional theory under the GGA-PAW approximation.

Space Group Fm $\bar{3}$, 202					
Unit Cell $a_0 = 11.19761 \text{ \AA}$			Volume = 1404.0283 \AA^3		
Atom	Wyckoff Position	x	y	z	Occupancy
Bi (1)	4a	0.0000	0.0000	0.0000	1.00
Bi (2)	4b	0.5000	0.0000	0.0000	1.00
Bi (3)	48h	0.2500	0.2229	0.0000	0.50
O (1)	96i	0.1279	0.0962	0.1460	0.25
O (1)	96i	0.4038	0.1460	0.1279	0.25

Taking the occupancy into account, the superstructure is comprised of 32 cations and 48 anions, i.e., 16 formula-units per unit cell (Z=16). In the case of the cation, there are two different sites each of multiplicity four, Bi(1) and Bi(2), and one site of multiplicity 48, Bi(3). The occupancy of Bi(1) and Bi(2) sites is 1.0 and of Bi(3) is 0.5. There are thus 64 anion sites available in the structure, of which 48 are occupied by oxygen ions equally distributed on the two crystallographically different sites, O(1) and O(2); the remaining 16 sites are unoccupied (vacancies). The crystallographic sites of 1/8 of the superstructure are represented in Figure 6-4. As reference points, the conventional oxygen fluorite positions (8c in ideal fluorite) are shown in black in Figure 6-4; however, these points do not correspond to ion positions in the superstructure. Each of these fluorite oxygen positions is surrounded by three O(1) or O(2) sites, only one of which is occupied at any given time. The oxygen atoms are displaced from the ideal 8c Wyckoff position to 96i. To maintain the stoichiometry, only six oxygen anions are present in each 1x1x1 sub-unit; there are also two vacancies per sub-unit.

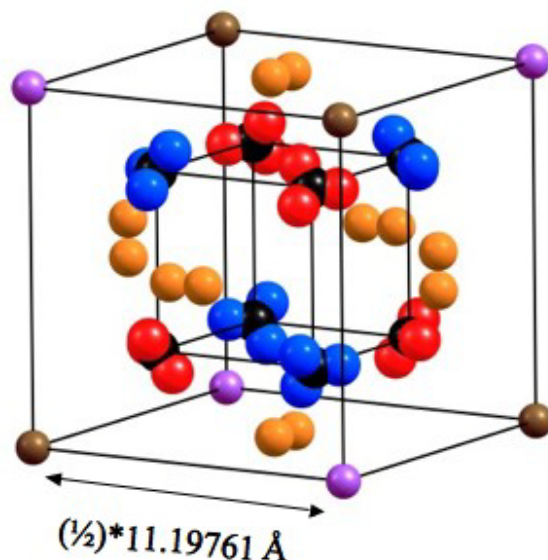


Figure 6-4. Crystallographic sites of the space group $Fm\bar{3}(202)$. 1/8 of the $2 \times 2 \times 2$ superstructure is shown here. Bi(1) and Bi(2) have an occupancy of 1.0. The Bi(3) sites have an occupancy of 0.5 with only one of the two of nearby available Bi(3) sites being filled at any given time. In the oxygen sub-lattice, for every oxygen fluorite position (black) there are three possible oxygen positions, only one of which is filled either by O(1) or O(2). Color scheme: Bi(1) are shown in brown, Bi(2) in violet, Bi(3) in orange, O(1) in red, O(2) in blue and exact (8c) oxygen position in black.

These displacements arise to accommodate the crystallochemical imbalance resulting from the unoccupied sites (vacancies). Further, since the vacancies are ordered, these displacements are also arranged in an ordered manner.

6.2.2 Bond Lengths

Bond lengths are briefly discussed in the previous chapter. In this chapter, they are discussed in detail with the illustration of the implications on the structural distortion. The bond lengths predicted by DFT are presented and then compared with the estimates from the other, more approximate, method. The relationship between the different bond lengths and the vacancy ordering is also presented.

6.2.2.1 Bond lengths from DFT calculations

As discussed in the Introduction, the structure of δ - Bi_2O_3 combines vacancy ordering in $\langle 110 \rangle$ and $\langle 111 \rangle$ directions. To characterize the bonding in the structure, it is useful to first examine the structure from the perspective of the Bi ions. The Bi ions are in an octahedral environment with respect to the oxygen-vacancy cubic sub-lattice, i.e., the Bi ions are at the centers of O ion cubes. In the combined vacancy-ordered structure, the Bi ions sit in two different environments, the Bi(1) and Bi(2) ions have vacancy neighbors in the $\langle 111 \rangle$ directions (Figure 6-5), while the Bi(3) ions have vacancy neighbors in the $\langle 110 \rangle$ directions (Figure 6-6).

6.2.2.2 Cation displacements in the $\langle 111 \rangle$ vacancy ordered oxygen sub-lattices

For the $\langle 111 \rangle$ vacancy ordered oxygen sub-lattice, each Bi(1) and Bi(2) ion is surrounded by six O(1) and O(2) ions respectively (Figure 6-5). As shown in Table 6-2, all the Bi(1)-O(1) and Bi(2)-O(2) bond lengths are identical.

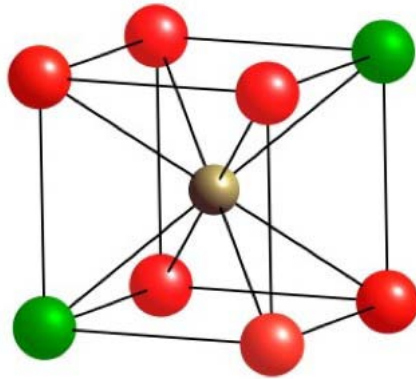


Figure 6-5. $\langle 111 \rangle$ vacancy ordered oxygen sub-lattice. Bi(1) present inside the O(1) sub-lattice. All Bi-O bond lengths are 2.426 Å, all O-O distances are 3.138 Å and all O-O-O angles are 72.276° . Similarly, Bi(2) is present inside O(2) oxygen sub-lattice and the sub-lattice has the same geometry.

Moreover, as discussed previously, this uniformity in bond lengths is reflected in the electronic degrees of freedom, with the charges between Bi(1)-O(1) and Bi(2)-O(2)

being equally distributed.⁸⁹ This equivalence in the positions of the oxygen ions ensures that the Bi(1) and Bi(2) ions do not move from their crystallographic sites at the center of the cube. These are those non-displaced Bi ions previously discussed in Figure 6-1.

Furthermore, all nearest neighbor O-O separations are 3.138 Å. However, the equal Bi-O bond lengths do not ensure a perfect-cubic (angles = 90°) oxygen sub-lattice. Rather, all the O-O-O angles in the sub-lattice are 72.276°, a very significant deviation from cubic.

6.2.2.3 Cation displacements in the <110> vacancy ordered oxygen sub-lattice

The oxygen ions in the <110> vacancy ordered sub-lattice are not all in crystallographically equivalent positions. In this sub-lattice, of the six oxygen ions surrounding each Bi(3), three are in O(1) sites and three in O(2) sites. As a result, the <110> oxygen sub-lattice is heavily distorted and has three different Bi-O bond lengths (see Table 6-2). One of the twelve possible <110> vacancy ordered oxygen sub-lattices is shown in Figure 6-6(a). In this sub-lattice, there are three O(1) ions, marked as O(1) 1, O(1) 3 and O(1) 6 and three O(2) ions, marked as O(2) 2, O(2) 4 and O(2) 5. There are three different Bi-O bond lengths that occur in pairs; each pair contains two crystallographically different oxygen ions. In Figure 6-6(a), the Bi(3)-O(1) 6 and Bi(3)-O(2) 5 bond lengths are 2.303 Å. Similarly, the Bi(3)-O(1) 1 and Bi(3)-O(2) 2 bond lengths are 2.399 Å, while the Bi(3)-O(1) 3 and Bi(3)-O(2) 4 bond lengths are 2.559 Å. A consequence of the non-equivalence of the oxygen ions and <110> vacancy ordering is that the central Bi(3) ion is displaced from its ideal positions (shown by dotted arrow in Figure 6-6(a)) by 0.3036 Å in one of the <100> directions away from the face of the distorted cube containing the vacancies. In contrast to the simpler geometry of the <111>

oxygen sub-lattice, the $\langle 110 \rangle$ sub-lattice is heavily distorted with these differing bond lengths also resulting in dissimilar O-O-O angles (Figure 6-6(b)).

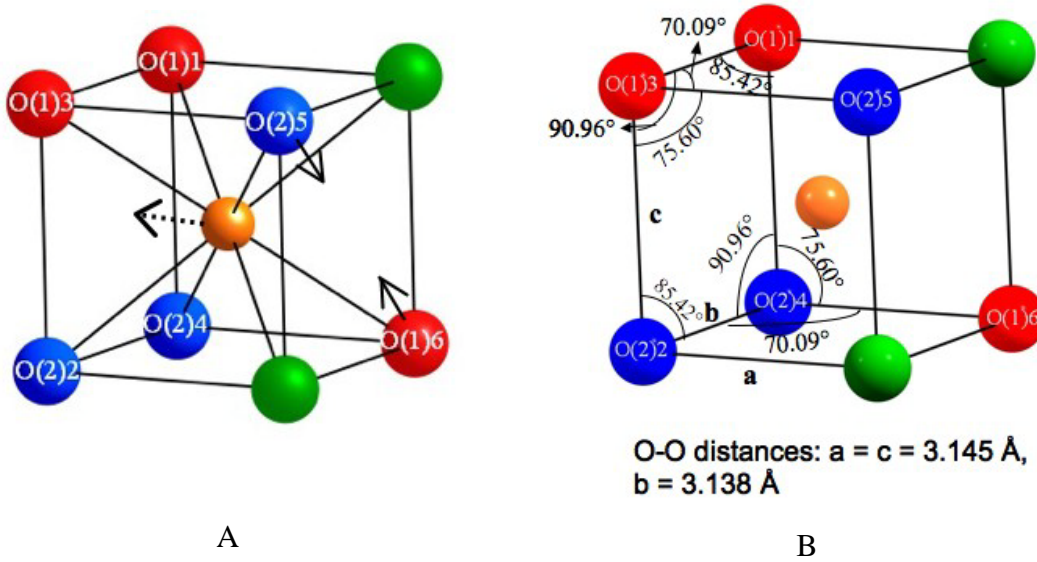


Figure 6-6. $\langle 110 \rangle$ vacancy-ordered oxygen sub-lattice. A) Bi(3) present inside the oxygen sub-lattice formed by three O(1), three O(2) and two vacancies. There are three different pairs of Bi-O bond lengths: Bi(3)-O(1)6 and Bi(3)-O(2)5 = 2.303 Å, Bi(3)-O(1)1 and Bi(3)-O(2)2 = 2.399 Å, Bi(3)-O(1)3 and Bi(3)-O(2)4 = 2.559 Å. The dotted arrow shows Bi(3) displacement in $\langle 100 \rangle$ direction by 0.3036 Å away from the plane containing the vacancies and solid arrows on O(2)5 and O(1)6 show the oxygen displacement in a direction close to $\langle 110 \rangle$. B) Schematic showing the geometrical values of the distorted $\langle 110 \rangle$ oxygen sub-lattice. Only O-O distances and O-O-O angles are shown; those involving a vacancy are not shown.

6.2.2.4 Anion displacement

The DFT calculations show a preferential-directional displacement of all of the oxygen ions. The structural analysis shows that every oxygen ion displaces in the direction of the two first nearest vacancies ordered in $\langle 110 \rangle$, as shown by the solid arrows in Figure 6-6(a). These two vacancies provide considerable open space in the structure, into which the ions can relax. The result is that both oxygen ions displace from the fluorite site by a magnitude of $x = 0.235$, $y = 0.322$ and $z = 0.033 \text{ \AA}$, resulting in a total displacement of 0.4 Å in a direction close to, but not exactly parallel to, $\langle 110 \rangle$.

6.2.2.5 Bond lengths from Shannon radii

There are several standard ways to estimate the bond lengths in ionic materials, including analysis of the Shannon radii.⁶⁹ In this sub-section section the value of Shannon radii method for analyzing Bi_2O_3 is assessed.

The bond lengths calculated from the radii given by Shannon⁶⁹ are based on the coordination environment. In ideal structures without defects, the bond lengths predicted by Shannon radii are quite accurate.⁶⁹ However, in the presence of defects or vacant lattice sites, as in the $\delta\text{-Bi}_2\text{O}_3$ structure, the bond lengths can either deviate from the expected values or sometimes can provide only incomplete information, as is found to be the case in the following analysis.

Every cation in an ideal fluorite structure is coordinated with eight anions. However in $\delta\text{-Bi}_2\text{O}_3$, each Bi^{3+} ion is coordinated with only six oxygen ions, the other two anion sites being vacant. According to the Shannon radii,⁶⁹ $r_{\text{Bi}^{3+}}(\text{VI}) = 1.03 \text{ \AA}$, $r_{\text{Bi}^{3+}}(\text{VIII}) = 1.17 \text{ \AA}$ and $r_{\text{O}^{2-}}(\text{IV}) = 1.38 \text{ \AA}$. This yields estimates of the Bi(VI)-O of 2.41 \AA . This estimated bond length is actually very close to the Bi-O bond length of 2.424 \AA in the non-distorted $\langle 111 \rangle$ ordered oxygen sub-lattice. Interestingly, although six coordinated, the DFT calculations yield Bi-O bond lengths in the $\langle 110 \rangle$ sub lattice as 2.559 \AA , which is very close to the Bi(VIII)-O bond length of 2.55 \AA . Hence, in this case the Shannon radii predictions are in close agreement with some Bi-O bond lengths given by DFT, but not others.

6.2.2.6 Sub-unit Cell Distortion

Thus far, it is characterized that ionic displacements of both Bi and O ions from their ideal fluorite positions are induced by the vacancies in $\delta\text{-Bi}_2\text{O}_3$. As a consequence,

the structure is distorted locally. In this section, these local distortions from the perspective of the FCC network of Bi ions are characterized.

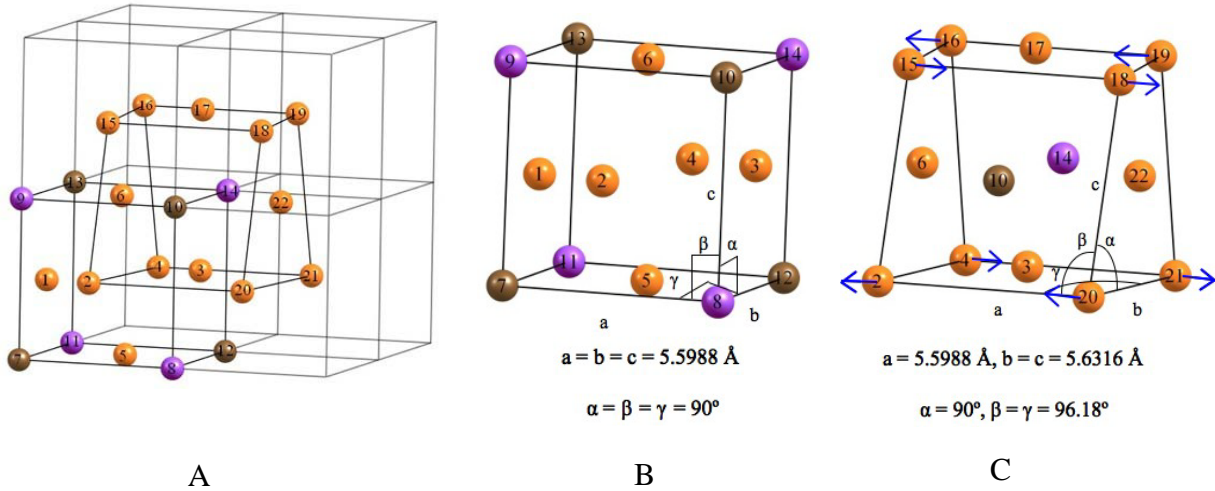


Figure 6-7. Distortion in the superstructure. A) Two interpenetrating FCC networks in $2 \times 2 \times 2$ superstructure. B) A non-distorted cubic FCC network formed by four Bi(1), four Bi(2) and six Bi(3) cations. C) A distorted FCC network formed by twelve Bi(3); the other two cations can be either both of same Wyckoff number or different (Bi(1), Bi(2)). The corners of the non-distorted FCC network are formed by Bi(1) and Bi(2) whereas those of distorted FCC network are formed by Bi(3) cations. For clarity, oxygen ions are not shown. Color scheme - Bi(1) in brown, Bi(2) in violet and Bi(3) in orange.

As Figure 6-7(a) shows, the Bi network can be considered either as an FCC network with Bi(1) and Bi(2) ions in the eight corners and Bi(3) ions of the six phases, or as a network with Bi(3) ions at the eight corners and on four of the six faces, the remaining two faces being occupied by a Bi(1) and a Bi(2) ion. These two distinct, interpenetrating FCC networks are shown in Figure 6-7(a). The difference between the two networks can be characterized by the shape of the boxes defined by the corner Bi ions.

Table 6-2. Bi-O bond lengths in the $\langle 110 \rangle$ and $\langle 111 \rangle$ vacancy ordered sub-lattice. The two $\langle 111 \rangle$ vacancy ordered sub-lattices has Bi(1) and Bi(2) ions surrounded by six O(1) and six O(2) ions respectively. The $\langle 110 \rangle$ vacancy ordered sub-lattice has three O(1) and three O(2) ions surrounding each Bi(3) ion.

	$\langle 111 \rangle$	(Å)
Bi(1) – O	O(1)	2.426
Bi(2) – O	O(2)	2.426
	$\langle 110 \rangle$	
Bi(3) - O	O(1) 5, O(2) 6	2.303
	O(1) 1, O(2) 2	2.399
	O(1) 3, O(2) 4	2.599

Recalling that the Bi(1) and Bi(2) ions sit at the ideal fluorite sites, the box defined by these ions, Figure 6-7(b), is a perfect cube with the Bi-Bi second nearest neighbor distance being half the lattice parameter, 5.5988 Å. By contrast, the FCC network defined by the Bi(3) ions in the corners, which are displaced by 0.3036 Å along $\langle 100 \rangle$ as shown in Figure 6-7(c) is distorted. In Figure 6-7(c), the Bi-Bi distance between ions 2 and 20 and between ions 4 and 21 is not affected by the displacement and remains 5.5988 Å, as is in the undistorted Bi(1)-Bi(2) FCC sublattice. However, the anti-parallel displacement of the columns of ions has the consequence that the distance between ions 2 and 4, and between ions 20 and 21 ions increases to 5.6316 Å. (Similar anti-parallel displacements occur between ions 2 and 15 and between ions 20 and 18.) These displacements distort the box such that while α remains 90° β and γ deviate significantly, taking the value of 96.18° . Each $2 \times 2 \times 2$ superstructure contains an equal number of these distorted FCC networks oriented along crystallographic axis. Thus, despite these distortions, due to the anti-parallel displacements in all three crystallographic axis, the overall system is cubic.

In the distorted FCC network, 12 of the 14 cations are Bi(3) ions with the remaining two being either Bi(1) or Bi(2). Depending on the choice of the Bi(3) FCC network, both of the non-displaced ions could be at their Wyckoff positions or one could

be in a Bi(1) site and the other in Bi(2) site. In the non-distorted FCC network (Figure 6-7 (b)), 8 out of the 14 Bi FCC ions are non-displaced, i.e., four each from Bi(1) and Bi(2); the remaining six are Bi(3).

Battle *et al.*⁹⁰ also postulated a similar kind of FCC network to the non-distorted network that has been presented here. In the Y_2O_3 - Bi_2O_3 system, they expected Bi^{3+} to occupy all Bi(3) positions (as also seen here), whereas, the rest of the positions at the corners of the unit cell (see Figure 6-7(a)) could be occupied either of Y^{3+} and Bi^{3+} . In their analysis, they did not, however, distinguish between the non-distorted and the distorted networks.

6.2.2.7 Comparison with Bixbyite Structure

The bixbyite structure displays $Ia\bar{3}$ space group symmetry with a cell formula $M_{32}O_{48}$ consisting of 32 cations, 48 anions and 16 vacant anion sites. The cations occupy 8a and 24d sites at 0, 0, 0 and $x, 0, 0.25$ respectively and the anions occupy 48e sites at x, y, z . It is interesting to notice that while the vacancy-ordered structure of δ - Bi_2O_3 very closely resembles that of the bixbyite structure, it is actually distinct.

On the one hand, the vacancies and the cations have similar crystallographic positions and the vacancies have same site occupancy in both the structures, thus, resulting in the same ordering of vacancies. Using coordination defect theory, Bevan and Martin⁹¹ have recently shown 3D vacancy networks in $\langle 110 \rangle$ directions in bixbyite Mn_2O_3 . These vacancy networks are connected by $\langle 111 \rangle$ vacancy linkages. This is identical to the $\langle 110 \rangle$ - $\langle 111 \rangle$ vacancy in Bi_2O_3 .^{75,89} The cations show similar crystallographic characteristics in both the structures. In particular, in each structure there

are 8 non-displaced and 24 displaced cations. Further, the vacancy environment around two different cations remains the same (Figures 6-5 and 6-6).

On the other hand, the anion positions in the two structures are different, arising from different displacements relative to the cation positions. To elucidate these differences, a DFT simulation starting with Bi_2O_3 arranged in the bixbyite structure is performed. During the relaxation, the O ions move considerably; the final structure is that originally obtained structure for $\delta\text{-Bi}_2\text{O}_3$ with space group symmetry $\text{Fm}\bar{3}$. It is quite possible that the differences in the anion sublattice, responsible for the difference between the two structures, arises from the lone pair electrons of Bi, that are absent in other cations crystallizing in bixbyite structures.

6.3 Relation to Experiment

The issue of the overall nature of the defect ordering is addressed first. MD simulations show that the high polarizability of Bi ions leads to continuous diffusion in the system. As a result the combined $\langle 110 \rangle$ - $\langle 111 \rangle$ -ordered defect structure does not become locked in. The simulations further show that the presence of non-polarizable or weakly polarizable cations does result in the ordered defect structure being produced, and that it has a structure that is consistent with that found in the experimental analysis of doped Bi_2O_3 by Wachsman *et al.*⁷⁵ It is this structure that is analyzed here and it can be considered as the prototype for the structure present in the doped system. It is thus appropriate to place the crystallographic analysis in the context of the experimental results for doped systems.

Anion Displacement: Positional Ordering from DFT

Anion displacement and vacancy ordering in δ - Bi_2O_3 has long been a subject of discussion, with several contradictory models being presented.^{68,74,90,92} A detailed discussion of these models can be found in Boyapati *et al.*⁷³ Here the issue of doped Bi_2O_3 is addressed, i.e., the anion displacement within the defect ordered structure. Based on neutron-diffraction data, Willis *et al.*⁷⁴ presented an oxygen sub-lattice model (anion cubic sub-lattice) in which all the anions were suggested to be displaced in $\langle 111 \rangle$ directions, i.e., a displacement from regular tetrahedral site, 8c ($\frac{1}{4}, \frac{1}{4}, \frac{1}{4}$), to an interstitial site, 32f (0.3, 0.3, 0.3). Battle *et al.*⁸⁴ suggested a similar displacement in pure Bi_2O_3 . In Y_2O_3 - Bi_2O_3 ⁹² however, they found that a higher concentration of yttria decreased the concentration of $\langle 111 \rangle$ displaced anions, with some evidence of $\langle 110 \rangle$ anion displacement. By contrast, the experiments by Boyapati *et al.* have, however, found that in the displacement occurs in $\langle 111 \rangle$ directions; they did not observe any signature of $\langle 110 \rangle$ displacement. An increased concentration of less polarizable dopants (Y^{3+} compared to Dy^{3+}) increases the number of $\langle 111 \rangle$ displaced anions. As Boyapati *et al.*⁷³ point out, the difference between their results and those of Battle *et al.* may be due to the fact that their samples were not aged while those of Battle *et al.* were aged. DFT calculations also reveal anion displacement that are close to but not exactly along $\langle 110 \rangle$, and the observations in this thesis are thus to a large extent consistent with the results of Battle *et al.*^{90,92}

The actual defect structure of δ - Bi_2O_3 , which is only stable at high temperature, has not been fully characterized. While it is possible that this structure, evolving through diffusion, is not related to the ordered structure inherent to the doped systems, it also seems reasonable that at any single instant in time for any small region of the crystal, the

structure would strongly resemble one the crystallographically equivalent variants of the defect-ordered structure. Further structural characterization and simulation are required to resolve this issue.

6.4 Discussion

MD simulations and DFT calculations are consistent with experiments in that δ - Bi_2O_3 has a $2 \times 2 \times 2$ fluorite-related superstructure with a combined vacancy ordering in $\langle 110 \rangle$ and $\langle 111 \rangle$ directions. It is shown that vacancies lead to significant structural changes, particularly, the ionic displacements. Battle *et al.*⁸⁴ reported the comparison between the displacement of the cations in pure δ - Bi_2O_3 and Y_2O_3 doped δ - Bi_2O_3 . In the pure δ - Bi_2O_3 the cations were found to be present at the exact crystallographic positions.⁸⁴ By contrast, in the doped δ - Bi_2O_3 cations were displaced in $\langle x00 \rangle$ directions. Similar cation displacements in $\langle x00 \rangle$ directions are also found here.

Further analysis shows that the displacement of the cations is correlated with the ordering of the vacancies around them. All cations, which are displaced have an ordering of the vacancies in $\langle 110 \rangle$ around them. By contrast, all non-displaced cations have vacancies ordered in $\langle 111 \rangle$ directions. All the cations that displace in either of the directions, i.e., $[100]$, $[010]$ or $[001]$ move by 0.3036 \AA from their crystallographic positions.

Given the partial occupancies of some anion and cation sites, and the vacancy ordering previously described, Table 6-1 fully describes the atomic and vacancy arrangement. The previous analysis^{72,73} of neutron diffraction data within the fluorite space group considered three possible positions for the oxygen ions 8c, 32f and 48i sites within the fluorite space group. The refinement identified the 32f sites as being most

consistent with the data. The analysis of the positions derived from the simulation is based on the $2 \times 2 \times 2$ fluorite superstructure and identifies the oxygen ion positions as occupying the 96i sites. The results of these experiments showed that not only was there “occupancy ordering” where vacancies aligned along $\langle 111 \rangle$ and $\langle 110 \rangle$, but that there was also “positional ordering” where the oxygen ions were displaced in $\langle 111 \rangle$ from the normal tetrahedral 8c site to interstitial 32f sites.^{72,73} In the current simulation study the oxygen sites are indexed with respect to the $2 \times 2 \times 2$ $Fm\bar{3}$ space group, which has a larger number of equivalent sites. Thus, the $Fm\bar{3}m$ 32f site is analogous to the 96i in the $Fm\bar{3}$ structure. The physical displacement from the 8c sites to the 32f sites in the $Fm\bar{3}m$ space group implies an equal possibility of displacements along the faces of the coordination tetrahedron or the $\langle 111 \rangle$ directions. However, in the $Fm\bar{3}$ space group, due to the doubling of the unit cell to $2 \times 2 \times 2$, displacements from the ideal tetrahedral position (which is 32f in this space group rather than 8c) to the 96i sites represent in-plane displacements within the $\{111\}$ planes, i.e., the oxygen ions are displaced towards the edges of the coordination tetrahedron. Due to lower symmetry of the superstructure, for a given oxygen ion, displacement is not possible towards all six edges of the tetrahedron but only towards three of them.⁹³ As such, by taking into consideration the doubling of the unit cell, the superstructure presented here represents and captures the correlated anion and cation displacements in even more detail.

6.5 Conclusion and Outlook

In Chapters 4,5 and 6 a detailed characterization of the structure of δ - Bi_2O_3 from molecular-dynamics and electronic level simulations is presented that enabled a complete crystallographic analysis. MD simulations have shown that atomic polarizability is very

important in the oxygen diffusion. Low polarizability leads to a combined ordering of the vacancies in $\langle 110 \rangle$ and $\langle 111 \rangle$ directions; high polarizability leads to a disordered lattice and sustained diffusion. The equilibrated vacancy ordered structure determined from MD simulations is consistent with the order of energies determined from DFT calculations. Crystallographic analysis shows that a $2 \times 2 \times 2$ superstructure is required to fully describe the vacancy ordered structure of $\delta\text{-Bi}_2\text{O}_3$, the crystallographic parameters of which are given.

From the electronic structure viewpoint, it is shown that the charge distribution plays a very important role. Due to two different kinds of vacancy environments around Bi atoms, the Bi atoms bond differently with O atoms. It is found that Bi forms covalent-character bond when vacancies are symmetrically ordered in $\langle 111 \rangle$ direction. In contrast it maintains high ionic character bond when vacancies are ordered in $\langle 110 \rangle$ direction. It is speculated that because covalent bond is directional and difficult to break, it is the limiting factor in oxygen diffusion. The cessation of the oxygen diffusion is a consequence of the bond formation.

Finally, although this work has laid the foundations in understanding the structure of pure $\delta\text{-Bi}_2\text{O}_3$, it is important to understand the mechanisms of diffusion and the difference in the doped systems like YSZ and doped CeO_2 to fully characterize the fluorite-based materials.

CHAPTER 7 RADIATION DAMAGE IN MGO

7.1 Nuclear Energy

7.1.1 Nuclear Power

A large amount of energy can be released by the disintegration of an atom. In the year 1911, Ernest Rutherford, brought this to attention from the decay of radium and stated:⁹⁴

“This evolution of heat is enormous, compared with that emitted in any known chemical reaction... The atoms of matter must consequently be regarded as containing enormous stores of energy which are only released by the disintegration of the atom.”

In the last hundred years, science has come a long way by developing a good understanding of the nuclear fission reactions. It is recognized that a wise use of nuclear energy has immense potential to be a part of the solution to the energy crisis; the most significant nuclear energy contribution being in producing electricity. Currently there are 443 nuclear power plants operating throughout the world that account for 15% of the global electric power generation. With nuclear reactors becoming safer⁹⁵ and with increasing technological understanding, this sustainable energy-production source can be relied upon more. Moreover, with a degrading environment and depleting fossil fuel resources, the world is hard-pressed to advance in this technology.

7.1.2 Challenges for Materials Science

While the understanding on nuclear reactions has been put to applications in nuclear reactors for the last 50 years, we still face enormous challenges from a materials science viewpoint. Two most fundamental challenges are, (a) improving radiation tolerance of fissionable materials to improve fuel life inside the reactor, (b) safer disposal

or recycling of the nuclear waste. The first problem is relatively less worrisome than second, for which, we still have no scientific long-term solution.

The nuclear waste consists of radioactive materials that emit different kinds of harmful radiations. Materials such as ^{233}U and ^{239}Pu have long half-life period of 160,000 and 24,100 years.⁹⁶ In addition, minor actinides radioactive such as ^{237}Np , ^{241}Am + ^{243}Am and ^{244}Cm are produced in the nuclear fission reaction and a pose direct threat to environment, not only by radiation but also by mixing with the underground water. Consequently, in pursuit of preventing the environment degradation from carbon-based fuels, all of a sudden one has to worry about the pollution due to their alternatives.⁹⁷

Two strategies are broadly envisioned for dealing with nuclear waste: recycling of spent nuclear fuel and direct disposal into a repository. The first strategy involves reprocessing of the nuclear fuels to reclaim U and Pu for the fabrication of mixed oxide fuel (MOX). The actinides can be incorporated into an inert matrix fuel (IMF). After a once-through burn-up, the MOX and IMF would be sent to a geological repository. The second strategy involves direct disposal of the spent fuel in a geological repository. The U, Pu and actinides would be stored in materials such as zircon⁹⁸ and fluorite-based materials⁹⁹ that are resistant to damage due to radiation emitted by these radioactive materials. These can then be deposited in the geological repositories. Both these strategies are still under research and much needs to be understood, particularly from the radioactivity viewpoint, before they can be widely applicable.

7.2 Radioactivity

From Coulomb's Law, the positively charged protons in the nucleus should repel each other and the nucleus should rapidly fall apart. However, at distances smaller than 10^{-15} m, the protons and neutrons are bound together by a powerful attractive force called

the strong nuclear force, which keeps the nucleus together.¹⁰⁰ This force is independent of the charge on the species. As the number of protons increases inside the nucleus, to maintain its stability, the number of neutrons also increases. For low atomic number elements, the number of neutrons is approximately equal to the number of protons. However, for higher atomic number elements even more neutrons are required to stabilize the nucleus (e.g., $^{59}_{27}\text{Co}$, $^{60}_{28}\text{Ni}$). However, eventually for elements with very high atomic number, even the increased number of neutrons is no longer able to provide such stability. Hence, to gain stability, the nucleus can disintegrate by radiation. This process of disintegration is known as radioactive decay. $^{235}_{92}\text{U}$, $^{239}_{94}\text{Pu}$ are common elements that disintegrate through radioactivity. There are four kinds of radiation decay by which a nucleus can disintegrate: alpha (α) decay, beta (β) decay, gamma (γ) decay and neutron decay.

7.2.1 Alpha (α) Decay

When a nucleus disintegrates by emitting an alpha particle (^4_2He), the process is known as alpha decay. Equation 7-1 describes the alpha decay of $^{239}_{94}\text{Pu}$.



In the α -decay, the parent nucleus ($^{239}_{94}\text{Pu}$) is different from the daughter nucleus ($^{235}_{92}\text{U}$). Hence, one chemical element is converted into another. The binding energy liberated due to the reaction is converted into kinetic energy of the alpha particle and the daughter nucleus. Alpha particles usually have kinetic energy of ~5 MeV and mean free path length of ~32 μm . Because of their small path length, they can be stopped by a sheet of paper and hence are not harmful to human tissue, unless inhaled.

7.2.2 Beta (β) Decay

Beta decay occurs if a nucleus is unstable due to too many protons or neutrons.¹⁰⁰

The excess neutrons or protons transform into other nucleon, changing the neutron to proton ratio and stabilizing the nucleus. There are three types of beta decays such as beta-minus decay, beta-plus decay and electron capture.

In the beta-minus decay, a neutron transforms into proton, and emits an electron called as beta minus particle (β^-) and an electron-antineutrino ($\bar{\nu}_e$). A beta-minus decay can be represented as:



In the beta-plus decay, a proton changes into neutron by emitting a positron (β^+) and an electron-neutrino (ν_e). The positron is similar to electron but has an opposite charge to electron. The reaction can be given as:



The third type of beta decay is electron capture. In this decay, a proton captures an orbiting electron and transforms into a neutron while emitting a neutrino. The electron capture decay can be represented as:



In all types of beta decay, the parent nucleus has a different atomic number than the daughter nucleus. Equation 7-5 gives a common process of all three types of beta decay occurring in ${}^{126}_{52}\text{Te}$ and ${}^{126}_{55}\text{Cs}$. Both these elements are short-lived radioactive nuclides.



7.2.3 Gamma (γ) Decay

In γ -decay, a nucleus changes from a higher energy state to a lower energy state releasing energy in the form of packets of electromagnetic radiation known as gamma rays. These rays are the most intense and penetrative among all. In gamma decay, the number of protons and neutrons remain same.

7.2.4 Neutron Capture

In this radioactive process, a nucleus captures a neutron and forms an excited nucleus.¹⁰¹ The excited nucleus then emits gamma rays and returns to the normal state. A neutron capture reaction can be represented by equation 7-6.



A target nucleus, ${}^{238}_{92}\text{U}$, captures a neutron and forms ${}^{238}_{92}\text{U}^*$, which is an excited state of ${}^{238}_{92}\text{U}$. It is an important process in the production of ${}^{239}_{94}\text{Pu}$ in reactors.

7.3 Nuclear Fission

In a nuclear fission reaction, a nucleus divides into two fragments (of smaller nuclei) and three neutrons. A typical fission reaction of ${}^{235}\text{U}$ can be given as:



For every neutron involved in the nuclear reaction, three new neutrons are produced that further cause fission reactions, in process, setting up a chain reaction. Hence, nuclear fission reactions can be self-sustaining reactions. The fission products have very high kinetic energy; their slowing down is the main mechanism of heat production in the reactor. The energy obtained from a nuclear reaction can be roughly estimated by using the equation $E=mc^2$. For equation 7-7, the energy produced can be estimated as:

$$E = [m(^{235}\text{U}) - m(^{144}\text{Ba}) - m(^{89}\text{Kr}) - 2m_n]c^2 = 173\text{MeV} \quad (7-8)$$

Considering other reactions such as kinetic energy of beta rays, energy of gamma rays, energy of neutrinos and the energy associated with the delayed neutrons, the total energy of a fission reaction of ^{235}U is approximately 195 MeV per fission event.¹⁰¹ This energy is much higher than energy from normal chemical reaction which involve energy transfer of ~5-10 eV.

7.4 Radiation Damage

In a nuclear reactor, with all of the above mentioned processes occurring simultaneously, during the fuel's lifetime, large amount of fission products (10%) are accumulated and the fuel undergoes 2000 – 3000 displacements-per-atom (dpa),¹⁰² thus causing gross changes in the microstructure of the nuclear materials such as formation of voids and cracks. In addition, the crystalline nature of the materials is also damaged due to the creation of vacancies and interstitials, collectively known as Frenkel Pairs (FPs), thus limiting the lifetime of the fuel. Similar processes also occur in nuclear waste. The by-products (or nuclear waste) undergo radiation through β -decay of fission products (^{137}Cs and ^{90}Sr) and α -decay of actinides (U, Np, Pu, Am and Cm). While β -particles produce very low energy recoil nuclei and γ -rays, α -decay produces high-energy α particles (4.5 to 5.5 MeV) and energetic recoil nuclei (70 to 100 keV) along with γ -rays. Due to their high energy, α -particles undergo elastic collisions and the cascade effect displaces several thousand atoms, thereby creating FPs. Furthermore, due to the longer half-lives of actinides, α -decay is generally dominant at longer times.¹⁰³ Understanding the physical and chemical processes due to the consequence of radiation damage, both inside the nuclear reactor and in the repository conditions, is necessary to improve the

performance of the fuel in the reactor and to produce long-lasting storage materials that can sequester radioactive materials/rays from the environment for thousands of years.

The radiation damage phenomena take place at very small time scales ($< 10^{-12}$ s), which makes it difficult to understand them from experiments. Molecular dynamics (MD) simulation is an easy and informative method of calculating the atomistic damage, both chemical and physical. In this thesis, MD has been extensively used to elucidate the atomistic phenomenon occurring due to radiation damage.

7.4.1 Standard Radiation Damage Methodology Using MD Simulation

Atomic-level simulation has long provided important insights into the fundamental processes associated with radiation damage.^{104,105,106,107,108} In particular, simulations have shown themselves to be capable of capturing two important phases of radiation damage. First, the “ballistic phase” involves the formation of the collision cascade arising from the high-energy “primary knock-on atom” (PKA) (or the recoil of alpha particle causing atomic displacements). This phase typically lasts only a few picoseconds, its net effect being the generation of FPs and small point-defect clusters.¹⁰⁹ Second, the “kinetic phase” captures the diffusion-controlled dynamical evolution of these FPs and clusters, their annihilation, and the formation of larger long-lived defect clusters. The evolution of FPs during these two phases is represented in Figure 7-1. During the ballistic phase, a sudden increase in the defects is represented by a rising curve (Figure 7-1(a)). The number of defects reaches a maximum (shown by peak) during this phase. At the same time, the high kinetic energy (KE) of the PKA is converted into potential energy (PE) of the defects (Figure 7-1(b)). In Figure 7-1(b), the peak-time in the number of defects (also same in Figure 7-1(a)) matches with the peak-time in the PE, thus illustrating the conversion of PKA KE to maximum PE of defects.

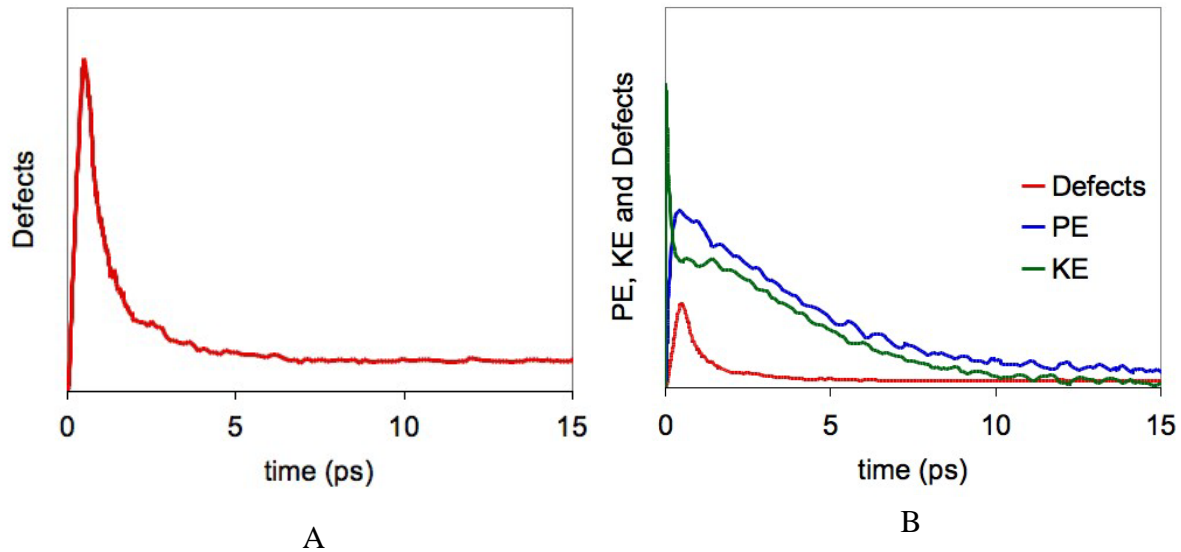


Figure 7-1. Two phases of radiation damage. A) Evolution of defects during the ballistic and kinetic phase. B) Distribution of kinetic energy (KE) and potential energy (PE) during the evolution of defects. Number of defects in (A) is a magnified view of defects' curve in (B).

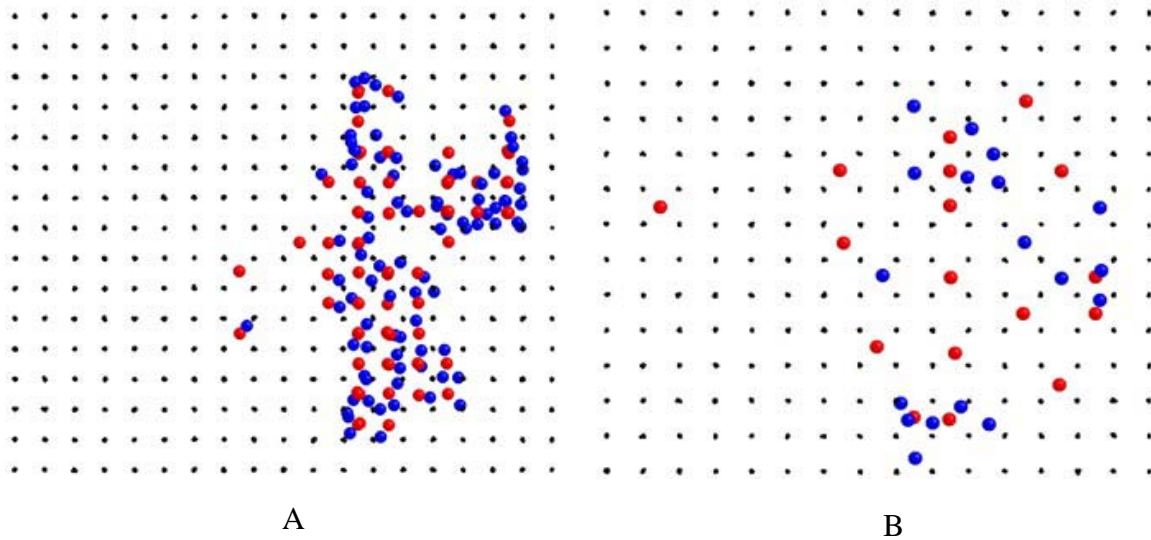


Figure 7-2. Typical Frenkel pair (FP) defects during radiation damage using PKA. A) Defects formation during the ballistic phase. B) Left-over defects during the kinetic phase.

This phase lasts only for few picoseconds after which, the FPs recombine and annihilate.

The fall in the number of defects (and PE) represents the recombination of the FPs.

During this time, a gradual transition from the ballistic phase to the kinetic phase takes

place. During the kinetic phase, most of the energy has been dissipated throughout the system (in the simulation, a thermostat is used to dissipate the energy) and the left-over defects diffuse to either recombine or form cluster. Schematics of the defects during the ballistic phase and kinetic phase are shown in Figure 7-2.

Large number of defects in Figure 7-2(a) represents the peak during ballistic phase.

Figure 7-2(b) represents the leftover defects during the kinetic phase. Most of the defects created during the ballistic phase recombine and annihilate. Thus, it is this kinetic phase that determines the long-time, experimentally accessible behavior of the material: while the recombination events promote radiation tolerance, the cluster-formation process produces the irreversible damage that degrades materials performance and ultimately limits lifetime.

Previous simulations of collision cascades followed by rather long temperature-accelerated dynamics (TAD) simulations^{107,110} have shown that the defect evolution during the kinetic phase is largely independent of the detailed nature of the initial damage created during the ballistic phase, suggesting that on a longer time scale, the role of the ballistic phase in the cascade simulation is mostly to introduce non-equilibrium point-defects into the system.

7.4.2 Kinetically-evolving Irradiation-induced Defects Method

Standard collision cascade radiation-damage simulations involving a PKA introduce only rather a small number of such point defects into the system. Thus a key question is whether these simulations are able to produce the wide range of defect environment present in experiments. Moreover, because it has been shown for some ionic systems, such as UO₂, that the initial propagation direction of the PKA has little effect on the ultimate defect evolution,¹¹¹ it appears that, at least in some cases, a rather complete

understanding of defect recombination, annihilation at sinks and clustering can be obtained by focusing on the kinetic phase alone. While standard radiation-damage MD simulations using the PKA approach capture the formation of the defects, they are not ideal for capturing the longer-time evolution of the systems. Most importantly, typically they are not long enough in duration to allow the formation of complex defect structures.

Here an approach is described that, by circumventing the ballistic-phase entirely, allows a much wider range of different defect environments to be explored. In this method, at the beginning of each simulation, a specified number of point defects (FPs) are created in a high-temperature equilibrated system. To avoid uninteresting and spontaneous interstitial-vacancy recombination events, the vacancies and interstitials are separated by a distance greater than the recombination radius. The system is then let to equilibrate at a high temperature and the diffusion-controlled kinetic evolution of the system is followed.

It can be argued that this method results in unrealistically large concentrations of defects. While this may be true when averaged over time and space, statistically it can be expected that such high defect concentrations will on occasion be generated over some spatial region. Moreover, the resulting defect structures, unlike rapidly recombining point defects, can have a significant role in determining the true radiation performance of the material.

This approach does not replace cascade simulations aimed at elucidating the effects of experimental conditions, such as the mass, energy and dose of the incident species on initial defect production. Rather, it is complementary in that it aims to capture more comprehensively the wide range of defect processes and kinetically evolving defect

environments that are rather insensitive to the details of specific cascade events. This approach allows to observe defect evolution under different defect environments and reveals the governing mechanism in the radiation tolerance.

In application to MgO as a model material, it is demonstrated that this approach replicates the defect clusters seen in the full cascade simulation followed by the TAD simulation.^{107,110} More importantly, it exposes a novel, previously unidentified intricate cluster-formation mechanism that involves not only the original, radiation-induced FPs but also formation of new “structural” FPs as a lattice response that stabilizes the larger clusters. This approach thus offers a simple, computationally straightforward and physically transparent way of elucidating the kinetic interplay among defect recombination, annihilation at defect sinks, and clustering in the development of radiation damage.

7.4.3 Materials Under Study

In this study, MgO and UO₂ are chosen to understand the radiation damage in ionic materials. MgO is chosen as a model material to prove the fidelity of the new method. It is motivated by the availability of previous simulations by Uberuaga *et al.*^{107,110} of relatively low PKA-energy (0.4-5.0 keV) cascade simulations that revealed that most of the FPs formed in the ballistic phase recombine during the kinetic phase. Those FPs that did not recombine were seen to evolve kinetically to form highly-stable clusters, their size ranging from di-interstitials to a maximum of seven ions. Particularly noteworthy is the fact that these clusters were not formed during the ballistic phase but as a consequence of interstitial diffusion during the kinetic phase in which the defects diffused long distances and were not confined to the region affected by the initial ballistic cascade.

From the technological viewpoint, MgO is a widely used as engineering material and is generally very well understood both experimentally and computationally. Furthermore, robust MgO empirical potentials are available that capture point defects phenomenon very well. UO₂, on the other hand, is a key component for fission reactors in nuclear-fuel rods. Understanding radiation damage in UO₂ is important to enhance the fuel performance. Also, since it has a fluorite crystal structure, it also serves as a model material to understand the radiation damage in the envisioned fluorite-related host materials⁹⁹ for the nuclear waste. This chapter illustrates radiation damage in MgO where, not only the new radiation damage methodology is demonstrated but also the key cluster-formation mechanisms in MgO are revealed, which have not been known before. In Chapter 8, radiation damage and clustering processes in UO₂ are revealed.

7.5 Interatomic Potential and MD Simulation

Our MgO single-crystal simulation cell consists of 20x20x20 cubic rocksalt unit cells, containing 64,000 ions. Periodic boundary conditions are applied in all three directions. The time step of 0.5 fs ensures good energy conservation in tests in the NPE ensemble. The short-range (mainly repulsive) interionic interactions are described by Lewis and Catlow's¹¹² rigid-ion Buckingham-type potential. The long-range electrostatic interactions are evaluated via direct-summation method³⁸ with spherical truncation at the cut-off radius of 8.139 Å. The zero-temperature lattice parameter thus obtained is $a_0=4.1986$ Å. All defect simulations are carried out in the NPT ensemble at 1000 K (the melting temperature of MgO for the potential used here is ~ 3250 K).¹¹³ At 1000 K, both Mg²⁺ and O²⁻ interstitials are highly mobile, whereas the corresponding vacancies are completely immobile on the MD time scale.

7.6 Results

At the beginning of each simulation, a specified number of FPs is randomly distributed throughout the system; to ensure their stability, i.e., to minimize uninteresting and spontaneous recombinations, the interstitials and vacancies are initially separated by a distance of at least $5a_0$. Because they cannot mutually annihilate, there is no constraint on the vacancy-vacancy or interstitial-interstitial distances; thus some are actually quite close to each other. In order to elucidate the nature and mechanism of defect clustering during the kinetic phase, two distinct types of starting configurations are considered. In the first, FPs are only inserted into either the Mg or the O sub-lattice, but not both; in the second, equal numbers of FPs are inserted into both sub-lattices.

7.6.1 FPs Only on One Sublattice

Initially, 100 FPs of Mg are created and the system is allowed to thermally equilibrate at 1000 K. After 2450 ps, only 18 Mg FPs are present. The schematic evolution of the defects on Mg sublattice is shown in Figure 7-3. The initially created 100 Mg FPs eventually recombine by interstitial-vacancy recombination. No Mg interstitial clustering is observed; as is shown below, this is due to the absence of oppositely-charged O FPs. Similarly, 100 FPs were created on the O sub-lattice. As in the case of the Mg FPs, eventually complete annihilation takes place with no clustering occurring on O sub-lattice due to the absence of the Mg FPs (Figure 7-4). In a conventional collision-cascade simulation it is, of course, not possible to selectively create defects on only one of the sub-lattices; this demonstrates a unique aspect of this approach in understanding the defect evolution. These simulations provide a baseline against which to compare the results of simulations of FPs on both sub-lattices.

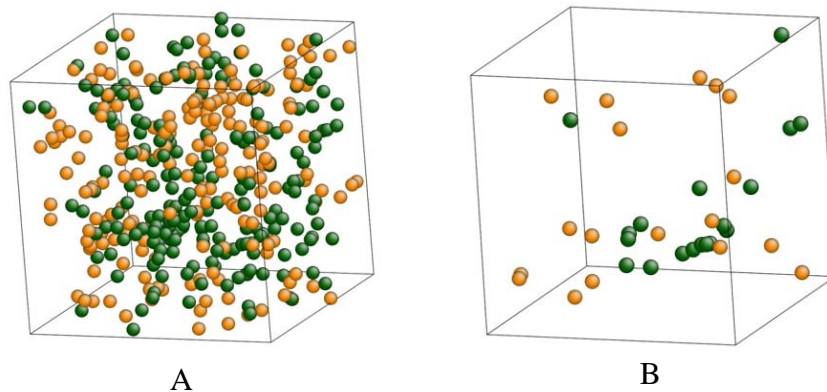


Figure 7-3. Evolution of FPs on Mg sublattice. Snapshots taken at A) $t=0$ and B) $t=2450$ ps showing the evolution at $T = 1000$ K of 100 FPs initially introduced on Mg sublattice. Of the initially 100 Mg FPs in (A), only 18 Mg FPs are left behind in (B). Dark green and orange spheres represent Mg interstitials and vacancies; eventually all Mg FPs recombine and annihilate.

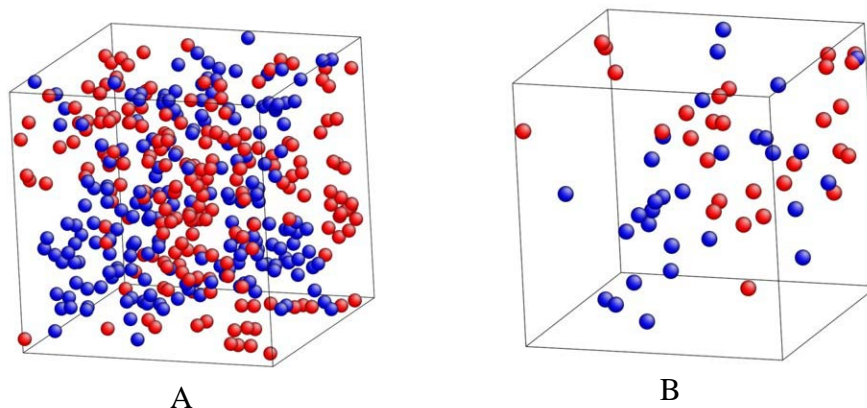


Figure 7-3. Evolution of FPs on O sublattice. Snapshots taken at A) $t=0$ and B) $t=2450$ ps showing the evolution at $T = 1000$ K of 100 FPs initially introduced on O sublattice. Of the initially 100 Mg FPs in (A), only 26 Mg FPs are left behind in (B). Red and blue spheres represent O interstitials and vacancies. Eventually all O FPs recombine and annihilate.

7.6.2 FPs on Both Sublattices

Next, equal numbers of FPs are simultaneously inserted into both the Mg and O sub-lattices. This scenario corresponds to electron radiation commonly used to produce single vacancies and interstitials.¹¹⁴ It also resembles the situation at the end of the ballistic phase of a collision-cascade radiation-damage simulation. Figure 7-5 shows two

snapshots taken again at (a) $t=0$ and (b) $t=2450$ ps for a system containing initially 100 FPs on each of the two sub-lattices. Compared to the case of Mg or O FPs only, this annealing simulation reveals much less interstitial-vacancy recombination but, instead, significant interstitial aggregation into clusters. This aggregation starts quickly by the formation of highly mobile di- and tri-interstitials. Identical di- and tri-interstitial clusters were observed in the lower-temperature, combined collision-cascade and TAD simulations by Uberuaga *et al.*^{107,110}

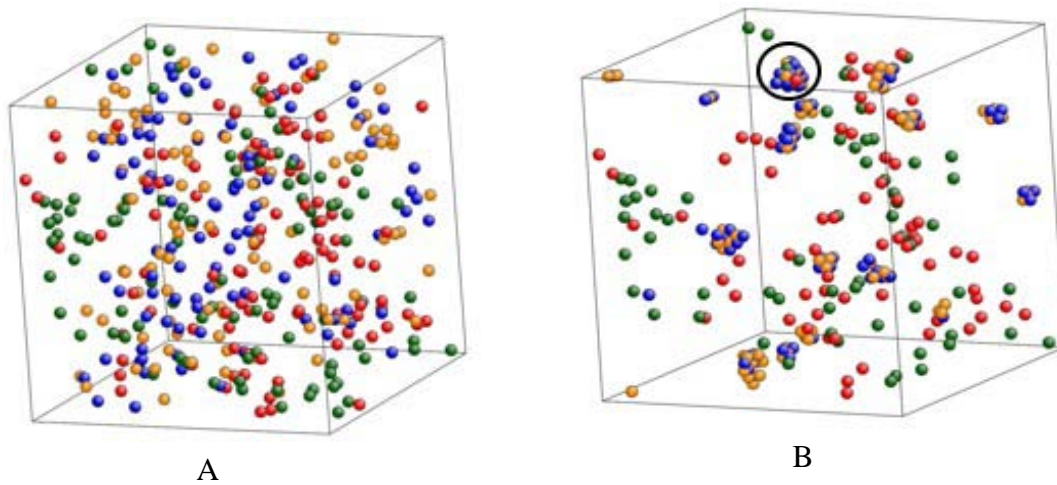


Figure 7-5. Snapshots taken at A) $t=0$ and B) $t=2450$ ps showing the evolution at $T = 1000$ K of 100 FPs initially introduced into each of the two sub-lattices. Of the initially 100 Mg and 100 O FPs in (A), 72 Mg and 76 O FPs are still present in (B).

While nearly all of the $\text{Mg}^{2+}\text{-O}^{2-}$ di-interstitials combine to form larger clusters, only a few of the tri-interstitials (of both kinds: $\text{Mg}^{2+}\text{-O}^{2-}\text{-Mg}^{2+}$ and $\text{O}^{2-}\text{-Mg}^{2+}\text{-O}^{2-}$) aggregate to form larger clusters; the others maintain their individual tri-interstitial identity. Both the tri-interstitial and the larger-sized interstitial clusters are found to be very stable in that they survive to the end of the simulation at 2450 ps.

During this annealing simulation, the majority of FP annihilation events by vacancy-interstitial recombination occur very quickly (within the first 50 ps), during

which period each of the defect types is fairly evenly distributed in space. Once interstitials aggregate into clusters, the likelihood of further vacancy-interstitial recombination quickly decreases in favor of cluster growth by interstitial capture. Any remaining single interstitials therefore quickly disappear from the system; in fact, after about 2000 ps, virtually no individual interstitials are left. This is quantified in Figure 7-6, which compares the number of Mg^{2+} interstitials present in a system with FPs only on the Mg sub-lattice with a system with FPs on both sub-lattices.

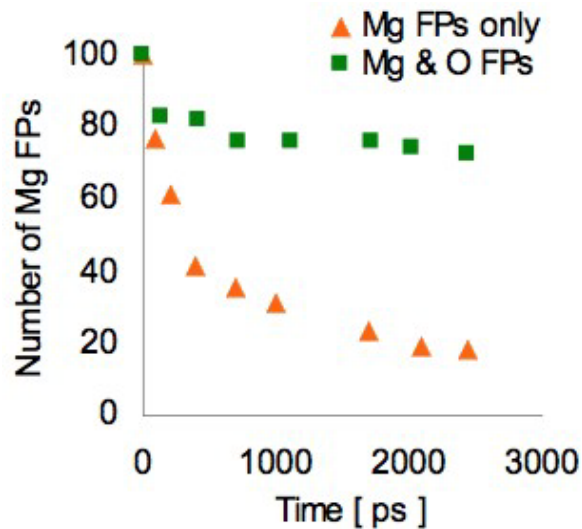


Figure 7-6. Total number of Mg FPs present in the simulation cell vs. time when the system is initialized with Mg defects only (triangles), and both Mg and O defects (squares).

This comparison demonstrates that, when the FPs are present on only one sub-lattice, all the vacancies and interstitials eventually recombine due to the absence of clustering; hence, after 2450 ps only ~20% of the initial FPs remain. By contrast, in the system containing FPs on both sub-lattices, about 80% of the FPs become immobilized by precipitation into highly stable vacancy-interstitial clusters; in fact, after only 1000 ps the FP count levels off (see Figure 7-6).

The stability of these clusters is most likely strongly enhanced by being stoichiometric, and hence charge neutral. Similar simulations with very low concentration of point defects simultaneously on both the sub-lattices also result in di- and tri-interstitial clusters that maintain their identity for the entire 2500 ps of the simulation.

7.7 Cluster-Formation Mechanism

A close-up snapshot of one of the larger interstitial clusters, circled in Figure 7-5(b), is displayed in Figure 7-7. Investigation of the dynamic growth mechanism of this representative cluster reveals *two* distinct, coordinated mechanisms that control its formation and growth.

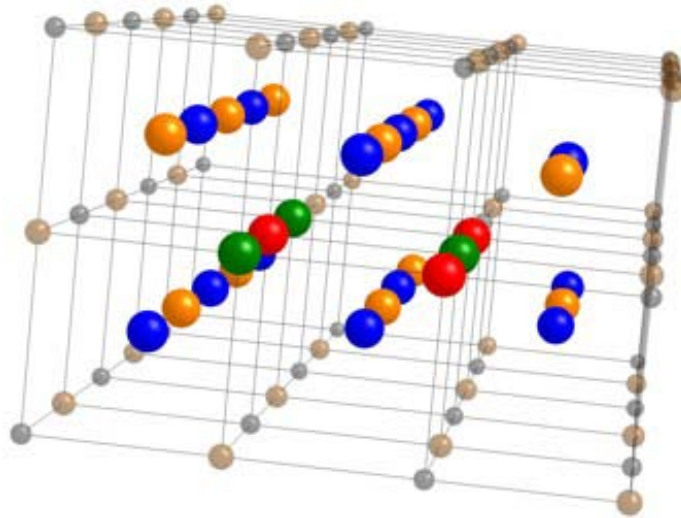


Figure 7-7. Close-up of the all-interstitial cluster circled in Figure. 7-5 (B). The cluster forms an interstitial rocksalt lattice that is displaced with respect to the parent lattice.

These are: (i) the conventional mechanism involving diffusion-controlled aggregation and annihilation of the originally introduced interstitials, and (ii) the spontaneous formation of *new*, “structural” FPs by the coordinated displacements of lattice atoms within the cluster core. The coordinated operation of the two mechanisms is illustrated in Figure 7-8 which captures four sequential hopping events (see arrows) during the growth

and stabilization of a cluster containing initially four Mg^{2+} and five O^{2-} interstitials together with one Mg and one O vacancy, Figure 7-8(a). (A cluster with this structure was also observed in the earlier simulations^{107,110}). Arrow 1 indicates oxygen diffusion to a neighboring interstitial site while arrow 2 captures the annihilation of an oxygen FP by interstitial-vacancy recombination.

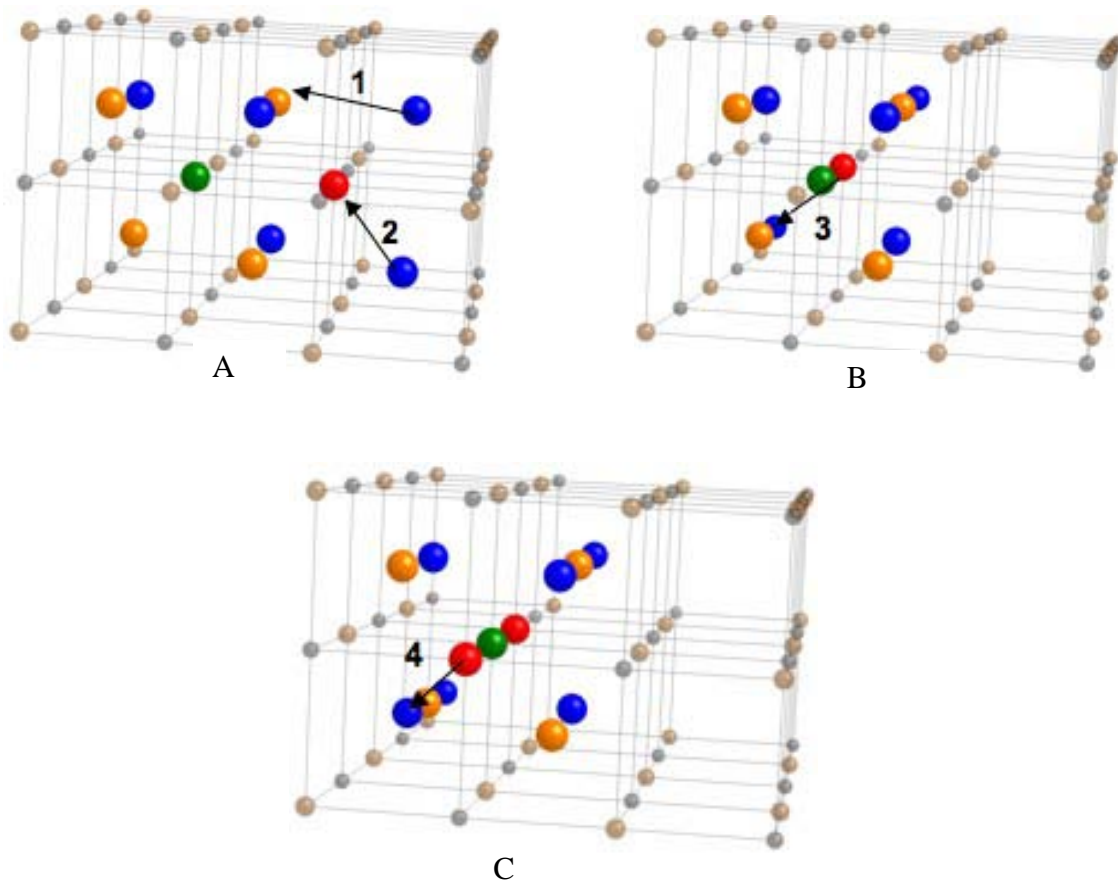


Figure 7-8. Two distinct mechanisms control the growth of an interstitial MgO lattice within the host lattice. The interstitial cluster A) contains four Mg^{2+} (orange) and five O^{2-} interstitials (blue) together with one Mg (green) and one O (red) vacancy. Black spheres represent Mg^{2+} and brown spheres O^{2-} ions in the MgO parent lattice. B) The spontaneous formation of a *new* oxygen FP within the cluster contributes to the growth of the cluster while simultaneously stabilizing it energetically. C) The spontaneous formation of a second oxygen FP completes one cubic unit cell of the interstitial MgO lattice.

Both are conventional diffusion events of interstitials already present at the beginning of the kinetic phase. By contrast, Figure 7-8(b) reveals a novel mechanism involving the spontaneous creation of a new (not initially present) FP as a regular-lattice O ion hops to an interstitial site (arrow 3), leaving behind a newly created vacancy within the cluster core; this event is then repeated in Figure 7-8(c); arrow 4.

Two additional ions already present at the back of the interstitial cube in this figure act as nucleation sites for the completion of the next, adjacent cube. The net outcome of these events is a complete cube of an interstitial MgO crystal that has been formed and that continues to grow, on the displaced, interstitial lattice.

7.7.1 Crystallography of the Cluster

To elucidate the driving force for the spontaneous creation of new FPs in the cluster core, previous work on the nature of long-range forces in rocksalt-structured crystals is recalled that has shown that a finite-sized crystallite is terminated such that the basic cubic building blocks remain intact.¹¹⁵ The reason for this is that any break-up of these charge neutral, dipole-moment-free, octopolar (MgO)₄ building blocks creates long-ranged dipolar forces that significantly increase the Coulomb energy of a finite-sized crystal.¹¹⁵ This analysis has been confirmed in numerous experiments¹¹⁶ and additional simulations¹¹⁷ that revealed that rock-salt structured surfaces, indeed, consist of complete octopolar building blocks (Figure 7-9), thereby eliminating any long-range dipole moment perpendicular to the surface.¹¹⁵

The crystal structure of the interstitial cluster is same as that of the parent crystal structure, i.e., both have rocksalt crystal structure. In a building block (here (MgO)₄) of a rocksalt crystal structure, every Mg ion is followed by an O ion and vice-versa (Figure 7-

10 (a)). Mg and O occupy 4a and 4b Wyckoff sites respectively. Inside this building block, there is one empty octahedral site, Wyckoff 8c.

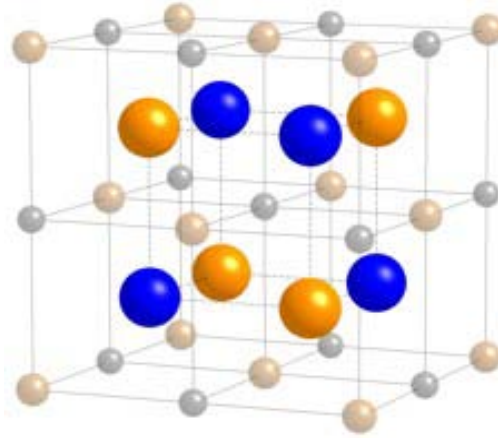


Figure 7-9. A $(\text{MgO})_4$ octopolar. Decrease in the Coulombic energy is the driving force for the formation of a dipole-moment free octopolar cluster.

It is this site that is occupied by the interstitial (say Mg, Figure 7-10(b)). If one of the crystallographic directions is translated to juxtapose next rocksalt building block, the next octahedral site is now occupied by an opposite ion, O (Figure 7-10(c)). Similarly, by building rocksalt crystal structure in three dimensions, it is found that the interstitial cluster is formed by alternating Mg and O ions that occupy alternating octahedral sites (Figure 7-9). Hence, interstitial cluster also maintains rocksalt crystal structure which is same as the parent crystal structure.

This crystallography of interstitial cluster is unique for rocksalt-based materials. In UO_2 (Chapter 8), it is found that interstitial crystal structure does not maintain the parent crystal structure due to the crystallographic limitation. Whereas in MgO, multiple unit cells are involved in clustering mechanism, and the cluster size is not limited, in UO_2 , the cluster is limited to only one unit cell.

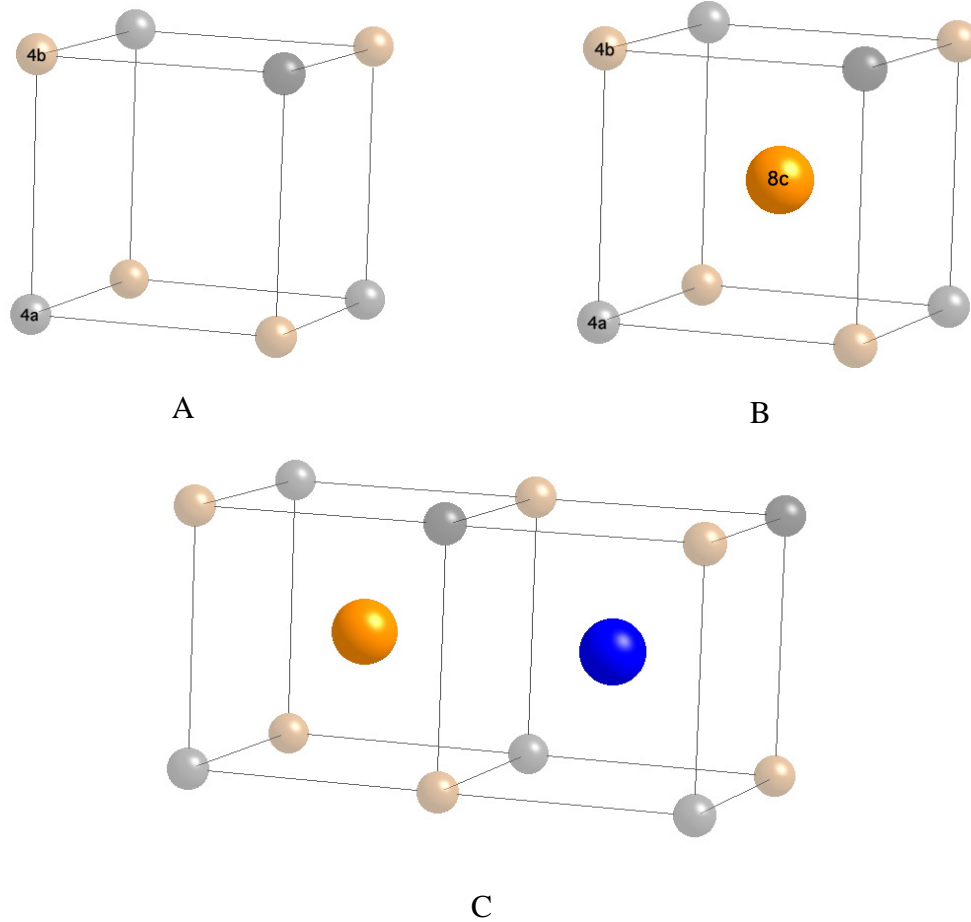


Figure 7-10. Crystallography of MgO rocksalt lattice. A) A $(\text{MgO})_4$ building block in which Mg occupy 4a and O occupy 4b Wyckoff sites. B) An octahedral interstitial position with Wyckoff site, 8c. C) In two MgO juxtaposed building blocks, alternate octahedral sites are occupied by opposite ions, Mg and O.

7.8 Discussion

Applied to the observations in Figure 7-8, this means that the mechanism of formation of the interstitial MgO lattice should evolve by progressive formation of complete cubic $(\text{MgO})_4$ building blocks. In view of this, the creation of the “structural” FPs appears to be simply a way to form complete octopolar building blocks, thereby lowering the total energy of the interstitial MgO crystallite. It is emphasized, however, that the FP creation mechanism is a cluster-stabilizing effect that does not happen

independently in perfect-crystal regions; it is therefore only indirectly related to the radiation-induced FPs from the ballistic phase. Similar behavior in UO_2 is observed where new FPs are created in the oxygen sub-lattice; however, the details of clustering mechanism are different.¹¹⁸

Temperature-accelerated dynamics (TAD) simulations^{107,110} have extended the reach of PKA simulations out to macroscopic time scales. However, PKA simulations of one or a few cascades correspond to low defect concentrations, thereby limiting the complexity of the defect structures that can evolve. By injecting a very high density of Frenkel-pair defects, the present method much more readily allows large clusters to develop. Moreover, this high density essentially allows nanosecond simulations to not only produce defect structures only previously seen in much longer simulations, but also produces heretofore unreported defect structures. Because the initial defect concentration is extremely high, it might be argued that the dynamically generated complex defect structures seen here may in reality be rather uncommon. However, given that single defects and small clusters are annihilated as the system evolves, it is precisely these large, structurally complex clusters that will survive and constitute the long-term radiation damage in the system.

A similar methodology of sprinkling of defects has also been followed in Monte Carlo (MC) simulation of radiation damage.^{119,120} However, such MC simulations require prior knowledge of the specific atomic-level mechanisms and energetics. Such prior information is not required in these MD simulations; indeed, these simulations are capable of providing the mechanistic and energetic input required for the MC simulations.

To conclude, by complementing the cascade simulations, this robust and straightforward approach enables elucidation of the kinetics of radiation-damage development unencumbered by the initial damage due to one specific cascade. By following only the kinetic evolution at elevated temperature, it enables observation of defect aggregation up to significant cluster sizes, and with mechanistic detail not previously possible. In addition, the ability to selectively create defects on only one of the sub-lattices provides an additional perspective on the nature of radiation-damage development. Since it does not require particularly large system sizes, the approach thus provides a relatively simple and direct route for elucidating the competing roles of point-defect annihilation and aggregation in the development of radiation damage, including host-lattice responses in the process.

CHAPTER 8 RADIATION DAMAGE IN UO₂

8.1 Introduction

In Chapter 7, the capability of the new approach to perform radiation damage MD simulations in elucidating the evolution of defects in MgO is demonstrated. In this Chapter, same methodology is employed to elucidate point defect evolution in fluorite-based UO₂.

Fluorite-based materials are widely used in the nuclear applications both as nuclear fuel and in the nuclear waste repository. In these applications, the irradiating high-energy particles cause damage by creating point defects, clustering of which can form defects structures such as cluster, dislocations, voids and stacking faults, ultimately leading to material failure. The damage tolerance of a material not only depends on the number of defects created during irradiation but also on their long time kinetic evolution; understanding the complete evolution of defects is therefore very important. Computer simulations play a key role in complementing experiments by revealing important radiation-induced fast atomistic phenomenon^{106,108,99,121} that are otherwise impossible to capture. UO₂ is a commonly used material in both nuclear applications in which radiation effects have been studied, for a long time, experimentally,^{122,123,124,125} and more recently, computationally.^{126,127} The simulations have however been limited only to the initial collisional phase of damage; extending the time scale to elucidate computationally-accessible complete defect-evolution mechanisms is therefore the next step.

Under oxidizing conditions, UO₂ readily accommodates O interstitials to form UO_{2+x}. Ultimately, these interstitials lead to a transformation to another distinct phase, β -U₄O₉,¹²⁸ with a structure closely resembling that of fluorite. A unit cell of β -U₄O₉ has

space group of $\bar{I}43d$ and consists of a cluster of oxygen interstitials and vacancies known as cuboctahedral (COT) cluster (Figure 8-1).^{129,130} In this structure, U atoms occupy positions very close those in the fluorite positions of UO_2 while O atoms form a COT cluster inside the unit cell. In comparison to eight oxygen atoms inside a unit cell of fluorite UO_2 , $\beta\text{-U}_4\text{O}_9$ has twelve oxygen atoms situated on the 12(b) position of $\bar{I}43d$.

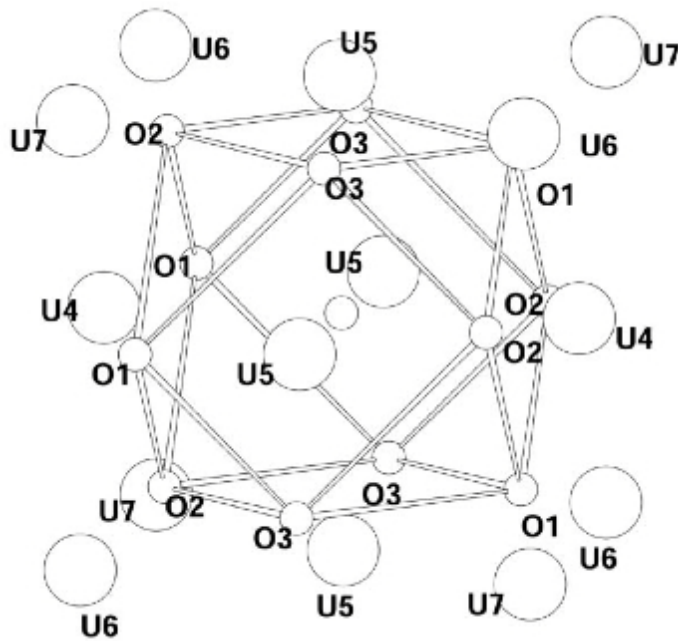


Figure 8-1. $\beta\text{-U}_4\text{O}_9$ crystal structure. In this structure, U atoms occupy same positions as in fluorite UO_2 . O atoms form a cuboctahedral cluster by occupying 12(b) positions in space group $\bar{I}43d$. (Reproduced from reference 130)

Under irradiation of UO_2 , there can be a local increase in the oxygen interstitial concentration near the damage site. Under these conditions, it is possible that cluster formation might cause a local phase transformation, changing the crystal structure and thereby affecting the radiation tolerance. In this work, MD simulations are used to elucidate the evolution of irradiation-induced point defects in UO_2 , including the formation mechanism of COT clusters in the fluorite matrix.

8.2 Simulation Methodology

While applying the method mentioned in Chapter 7 to MgO,¹³¹ it was able to reproduce the clusters that were observed from the combined radiation damage MD-TAD simulations.¹¹⁰ Moreover, by focusing entirely on the kinetic phase of radiation damage, this method allowed to better understand the defect recombination and clustering mechanism in MgO. In particular, because the defects are created by hand, it allows to choose the sub-lattice to create the defects and therefore, to elucidate, for example, the defect evolution on one sublattice in the absence of defects on the other sublattice.

8.2.1 Interatomic Potential and Molecular Dynamics Method

The interactions between the ions are described by a pair-potential. Here, the short-range atomic interactions are captured using the potential form provided by Bushing-Ida *et al.*¹³² with parameters taken from Basak *et al.*¹³³ In addition to the widely implemented Buckingham-type form for the ionic materials, the Bushing-Ida potential form also includes a Morse term that introduces a “covalent” component. Due to the assumption of partial covalency, the ionic charges are given non-formal values, which take into account partial charge transfer between the ions.

The melting point for this interatomic description of UO₂ has been determined to be $\sim 3450 \pm 50$ K,¹³⁴ which is in fair agreement with the experimental value of 3100 K^{135,136}. Likewise, the oxygen sub-lattice ordering temperature for this potential has been determined to be 2200 K¹³⁴ which is also in fair agreement with the experimentally-obtained value of 2600 K.¹³⁷ Throughout this work, all simulations have been carried out at a temperature of 1000 K, which is well below the melting and sub-lattice melting temperatures. At this temperature, the oxygen interstitials and vacancies have high diffusivities, whereas the uranium counterparts have very high migration energies and

therefore are less mobile; this temperature is also representative of the temperature range of 800 – 1600 K present in a typical fuel pellet.

In order to elucidate the interplay of U and O point defects at elevated temperature, all simulations are carried out on UO₂ single crystal containing 96,000 ions. An MD time step of 0.5 fs is used which is small enough to conserve energy for several thousand MD steps in NVE test runs. To capture as much of the defect evolution as possible, all the simulations have been carried out for more than 1 ns. The point defects, i.e., vacancies and interstitials, are identified by comparing the structure with defects at any time with the initial structure containing no defects. If any lattice site does not contain an atom within a spatial cut-off radius of 1 Å, the site is identified as a vacancy.

8.2.2 Diffusion-controlled Kinetic Evolution of Defects

From multiple simulations, it is observed that the defect environment on one sub-lattice significantly influences the point-defect evolution on the other. To illustrate this, point defects are randomly created either on one sub-lattice or both, and let the system equilibrate at 1000 K. All the vacancies of each type are separated by at least $5a_0$ from their counterpart interstitials. In the following section, multiple simulation results distinguished by the defects on one or both sub-lattices are discussed.

Our first simulation was performed on a system containing no defects. The system was equilibrated for a sufficiently long time at 1000 K. As expected, the analysis of the structure shows no defects at any stage. This structure is used as the starting point for the simulations that are discussed in detail here.

Figure 8-3. By 1400 ps, only four O FPs are left in the system. Eventually, all of the O FPs recombine by vacancy-interstitial recombination mechanism; no interstitial-interstitial or vacancy-vacancy clustering is observed. This demonstrates that, in the absence of defects on U (or cation) sub-lattice, the O sub-lattice is completely healed within a few picoseconds, resulting in no long-lasting damage to the material.

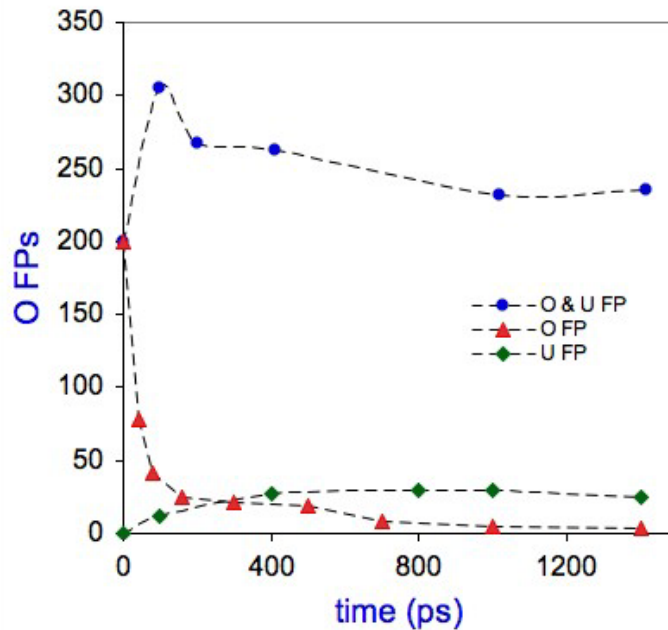


Figure 8-3. Total number of O FPs present when the system is initialized with three different defect conditions: (1) defects present only on O sub-lattice (red triangles); (2) defects present only on U sub-lattice (green diamonds) and (3) defects present on both O and U sub-lattices (blue circles); In contrast to (1), in other two cases, new FPs are created in O sub-lattice when defects are also present on U sub-lattice.

In contrast to the above expected result, the simulation of FPs on the U sub-lattice alone yield a surprise. 200 FPs are created only on U sub-lattice. The initial snapshot of the system with defects is shown in Figure 8-4 (a); snapshots at later times are shown in Figures 8-4 (b) and 8-4 (c). Since, the U interstitials and vacancies have very high migration energies, recombination events are less frequent. Out of the initial 200 U FPs,

160 U FPs are still present after 1700 ps. This is as expected based on the high migration energies of U vacancies and interstitials. What was not expected, however, was that the high concentration of the defects on the U sub-lattice nucleates O FPs. This is shown as the diamonds in Figure 8-3. Starting from no O FP at $t = 0$ ps, there is a gradual increase in the number of O FPs; this peaks at ~ 600 ps with a total of ~ 30 FPS, and then slowly decreases; however even after 1700ps about 20 O FPS remain (Figure 8-4 (b)).

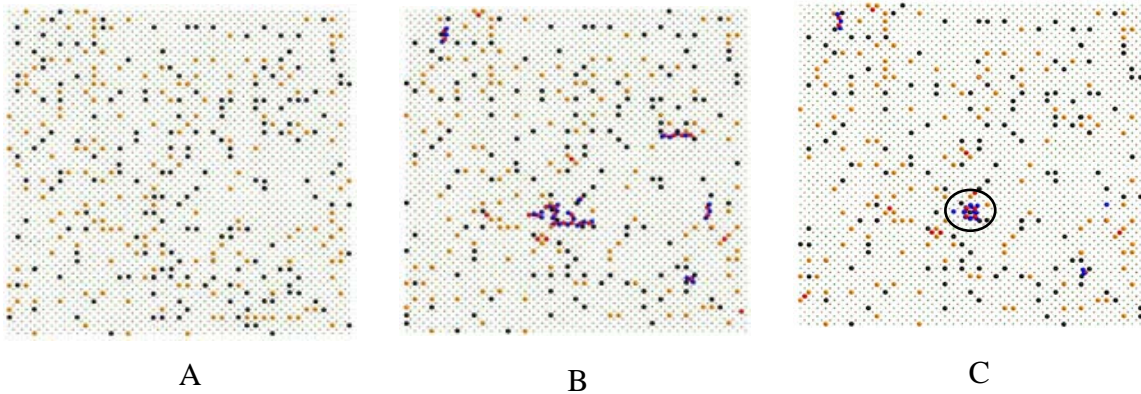


Figure 8-4. Evolution of the point defects present only on the uranium sub-lattice. A) $t = 0$ ps, initially 200 FPs were randomly distributed on the uranium sub-lattice. The U vacancies and interstitials are less mobile at this temperature. Therefore, only few recombination events take place. B) At $t = 1000$ ps, due to the large number of U defects, some new O FPs are created which diffuse with time. C) At $t = 1700$ ps, the interstitials diffuse and form a cluster shown as circled. (See Figure 8-7 for details on cluster).

Although most of vacancies and interstitials that make up these O FPs remain close to each other (within $2a_0$), some of them diffuse far enough from their counterpart to suggest their potential for long-term stability. Indeed, some of the defects are no longer isolated but, as seen in Figure 8-4 (c), actually form clusters. A detailed analysis of these structures is given below. What is most noteworthy here, however, is the observation that the presence of the defects on the U sub-lattice leads to the spontaneous formation of O FPs, whose diffusion controls the longer time scale evolution of the system.

remain at the end of the simulation. The time evolution of the effective O FPs concentration shows a large initial increase within the first 100-150 ps, followed by a slow decline. Instead of almost complete elimination of the O FPs at the end of the simulation, their number is actually larger than at the beginning of the simulation.

This indicates that there are two different phenomenon taking place simultaneously. First, in few cases, random diffusion of the vacancies and interstitials results in their elimination by recombination. Second, more interesting, and responsible for the sharp increase, is the formation of *new* O FPs. These are created by an O ion spontaneously displacing from the regular lattice site to a nearby interstitial site. The unrecombined original O FPs and the newly created O FPs together evolve into clusters: while the O interstitials form COT clusters, the O vacancies form Schottky defects with the U vacancies. The structures of these clusters are discussed in detail below.

Considered together, these three simulations illustrate two important points: First, U FPs influence the radiation tolerance of UO_2 . The presence of U FPs not only prevents O FPs recombination, but also in certain cases contributes to creation of new ones. This in turn shows that radiation tolerance of UO_2 decreases if the U FPs remain in the system. Second, from the methodology viewpoint, this approach of selectively creating defects on different sub-lattices, allows better understand the defect evolution mechanisms.

8.2.5 Vacancy Clustering: Schottky Defects

A Schottky defect consists of two O vacancies and one U vacancy. The evolution of vacancies into Schottky defects takes place in both the system with defects only on U sub-lattice and in the system with defects on both O and U sub-lattices. The O vacancies for the vacancy-cluster formation in the system with defects on both sub-lattices comes mainly from the O FPs created at the beginning of the simulation. For the system with

only U defects, the dynamically created O FPs contribute O vacancies to the Schottky defect. In both cases the process involves the diffusion of the mobile O vacancies to essentially stationary U vacancies. A snapshot of a Schottky defect is shown in Figure 8-5. Separate static calculations have shown that O-U-O vacancy cluster has a much lower energy than O-U di-cluster with a separate O vacancy.

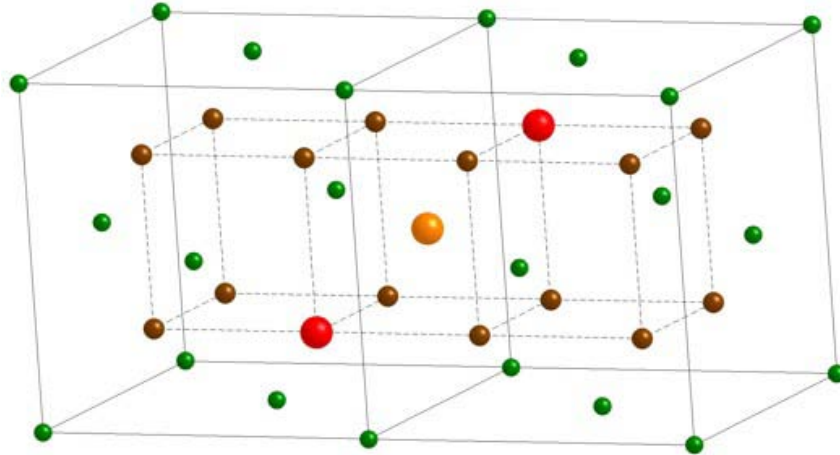


Figure 8-6. Schottky-defect formation. Two O vacancies tend to align in $\langle 111 \rangle$ direction around a U vacancy.

The system with completely separated vacancies has a higher energy yet. As a result, although the Schottky defect is created by diffusion, it is extremely stable. All of Schottky defects involve vacancies that are near neighbors of each other. While most of the Schottky defects form as $V_O-V_U-V_O$ along $\langle 111 \rangle$ (Figure 8-5), some form along $\langle 110 \rangle$. Regardless of the specific structure, the creation of these Schottky defects sequesters O vacancies, thereby making them unavailable for vacancy-interstitial recombination events. As it will be seen, this leads to the possibility of the O interstitials, whose potential recombination partners are in Schottky defects, forming complex defect structures.

8.2.6 Interstitial Clustering: Cuboctahedral Clusters

With the O vacancies segregated into the vacancy clusters, the O interstitials also evolve into clusters. The segregation of the interstitials into clusters is a rapid process and the vacancy and interstitial clustering occur simultaneously, provided the defects are available. In the system with defects on both sub-lattices, the interstitial clusters begin to appear within first 40 ps. On the other hand, in the system with defects only on U sub-lattice, it takes more than 1 ns before the newly formed O interstitials segregate and form clusters.

The O interstitials form COT clusters in both systems. These COT clusters contain twelve O interstitials and eight O vacancies inside a unit cell of UO_2 . Such interstitial clusters have been previously observed experimentally in the oxygen-rich UO_2 systems^{129,130,138} and have been found stable from electronic-structure calculations.¹³⁹ These simulations allow the dynamics of the formation process itself to be determined.

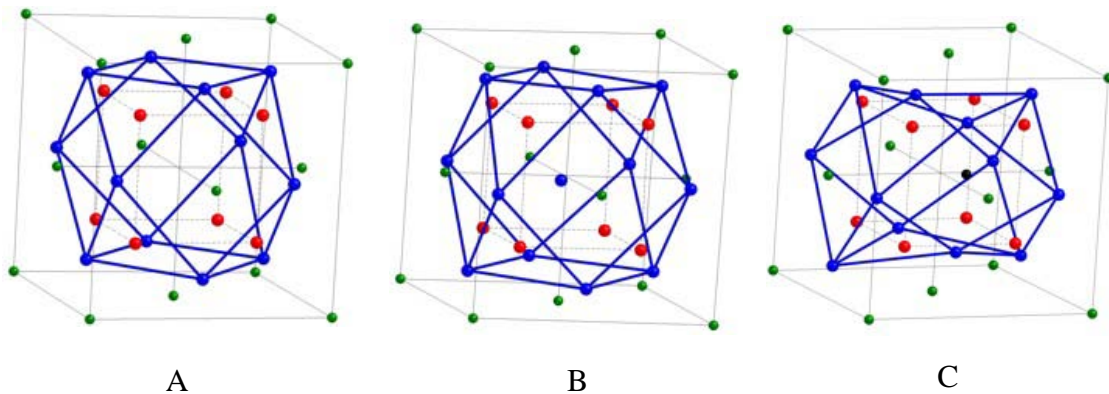


Figure 8-7. Three different kinds of cuboctahedral (COT) clusters as seen in Figure 8-5 differentiated by filled or empty octahedral site. The cubic oxygen sub-lattice has 4 O interstitials in addition to 8 original atoms. These extra interstitials displace the lattice oxygen atoms thereby creating, in total, 12 O interstitials and 8 O vacancies. The U lattice remains undisturbed. A) An empty COT cluster, B) O-filled COT cluster and C) U-filled COT cluster.

There are two different COTs, distinguished by the vacant (COT-*v*) or occupied (COT-*o*) octahedral site at their center. In the COT-*o* clusters, the octahedral site is occupied by an oxygen ion. In the simulations, in addition to these two previously described interstitial clusters, it is found that a U ion can also occupy the octahedral site inside the COT- cluster (COT-*u*). Figures 8-7 (a), (b) and (c) show the COT-*v*, COT-*o* and COT-*u* clusters, as spontaneously formed in the simulations.

In all of these clusters, while the U FCC lattice (green) remains undisturbed. By contrast the concept of an O sub-lattice begins to break down. In particular, rather than 8 O ions occupying the corners of cubic sub-lattice, there are 12 O interstitial ions and no ions at all occupying the sub-lattice sites. It would seem extremely unlikely that all of the 8 original O ions were displaced from their lattice sites. What actually happens is the addition of extra 4 O interstitials to a unit cell that previously had an un-defected O sub-lattice, leads to the 8 ions on the O sub-lattice being displaced from their positions. The result is that all 12 O ions finally reside in the interstitial positions. A crystallographic analysis of the COT clusters is given elsewhere.^{129,130}

The formation of such clusters would be extremely unlikely if it required all of the O ions to converge on a single unit cell at the same time. Indeed, the simulations show that the COT forms in a progressive manner, as illustrated in Figure 8-8 for the COT-*u* cluster; the COT-*v* and COT-*o* clusters form in a similar manner. Figure 8-8 (a) is a snapshot at $t = 3\text{ps}$ of a unit cell containing a U interstitial at its center. At this time, all the O sub-lattice sites are occupied. At $t = 4\text{ps}$, one diffusing O interstitial enters the unit cell; as a result two O ions move from their lattice sites to interstitial sites, creating the structure shown in (Figure 8-8 (b)). The unit cell now contains two O vacancies and three

O interstitials. In Figure 8-8 (c) at $t = 20$ ps, another O interstitial enters the unit cell, which creates two further O FPs. As a result, there are four new O FPs created in the unit cell by the addition of two O interstitials. Similarly, further addition of two more O interstitials creates four more O FPs.

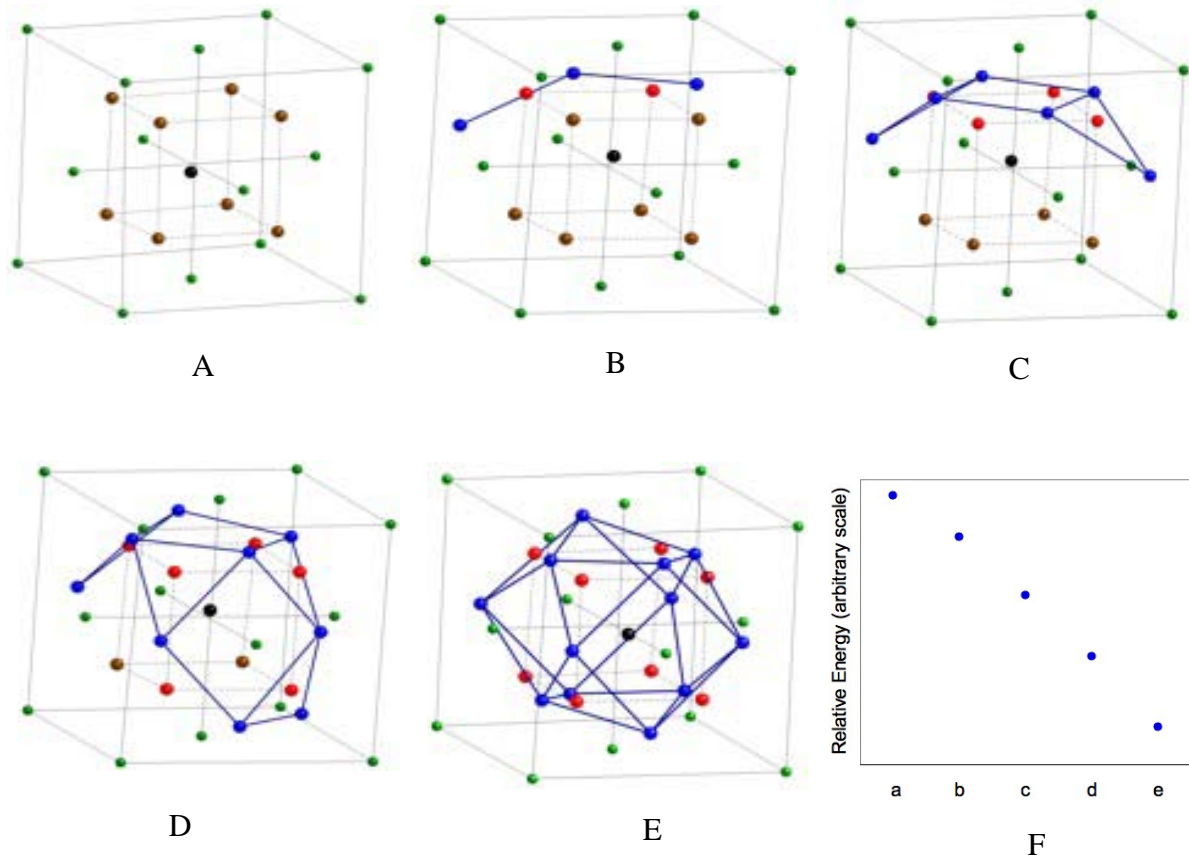


Figure 8-8. Progressive formation cuboctahedral (COT) cluster, as seen in an MD simulation. A) A fluorite unit cell containing U interstitial atom at the octahedral site at $t = 3$ ps. B) At $t = 4$ ps, a diffusing O interstitial enters the unit cell. Two oxygen atoms are knocked from their lattice site resulting in formation of two O vacancies and three O interstitials. C), D), and E) are snapshots at $t = 20$, 120 and 250 ps. For every additional O interstitial entering the unit cell, two oxygen atoms are knocked off from their lattice sites. F) The relative decrease in the energy of the system as the cluster is formed.

Thus, every addition of one O interstitial in the unit cell displaces two O atoms from their lattice sites thereby creating two new O FPs (shown in Figures 8-8 (d) and 8-8

(e)). Figure 8-8 (f) shows the energetics of the cluster formation. It illustrates the system favors cluster formation instead of separated O interstitials. The energy of the system decreases when the distributed O interstitials segregate and progressively form the COT cluster. The other two clusters, COT-*v* and COT-*o*, follow the same clustering mechanism. This formation mechanism of a COT cluster therefore explains the sharp increase in the number of the O FPs as was observed in Figure 8-3. For every complete cluster that appears in the system, there is an increase of 8 O FPs, with all of these new FPs appearing from the O displacements within a cluster. It has to be kept in mind that the new FPs are formed only because of an extra oxygen ion entering the unit cell; their independent formation has not been observed.

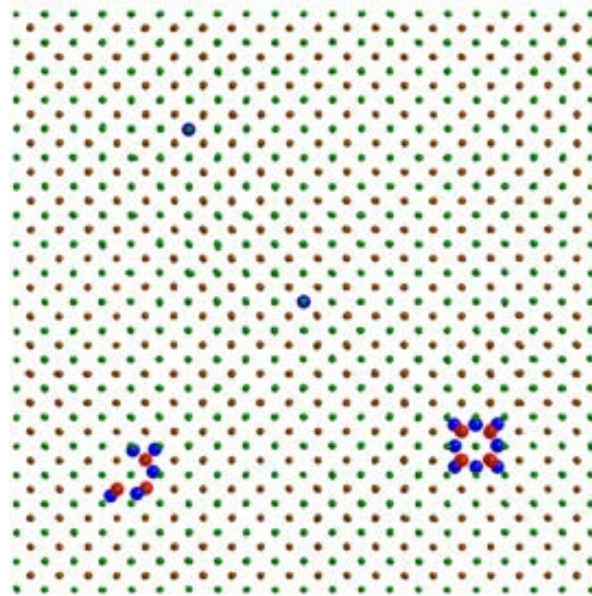


Figure 8-9. Clustering of oxygen interstitials in the absence of vacancies. Initially 4 U and 8 O interstitials were added to the system. The O interstitials diffuse and form cuboctahedral (COT) clusters. One cluster is complete while the second one is in the process of formation. The U interstitials (not shown here) remain immobile.

From the results, it is believed that O interstitial-cluster formation is stabilized by formation of Schottky defects. In the absence of U vacancies, the O vacancies can

recombine with the O interstitials. When U vacancies (and U interstitials) are present, O vacancies can be pinned in Schottky-defect clusters.

This forces the O interstitials to either remain isolated or form some sort of cluster. To illustrate this directly, simulations on systems containing only interstitials or only vacancies are performed. One simulation contained additional stoichiometric U and O interstitials (four extra U and eight extra O interstitials). A snapshot of the system at $t = 140$ ps is shown in Figure 8-9 (*U interstitials not shown*). The initially well-separated O interstitials diffuse and evolve into COT clusters. In Figure 8-9, one of the interstitial clusters is complete and the other one is in the process of construction.

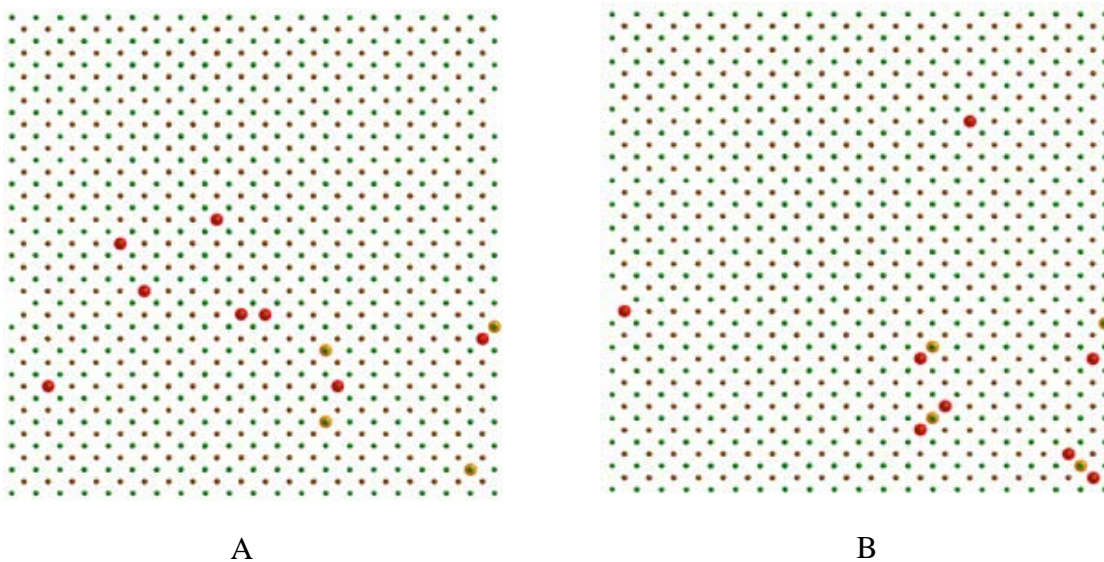


Figure 8-10. Snapshots showing clustering of U and O vacancies. A) At $t = 0$ ps, 4 U and 8 O vacancies are created in the system. B) O vacancies diffuse and cluster around U vacancies forming a $\langle 111 \rangle$ oriented cluster. Two $\langle 111 \rangle$ aligned clusters have formed by $t = 280$ ps.

A similar scheme is applied to understand the evolution of the independent vacancies.

Four U and eight O vacancies are created in the system. The snapshots of the initial structure at $t = 0$ ps and the equilibrated structure at $t = 280$ ps are shown in Figure 8-10.

Initially, all the vacancies are created randomly and sufficiently far away from each other

to prevent vacancy clustering. With time, the O vacancies segregate around the U vacancies to form Schottky defects. In Figure 8-10, two such clusters have already formed and one is in the process of formation.

8.2.7 Evolution of Disproportionately Defected Systems

Up to this point, the point-defect clustering process and the independent evolution of vacancies and interstitials is illustrated. Here, the interdependence of the evolutions of O FPs on that of U FPs is presented.

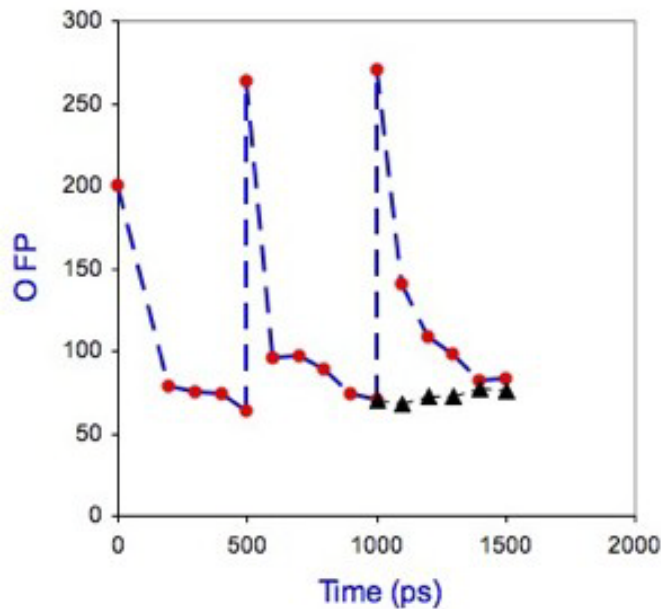


Figure 8-11. O FP evolution in a system initially containing 200 O FPs and fixed U FPs. After 500 ps, the number of O FPs levels off to ~ 60. Another 200 O FPs are added at 500 ps and 1000ps shown by two peaks. In both cases, the number of O FPs again level off to an equilibrium value. Evolved system at 1000ps was also separately equilibrated for 500ps. This evolution is shown with black triangles. Each case leads to almost the same number of O FPs at t=1500ps.

The aim is to understand the O FPs evolution in a disproportionately defected system, i.e., the evolution of a system with a large number of O FPs in the presence of a low concentration of U FPs. To do this, 200 O FPs and only 50 U FPs are created. The evolution of the O FPs with time is shown in Figure 8-11. At 200 ps there is a significant

decrease in the number of O FPs, which then levels off by about 500ps suggesting a certain concentration level of O FPs for U FPs. The system is perturbed with the hope of stimulating further interactions by creating a further 200 O FPs, as evidenced by the first peak in the plot. The system again equilibrates for another 500 ps. Most of the O FPs again recombine and annihilate leaving behind almost the same number of O FPs as were observed after first 500 ps. This shows that the additional 200 O FPs did not substantially disturb the evolution of the defects in the system and the O FPs concentration determined by the concentration of U FPs.

At this point (1000 ps), two different simulations on the equilibrated system are performed. In the first, yet another 200 O FPs to the system are added again. In the second, the 1000 ps system is simply allowed to equilibrate independently without any addition of O FPs (evolution shown by black triangles). After an additional 500ps, the two systems have almost identical numbers of O FPs. Thus, it illustrates that even a frequent addition of the O FPs does not alter the final evolution of the system to a fixed concentration. Hence, it is concluded that the equilibrated O FPs concentration depends entirely on the U FPs concentration in the system. To confirm this conclusion further, six different simulations are performed with systems initially containing 100 O FPs but varying number of U FPs, i.e., 5, 10, 20, 30, 50 and 70. Figure 8-12 gives the time dependence of the number of O FPs for each system. In Figure 8-12, as the initial U FPs concentration is increased, the number of surviving O FPs also increases. For illustration, the systems containing 5 and 70 U FPs are compared. At $t = 0$ ps, both the systems contain 100 O FPs. However, with time, the number of O FPs differs significantly between two systems. For the system containing 5 U FPs, the O FPs number drops to 38

by $t = 100$ ps and then to 25 at $t = 400$ ps. Due to a very low concentration of U FPs in this system, most of the O vacancies and interstitials annihilate by recombination and only few are left behind. The number of O FPs levels off by $t = 400$ ps and the data points for 400ps and 500ps overlap illustrating that no further O FP recombination takes place.

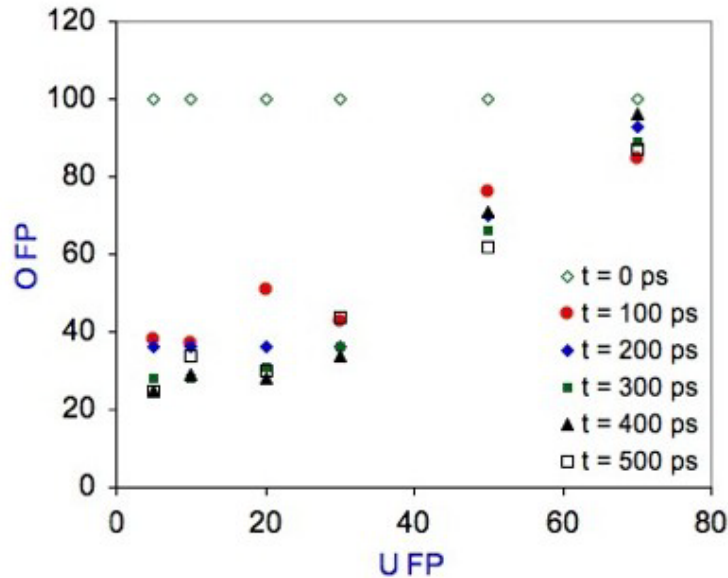


Figure 8-12. Number of O FPs (time progressing) as a function of number of initially created U FPs. Initially, 100 O FPs were created on each of six different systems containing 5, 10, 20, 30, 50 and 70 U FPs respectively. After every 100 ps time period, the number of O FPs are shown. There are higher number of O FPs alive after 500 ps in the system with initially higher U FPs. There are ~95 O FPs present in the system with initially 70 U FP (data on extreme right) in contrast to only ~30 O FPs in the system with 5 U FPs (data on extreme left).

The system with 70 U FPs displays a different evolution. In this case, first inspection shows that the data points for all six different time periods are concentrated very close to one another and near to the high end of the plot. This illustrates that not many recombination events take place. By $t = 100$ ps, only 15 O FPs have recombined and 85 survive. Even with further progressing time, the number of FPs does not decrease; rather there is an increase from 85 at $t = 100$ ps to 96 at $t = 400$ ps. Unlike the recombination

mechanism that was dominant in the 5 U FPs (low concentration) system, here the system forms *new* FPs. The O FPs in the high U FPs system evolve into clusters. This shows that an increasing concentration of U FPs tends to stabilize an increased concentration of O FPs in the system. Further, if the O FPs concentration is not sufficient for the given U FPs concentration, the system responds by creating new O FPs as also seen previously in Figure 8-5. The data for rest of the systems in Figure 8-12 also shows increased O FPs as the U FPs are increased.

8.3 Discussion

The simulation approach used here complements the conventional collision cascade simulations to provide a better understand the kinetic phase of defect evolution. An application of this method to radiation damage is previously presented in Chapter 7. Uberuaga *et al.*¹¹⁰ had used a combination of collision-cascade MD and TAD simulations to characterize the evolution of the point defects in MgO. The energy however, limited by the relatively small number of defects created in a single cascade, they could only observe very small clusters from multiple simulations. They found that the point defects left after the ballistic phase in the collision cascade evolved into interstitial clusters. On the other hand, this method allows to generate large concentration of the defects in a relatively smaller system. This method could not only reproduce their clusters but also observe much larger clusters. In addition, due to the formation of larger clusters, this methodology revealed the formation and growth mechanism of rocksalt clusters.

It is interesting to compare this UO₂ system with MgO. As in UO₂, in MgO it is observed that if the defects are present only on one sub-lattice, the FPs quickly recombine, whereas, they cluster if the defects are present on both sub-lattices. Further, not only is the defect evolution similar but in both case the clusters are also in part

stabilized by formation of new FPs. In UO_2 , it is seen that new FPs are formed only on O sub-lattice which stabilize the COT clusters. In MgO however, both Mg and O ions can displace from the lattice site to form new FPs. One difference arises from the difference in crystallography of the two systems. The interstitial lattice in MgO has the same structure of parent rocksalt crystal structure. Therefore, formation and growth of clusters is supported by new FPs that complete any missing interstitial in the $(\text{MgO})_4$ crystal structure. Since the crystal lattice and interstitial lattices have the same structures, the extent and shape of the defect cluster is not limited. By contrast, the lattice of interstitial sites in UO_2 does not have the symmetry of the parent lattice. As a result, the defect clusters have a defined extent and shape: a COT within a single unit cell. The MgO interstitial clusters have been found to be highly stable¹¹⁰ even on experimental time scale; the stability of UO_2 clusters beyond MD time scale is yet to be established.

It is well known that the experimentally observed COT clusters are found in oxygen-rich UO_2 . It was shown by Murray *et al.*¹³⁸ that the extra oxygen ions form COT clusters in systems with O-U ratio greater than 2.13. The observation of COT clusters in stoichiometric UO_2 with no extra O interstitials is rather unexpected. From the results, it is believed that it must be due to the high concentration of the interstitials in the system that act as extra O atoms. The hypothesis is supported by simulations on an only-interstitial system (Figure 8-9). However, the absence of clustering in the “only O FPs” environment illustrates that charge imbalance on the U sub-lattice is also very important. From analysis of all the simulations above, a clear picture emerges that the defects on the U sub-lattice are primarily responsible for the radiation intolerance of the UO_2 .

Anderson *et al.*¹⁴⁰ have recently used DFT calculations to predict that split-quad interstitials are the most stable O interstitial configurations in the hyperstoichiometric systems, followed by COT clusters. The least stable are the individual interstitials at the octahedral site. The split-quad interstitials are not observed in these simulations. This disagreement could be due to a lack of materials fidelity in the empirical potential and could be due to the effects of temperature: the DFT calculations were performed at 0 K whereas the MD simulations are performed at very high temperatures.

An atomistic simulation is only as good as the potential that describes the interatomic interactions. The Basak potential used for these simulations has non-formal charges lower than the nominal valences of the ions. This introduces a degree of covalency to the system. By contrast, the Busker potential uses strictly formal charge model (i.e., U^{4+} and O^{2-}). Corresponding simulations of FP evolution do not show the COT cluster formation. Further, with the Busker potential a pre-assembled COT cluster quickly disintegrates. Why do these potentials give such different results and which is more physically reasonable? The difference clearly arises from the difference in charges. In particular, the electrostatic repulsion among the like-charged interstitials is much higher for formal charges (Busker) than for partial charges (Basak). That both DFT calculations and experiment have shown the presence of COTs strongly suggests that, a non-formal charge model might be a better choice to model the defect evolution more appropriately. This conclusion is also consistent with the conclusion of Govers *et al.*¹⁴¹ that partial charge models for UO_2 generally provide higher materials fidelity than formal charge models.

Finally, this study has been performed on single crystal elucidating the underlying atomic-interaction mechanisms. A corresponding study in the polycrystalline UO_2 is required to elucidate the point-defect evolution in the presence of the grain boundaries (GBs). In the polycrystalline system, not only will the point defects annihilate by vacancy-interstitial recombination mechanism but may also be eliminated at the GBs. In that case, cluster formation might be impeded. An understanding of GB sink/source strength therefore needs to be established to understand the effect of GBs on defect evolution.

CHAPTER 9 EVOLUTION OF POINT DEFECTS IN BCC MOLYBDENUM¹

9.1 Introduction

The nucleation, annihilation, diffusion, segregation and clustering of vacancy and self-interstitial point defects in polycrystalline solids is of fundamental importance to many materials-science processes, such as compact sintering for microstructure development,¹⁴² irradiation damage in fuel and cladding components in nuclear systems,^{143,144} and electromigration in electronic interconnects,¹⁴⁵ to name just a few. As is well known, the equilibrium concentration and mobility of a particular type of point defect at any given temperature is determined by its formation and migration energies. However, under non-equilibrium conditions, the kinetic evolution of point-defect populations is driven by the competition between point-defect production and annihilation at internal sinks or sources (such as grain boundaries (GBs), voids or dislocation cores) and/or external surfaces.

Metals are widely used as structural materials inside nuclear reactors. Under these extreme conditions, they undergo damage due to irradiation. While damage due to irradiation in the bulk has been understood very well,^{121,146,147} with some relation to grain boundaries (GBs),¹⁴⁸ much work needs to be done to understand the behavior of grain-boundaries (GBs) from their source and sink strength viewpoint. The GBs are known to act as sources and sinks for defects. However, their response under extreme conditions is not clear. For example, under normal radiation events, GBs while acting as sources can emit interstitials to equilibrate high concentration of vacancies created in the grain. However, under extreme conditions, i.e., under high damage due to multiple radiation events at high temperature, GBs will also need to respond at the same rate by emitting

¹In this chapter, all work was done in collaboration with Dr. Paul Millet at Idaho National Laboratory apart from Figures 9-3, 9-4 and part of 9-5, which are sole works of Dr. Millett. The nanocrystalline structures were also prepared by Dr. Millett.

very high concentration of interstitials. However, intuitively, it occurs, that there must be a limit to which GBs can respond. This argument is also applicable to GBs while acting as sinks. Hence, a foremost question is: *Do GBs saturate?* In this work, a foundation is laid to elucidate the phenomenon by modeling a very simple crystal system, bcc Molybdenum. Damage due to radiation is modeled by using same methodology as described in Chapter 7.

Here the results of molecular-dynamics (MD) simulations are shown that focus on the dynamic nucleation and annihilation of both vacancies and interstitials at GB interfaces in nanocrystalline structures. The GB source and sink strength for vacancies as well as the sink strength for interstitials is extracted. The structures are initialized to be either over- or under-saturated with respect to one particular point-defect specie (either vacancy or interstitial). Upon annealing at high temperatures, these point defects then migrate throughout the lattice and annihilate at GB sinks (or nucleate from GB sources), thus allowing the characterization of the time-evolution of the system to equilibrium. Over-saturated point-defect systems can equilibrate by two mechanisms: (a) mutual vacancy-interstitial recombination, and (b) elimination at GBs. The source/sink strength of GBs for vacancies and interstitials allows establishing the governing point-defect equilibration mechanism out of the two. Furthermore, the use of fully-deterministic MD simulation in this work, as opposed to commonly-used kinetic Monte-Carlo models which use a rigid lattice,¹⁴⁹ is a further step towards a more realistic characterization of source/sink mechanisms.

9.2 Simulation Methodology

In the present work, high-temperature atomistic simulations are performed on nanocrystalline structures of body-centered-cubic (bcc) Mo in order to investigate the

grain-boundary source/sink strengths and diffusion kinetics of point defects at nanoscale dimensions. The three-dimensional (3D) periodic simulation cell contains six hexagonally-shaped, columnar grains of identical diameter ($d = 20$ nm) with a [100] columnar axis. The individual orientations of the grains in the global coordinate system are assigned to produce only high-energy, asymmetric tilt GBs, each with a misorientation angle of 30° . The structure of these GBs is continuously disordered along the interfacial plane. Further details on this nanocrystalline structure can be found elsewhere.¹⁵⁰ The zero-temperature MD input structures are heated up to the desired temperature in a step-wise fashion and all simulations are performed in the *isothermal-isobaric* ensemble.

The Finnis-Sinclair (FS) potential¹⁵¹ for bcc-Mo is used throughout the study. The parameters that are of particular interest for diffusion, the zero-temperature relaxed vacancy-formation energy (E_v^f) and the vacancy migration energy (E_v^m), have been previously calculated as 2.54 eV and 1.32 eV,¹⁵² respectively. These are slightly below the experimental values of 3.0 ± 0.2 eV and 1.5 ± 0.2 eV.¹⁵³ The thermodynamic melting temperature for this potential is found to be $T_m = 3097 \pm 10$ K¹⁵⁰ using the solid-liquid interface velocity method.¹⁵⁴ The highest annealing temperature chosen in this study is 2900 K, at which it was verified that GB pre-melting does not occur.

9.3 Vacancy and Interstitial Diffusivities

Before considering nanocrystalline microstructures, the diffusivities of both vacancies and interstitials in the perfect crystal are determined. Single-crystal structures with $40 \times 40 \times 40$ unit-cell dimensions (128,000 atoms) and 3D periodic boundary conditions are isothermally annealed at temperatures ranging between 2500 K and 2900

K. To determine the point-defect diffusivities, 20 vacancies or interstitials into the simulation cell are inserted and their self-diffusion is followed. A vacancy is created by randomly removing an atom from a regular lattice site, and, conversely, a self-interstitial is created by adding an atom to an interstitial site. It is furthermore ensure that, initially, every point defect is separated by a distance of at least $3a_0$ from any other point defect.

The self-diffusivity of the *atoms*, D_A , is determined from mean-squared-displacement (MSD) calculations under zero-stress conditions using the Equation 2-19. From this, the vacancy diffusivity (D_v) and interstitial diffusivity (D_i) can be obtained using the Equations 2-20 and 2-21. In Equations 2-20 and 2-21, f_v and f_i are correlation factors with values of 0.732^{155} and 0.300^{156} respectively. For the 20 point defects present in each simulation, the concentrations of $c_v = c_i = 20/128,000 = 1.56 \times 10^{-4}$.

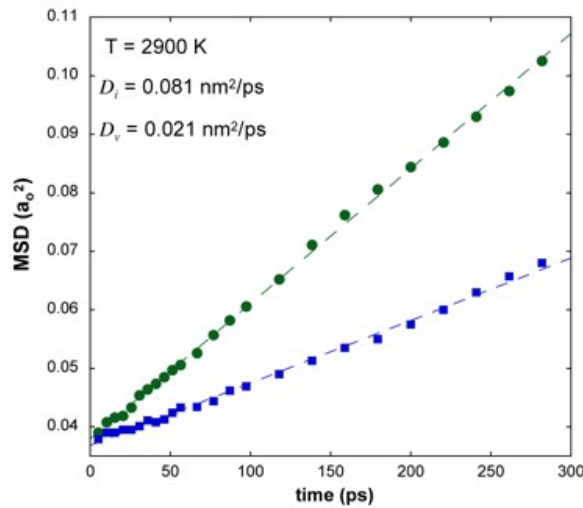


Figure 9-1. Mean-squared displacement for single-crystal structures ($40 \times 40 \times 40 a_0$) containing either 20 vacancies (blue squares) or 20 self-interstitials (green circles) at $T = 2900$ K. The vacancy and interstitial diffusivities are calculated to be $0.021 \text{ nm}^2/\text{ps}$ and $0.081 \text{ nm}^2/\text{ps}$, respectively.

The MSD data for both structures is plotted in Figure 9-1 for $T = 2900$ K. The least-squares fits to the data give vacancy and interstitial diffusivities of $0.021 \text{ nm}^2/\text{ps}$ and

0.081 nm²/ps, respectively (2.1×10^{-8} and 8.1×10^{-8} m²/s). The diffusivities at each temperature are then plotted on an Arrhenius diagram for interstitials and vacancies (Figure 9-2), revealing activation energies of $E_i^m = 0.49$ eV and $E_v^m = 1.06$ eV. The migration energy obtained for vacancy diffusion is somewhat lower than the value of 1.32 eV determined from the zero-temperature calculations;¹⁵² this can perhaps be attributed to the thermal expansion of the lattice.

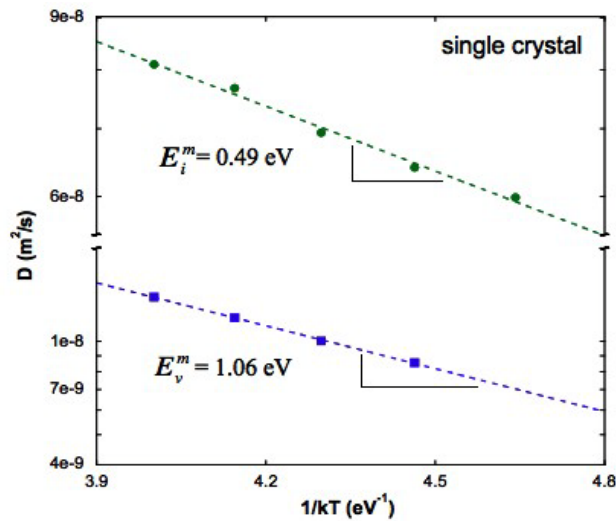


Figure 9-2. Arrhenius plot for D_i and D_v in the temperature range between $2500 \text{ K} \leq T \leq 2900 \text{ K}$. The activation energies for interstitial and vacancy migration are found to be 0.49 eV and 1.06 eV, respectively.

9.4 Grain Boundaries as Sources and Sinks

9.4.1 Grain Boundaries as Vacancy Sources

In order to investigate the GB source strength for vacancy emission, the nanocrystalline structures are initialized to be clearly under-saturated, with a vacancy concentration of $c_v^o = 0$, with respect to the thermal-equilibrium value. This is achieved by equilibrating the GB structures at $T = 2400 \text{ K}$ (where GB diffusion is activated, however vacancy nucleation is not), and instantaneously stepping up the temperature to T

= 2900 K. To investigate the vacancy nucleation and diffusion, the sample is then annealed at 2900 K for approximately 1 ns, while the vacancy distributions are monitored at various times throughout the simulations.

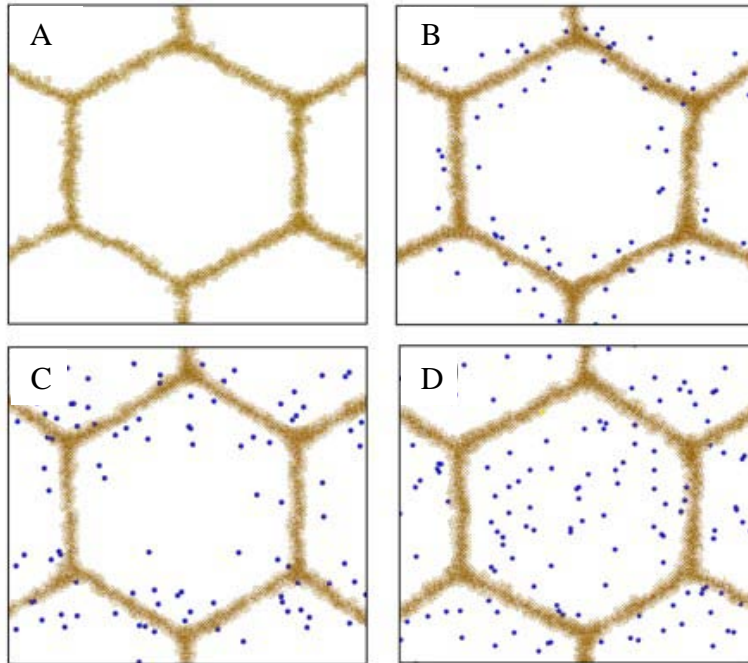


Figure 9-3. Progressive snapshots of the vacancy population within a single $d = 20$ nm grain at $T = 2900$ K for increasing time: A) $t = 0$ ps, B) $t = 72$ ps, C) $t = 205$ ps, and D) $t = 1005$ ps. The microstructure is viewed along the [100] columnar axis. The concentration of vacancies, identified by blue dots, increases with time due to the on-going nucleation from GB (brown atoms) sources. The time-evolution of the vacancy concentration, as quantified in the lower curve of Figure 9-5, follows an exponential approach to the equilibrium concentration of $\sim 10^{-3}$.

Figure 9-3 shows progressive snapshots in time of the vacancy population within a single grain interior of the under-saturated structure. GB regions are visualized by the use of the common-neighbor analysis,¹⁵⁷ which identifies atoms in non-bcc crystalline environments (light brown dots). In addition, vacancies (represented by blue dots) are detected by determining lattice sites within the grain interiors that are not occupied by an atom. The viewing direction is along the columnar [100] axis. Initially, at $t = 0$ ps

(Figure 9-3(a)), there are no vacancies. After 72 ps of annealing (Figure 9-3(b)), several vacancies have nucleated from the GBs, but have yet to diffuse extensively toward the grain centers. The vacancy concentration, at this time, has increased to $c_v = 2.9 \times 10^{-4}$. As time continues (Figure 9-3(c), $t = 205$ ps), the vacancy concentration increases to $c_v = 4.9 \times 10^{-4}$, and the vacancies have migrated further into the bulk. Finally, at time $t = 1005$ ps (Figure 9-3(d)), vacancies appear to be essentially evenly distributed throughout the microstructure with an increase in the concentration to $c_v = 9.3 \times 10^{-4}$.

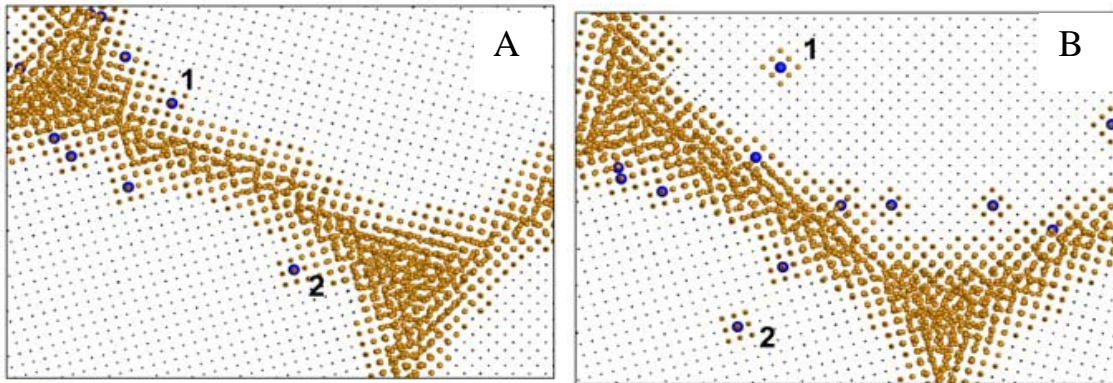


Figure 9-4. Close-up views of the nucleation of two lattice vacancies from a high-energy GB taken at A) $t = 60$ ps and B) $t = 70$ ps. The vacancies labeled '1' and '2' have nucleated from the GB and have migrated towards the interiors of the grains they inhabit. In the latter snapshot, several new vacancies have been nucleated and still reside near the GBs.

The emission of a vacancy from a GB source is a thermally-activated process with a pre-exponential term that is associated with an attempt frequency.¹⁵⁸ Therefore, a GB may produce many vacancies that reabsorb at their nucleation sites before a successful emission occurs in which a vacancy adequately distances itself into the lattice (similar to the creation of a stable Frenkel pair). Figure 9-4 provides a close-up view of the successful emission of two vacancies during a 10 ps time interval, demonstrating that the GBs do indeed serve as sources for the increasing vacancy populations within the

nanocrystalline grains. Throughout the simulation, it is observed that many short-lived vacancies directly adjacent to GBs (see Figure 9-4(b)) quickly annihilate back into the interface. A visual inspection reveals no qualitative change in GB structure or width throughout the simulation, suggesting that the source strength is constant and independent of past nucleation events.

9.4.2 Source-strength Analysis

The equilibration of the vacancy concentration in the grain interiors due to emission from GB interfaces is diffusion controlled. The most commonly used model for predicting the change in point-defect population due to microstructural source/sink mechanisms is the rate theory.¹⁴⁴ According to this model, the time evolution of vacancies and interstitials can be expressed as:

$$\frac{dc_v}{dt} = G - Rc_v c_i - k_v^2 D_v (c_v - c_v^{eq}) \quad (9-1)$$

$$\frac{dc_i}{dt} = G - Rc_v c_i - k_i^2 D_i c_i \quad (9-2)$$

According to Equations 9-1 and 9-2, the concentration rate of vacancies or interstitials depends on their production rate, G , the mutual recombination rate, R , and the microstructural source/sink strength, k^2 . c_v and c_i represent the concentration of vacancies and interstitials respectively, and D_v and D_i represent vacancy and interstitial diffusivities respectively. In material systems, certain equilibrium defect concentration lowers the free energy of the system by balancing the entropy components (Equation 2-13). In equation 9-1, c_v^{eq} , represents equilibrium concentration of vacancies. The equilibrium concentration of interstitials is generally very low and can be neglected.

In the absence of self-interstitials, and hence vacancy-interstitial recombination, the time evolution of the vacancy concentration is given by:

$$\frac{dc_v}{dt} = -k_v^2 D_v (c_v - c_v^{eq}) \quad (9-3)$$

In this continuum model, k_v^2 is assumed to be: (i) a weighted sum of the sink strengths for each microstructural element (GBs, dislocations, voids), and (ii) spatially-averaged over the entire material. In the work, GBs are the only sources in the simulation cell.

Integrating Equation 9-3 and re-arranging leads to

$$c_v(t) = c_v^{eq} + (c_v^o - c_v^{eq}) \exp(-k_v^2 D_v t) \quad (9-4)$$

where, c_v^o is the initial vacancy concentration. k_v^2 is a geometrical parameter related to the average grain size (or, inversely, the density of GBs) with units of $1/\text{length}^2$.¹⁵⁹ One can therefore also obtain the equilibration time, or the characteristic time for the system to evolve from c_v^o to c_v^{eq} , as $\tau = 1/k_v^2 D_v$.

To quantify the evolution of c_v in the system, the total number of vacancies in each grain is counted and divided by the number of lattice atoms in that grain. To reduce statistical noise, these values are ensemble-averaged over all six constituent grains in the simulation cell (the error bars represent deviations in these data sets). The concentrations for both the under- and over-saturated nanocrystals are plotted vs. time in Figure 9-5, revealing an asymptotic approach to $c_v^{eq} = (1.0 \pm 0.1) \times 10^{-3}$. Regardless of the initial concentration, the vacancy distribution in the bulk regions thus approaches its equilibrium value within about a nanosecond. Furthermore, it is pointed out that the equilibrium value is in qualitative agreement with the experimentally-measured vacancy

concentrations in most bcc and fcc metals of $10^{-4} < c_v^{eq} < 10^{-3}$ just below the melting temperature.¹⁶⁰

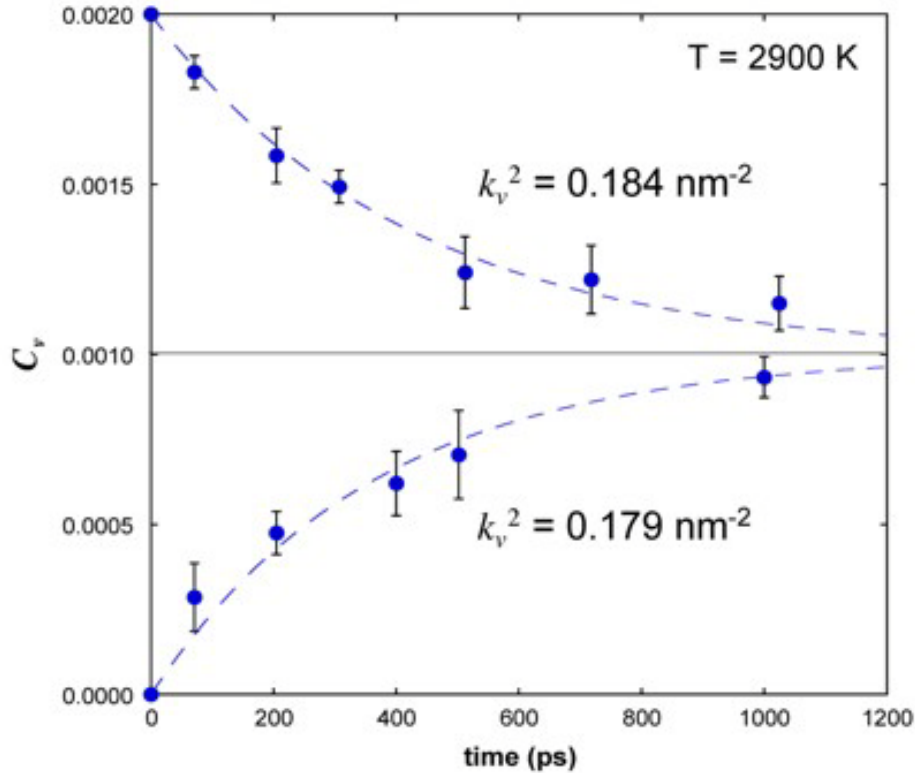


Figure 9-5. Evolution of the vacancy concentration in the under- and over-saturated nanocrystalline structures at $T = 2900$ K (see Figures 9-3 and 9-6). In both cases c_v evolves exponentially towards the equilibrium concentration of $c_v^{eq} = (1 \pm 0.1) \times 10^{-3}$. The dashed lines represent fits to Equation 9-4, yielding the GB sink and source strengths of $k_v^2 = 0.184 \text{ nm}^{-2}$ and $k_v^2 = 0.179 \text{ nm}^{-2}$, respectively.

The approach to equilibrium is found to be exponential, as evidenced by the fits of Equation 9-4 to the data, represented by the dashed lines. Inserting the value of $D_v = 0.021 \text{ nm}^2/\text{ps}$ (see Figure 9-1) yields a GB source strength of $k_v^2 = 0.179 \text{ nm}^{-2}$. In addition, the characteristic equilibration time is found to be $\tau = 1/(k_v^2 D_v) = 266 \text{ ps}$. It is found that this time corresponds to the instant at which c_v has increased to 63% of the difference between c_v^{eq} and c_v^o (obtained from Equation 9-4) for $t = \tau$.

9.4.3 Grain Boundaries as Vacancy Sinks

Grain boundaries, in addition to being vacancy sources, can also operate as sinks for both vacancies and self-interstitials. This is most relevant for particle irradiation in nuclear materials, in which displacement cascades continuously produce excess concentrations of Frenkel pairs. Following a cascade, these defects will either cluster to form voids and interstitial loops or annihilate by mutual vacancy-interstitial recombination or be eliminated at microstructural sinks (including dislocations, GBs, or free surfaces).

In order to quantify the GB sink strength for vacancy defects, a high-temperature anneal (at $T = 2900$ K) of the same nanocrystalline microstructure is performed, however, with an initial *super-saturation* of vacancies created by randomly inserting an initial concentration of $c_v^o = 2.0 \times 10^{-3}$ (i.e., $2c_v^{eq}$) into the grain interiors.

Figure 9-6 shows progressive snapshots of the super-saturated microstructure (see also Figure 9-3). The initial structure (at $t = 0$ ps) in Figure 9-6 (a) contains a concentration of $c_v^o = 2.0 \times 10^{-3}$. As the annealing proceeds to $t = 72$ ps (Figure 9-6 (b)), $t = 205$ ps (Figure 9-6 (c)), and finally $t = 1025$ ps (Figure 9-6 (d)), the concentrations decrease to $c_v = 1.8 \times 10^{-3}$, 1.6×10^{-3} , and 1.2×10^{-3} , respectively. In the absence of any interstitials in the system, this decrease in vacancy concentration is solely due to annihilation at the GB sinks. The corresponding vacancy concentrations vs. time are shown in the upper half of Figure 9-5, revealing again an exponential approach to equilibrium (dashed line; see Equation 9-4). Remarkably, the evolution of the over-saturated system is practically indistinguishable from that of the under-saturated system, albeit in an inverted manner. The equilibrium concentration and sink strength are found

to be $c_v^{eq} = (1 \pm 0.1) \times 10^{-3}$ and $k_v^2 = 0.184 \text{ nm}^{-2}$, which are nearly identical to the undersaturated values. The equilibration time for this system is therefore $\tau = 1/(k_v^2 D_v) = 259 \text{ ps}$ (compared to 266 ps for the undersaturated system).

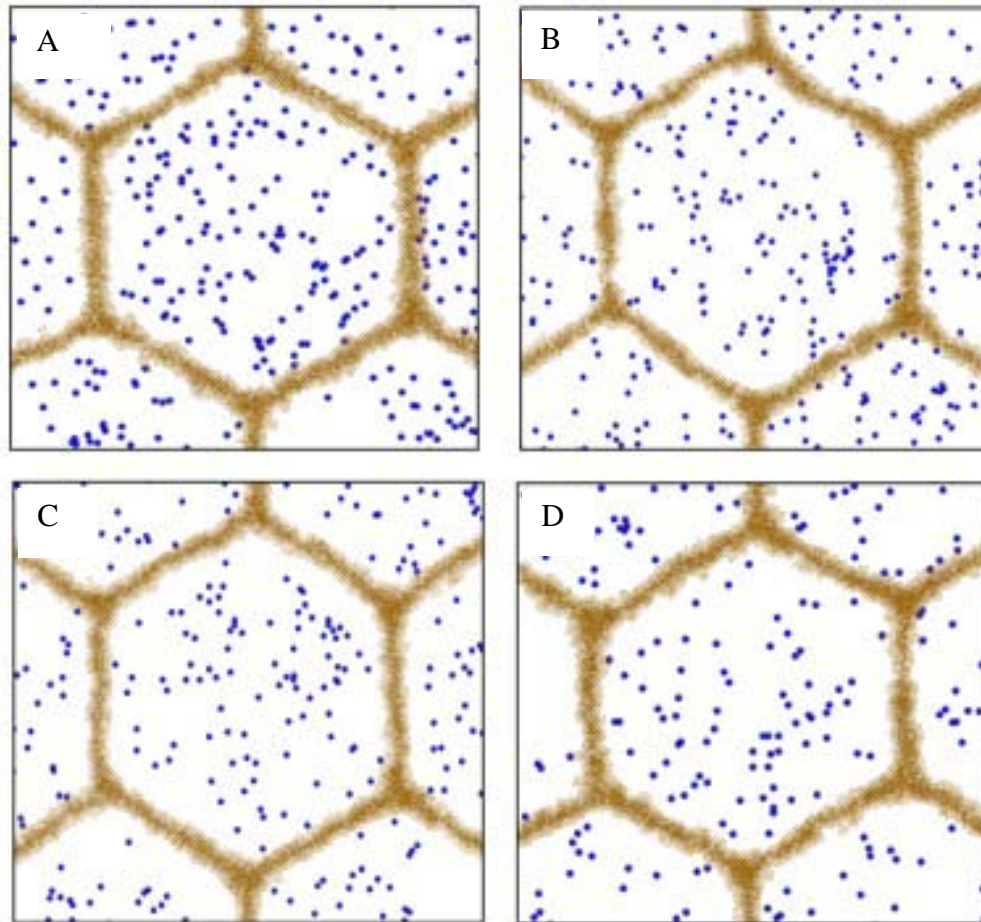


Figure 9-6. Progressive snapshots of the vacancy population in a single grain of the oversaturated sample taken at A) $t = 0 \text{ ps}$, B) $t = 72 \text{ ps}$, C) $t = 205 \text{ ps}$, and D) $t = 1025 \text{ ps}$ (see also Figure 9-3). The initial vacancy concentration is twice that at equilibrium. The evolution is quantified in the upper curve of Figure 9-5.

The good correspondence between the values of GB source and sink strengths suggests that the GBs are equally efficient at nucleating and annihilating vacancies, and that the equilibration process is diffusion-controlled.

9.4.4 Grain Boundaries as Interstitial Sinks

Similar to the above vacancy simulations, the GB sink strength of interstitials is elucidated by annealing a super-saturated interstitial system at $T = 2400$ K. This lower temperature is chosen due to the fact that at 2900 K, vacancies nucleate from the GBs at an appreciable rate (see Figure 9-3) and recombine with the initially-inserted interstitials, thus interfering with the GB sink-strength determination.

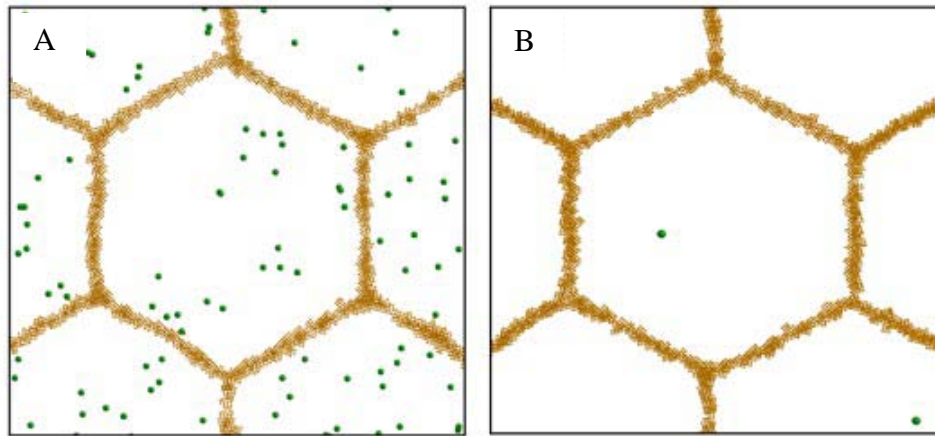


Figure 9-7. Progressive snapshots of the oversaturated interstitial distribution within the $d = 20$ nm nanocrystalline structure. The sample was annealed at the lower temperature of $T = 2400$ K to avoid the GB nucleation of vacancies (that would interfere with the evolution of the interstitials). The snapshots were taken at A) $t = 0$ ps where $c_i = 4.4 \times 10^{-4}$ and B) $t = 779$ ps where $c_i = 1.1 \times 10^{-5}$ and only a couple of interstitials remain in the grain interiors.

At this lower temperature, vacancy nucleation is suppressed, at least for a short time ($t < 800$ ps) while interstitial diffusion dominates, thus allowing a determination of k_i^2 . Figure 9-7(a) shows the nanocrystalline structure prior to the simulation, containing an initial interstitial concentration of $c_i^o = 4.4 \times 10^{-4}$. After 779 ps of annealing (Figure 9-7(b)) only a couple of interstitials remain in the grain interiors, corresponding to a concentration of $c_i \sim 10^{-5}$. The corresponding rate equation for the time evolution of

interstitial concentration in a material with microstructural sources and sinks is generally given as¹⁴⁴

$$\frac{dc_i}{dt} = -k_i^2 D_i c_i \quad (9-5)$$

Due to high formation energy, the equilibrium self-interstitial concentration in metals is typically very low, even at high temperatures, and therefore is neglected (compare Equation 9-5 with Equation 9-3).

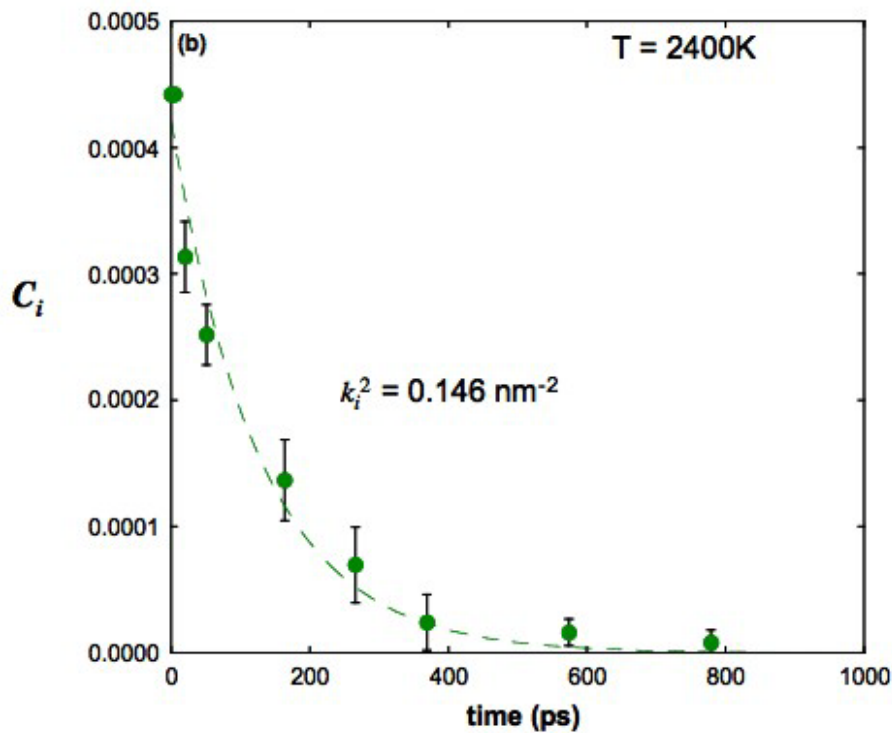


Figure 9-8. Quantification of the time evolution of the self-interstitial concentration, c_i , at $T = 2400$ K (see Figure 9-7). The dashed line represents a least-squares fit to Equation 9-6, yielding a GB sink strength for self-interstitials of $k_i^2 = 0.146$ nm^{-2} .

Consistent with this, no measurable equilibrium concentration in the simulations is observed (the final structure contains only a couple of interstitials among the six grains, which may still be too many). The time-dependent concentration is obtained by integrating Equation 9-5 to produce

$$c_i(t) = c_i^o \exp(-k_i^2 D_i t) \quad (9-6)$$

As expected, this relation is similar to the vacancy evolution governed by Equation 9-4. Figure 9-8 shows this exponential approach of c_i to zero. Fitting to Equation 9-6 (dashed line) yields the GB sink strength for interstitials as $k_i^2 = 0.146 \text{ nm}^{-2}$.

The equilibration time for this simulation is therefore $\tau = 1/(k_i^2 D_i) = 127 \text{ ps}$, using an interstitial diffusivity of $D_i = 0.054 \text{ nm}^2/\text{ps}$ (extrapolated from Figure 9-2(a)). Thus, the GB source strength for vacancies ($k_v^2 = 0.179 \text{ nm}^{-2}$), the GB sink strength for vacancies ($k_v^2 = 0.184 \text{ nm}^{-2}$), and the GB sink strength for interstitials ($k_i^2 = 0.146 \text{ nm}^{-2}$) are all relatively similar.

9.4.5 Discussion on GB Source/Sink Strength

The vacancy and interstitial concentrations given in Equations 9-3 and 9-5, and those presented in the results above, are spatially averaged over the entire grain interiors (i.e., they do not capture spatial gradients within the grain interiors). As a result, the GB source/sink strengths for vacancies (k_v^2) and interstitials (k_i^2) are simply geometrical constants that only depend on the grain size and distribution. Brailsford and Bullough¹⁵⁹ determined an analytical solution for these source/sink strengths by assuming a periodic array of grains (similar to the microstructures considered here). For the regions between the GBs, Fick's law was solved subject to the boundary condition that $c_v = c_v^{eq}$ at the GBs, and the vacancy concentration was spatially-averaged over the domain throughout time. Their solution for GB source/sink strength is

$$k_v^2 = k_i^2 = \frac{15}{r_g^2} \quad (9-7)$$

where, $r_g = d/2$ is the grain radius. For $d = 20 \text{ nm}$, this yields $k_v^2 = k_i^2 = 0.15 \text{ nm}^{-2}$. This

value lies between the GB strength for vacancies ($k_v^2 = 0.184 \text{ nm}^{-2}$ for sinks, and $k_v^2 = 0.179 \text{ nm}^{-2}$ for sources) and that for interstitials ($k_i^2 = 0.146 \text{ nm}^{-2}$).

9.5 Frenkel-pair Annihilation

Until now, the source/sink strength of GBs for either point defects is elucidated (in the absence of another) using the third term in Equation 9-1 (or 9-2). The attention is now turned to the annihilation mechanisms in the simultaneous presence of both vacancies and interstitials. In Equation 9-1 (and 9-2), while the first term, the defect generation term, is constant throughout the simulations, the second term representing the annihilation by mutual recombination mechanism and the third term representing the annihilation at GBs are changing constantly. In this section, the effect of the last two terms is disentangled and the governing point-defect annihilation mechanism is determined.

9.5.1 FP Annihilation by Mutual Recombination

The second term in Equation 9-1 depends on the concentration of point defects and the mutual recombination rate, R . To extract R , single-crystal simulation is adopted in which 50 FPs are randomly created and their evolution is followed. Since the concentration of vacancies and interstitials, at any point of time is same, it can be assumed that:

$$\frac{dc_{FP}}{dt} = \frac{dc_i}{dt} = \frac{dc_v}{dt} = -Rc_i c_v = -Rc_v^2 \quad (9-8)$$

Time progressing snapshots of the structures at, $t = 20 \text{ ps}$ and $t = 307 \text{ ps}$ are shown in Figures 9-9(a) and 9-9(b) respectively. At any instant, an approaching vacancy and interstitial can recombine and annihilate. Since there are no other sinks in a single crystal, the elimination is only by pure recombination. A time-dependent mutual recombination profile of FPs is shown in Figure 9-10. The analytical solution of the equation is a power

law represented by $c_v = 1/[R(t) + 1/c_v^o]$ where c_v^o is the initial concentration of the vacancies (or FPs). Fitting with least-square method yields the recombination rate (R) as 42.58 ps^{-1} .

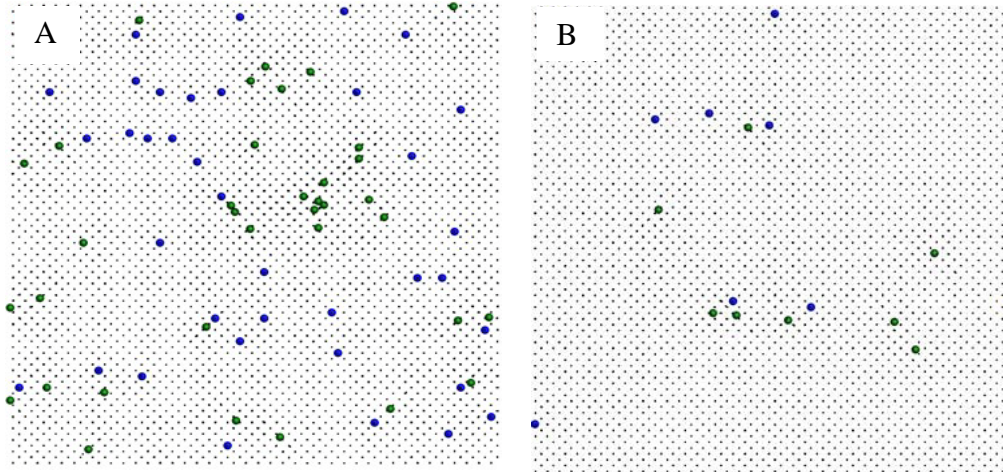


Figure 9-9. Frenkel pair distribution in a single crystal at two different MD times, A) $t = 20 \text{ ps}$ and B) $t = 307 \text{ ps}$. 50 FPs were randomly-distributed throughout the system separated by a minimum recombination radius of $2.0a_o$.

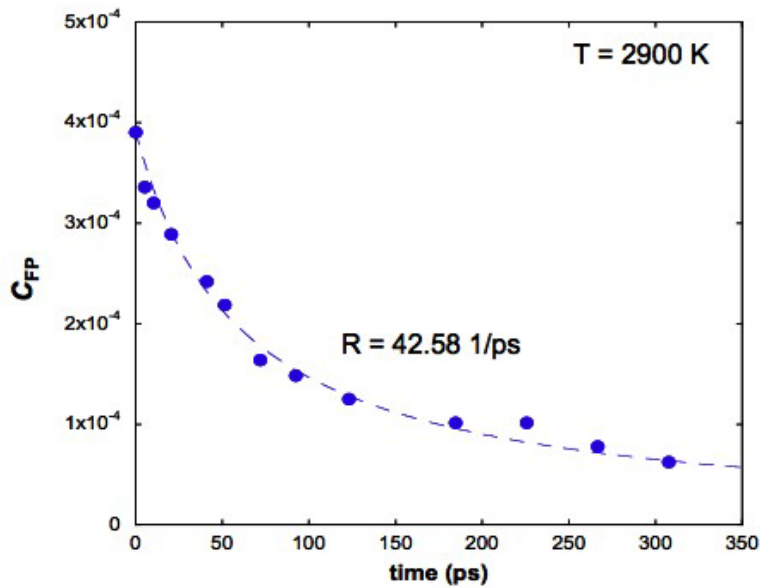


Figure 9-10. Frenkel pair concentration vs time for the structure shown in Figure 9-9 representing the FPs' recombination rate (R) in a single crystal. From the least-squares fit to Equation 9-8, R is found to be 42.58 1/ps .

The recombination rate can also be related to the diffusion coefficient of the species by a simple relationship:¹⁶¹

$$R = \frac{4\pi r(D_v + D_i)}{\Omega} \quad (9-19)$$

where, r is the recombination radius (it is the radius within which interstitials and vacancies can recombine spontaneously) and Ω is the atomic volume. By inserting corresponding values, the recombination rate of vacancies and interstitials obtained from Equation 9-9 is 41.61 ps^{-1} . This is in very good agreement with that obtained from the simulations ($R = 42.58 \text{ ps}^{-1}$, Figure 9-10). The recombination radius, r , can be backed out from Equation 9-9 by inserting $R (= 42.58 \text{ ps}^{-1})$. Thus, a theoretically obtained value of recombination radius, r , is $1.65 a_0$ which is also a very reasonable value for crystalline systems.

9.5.2 Frenkel Pair Annihilation in a Nanocrystalline Structure

Recapitulating the results, the source/sink strength of the GBs is calculated by elucidating the individual effect of third term in Equation 9-1. In this calculation, the second term is disregarded by allowing no recombination events. In the previous section, only the second term was focused by allowing recombination events in the absence of GBs. In this section, all processes are allowed to occur simultaneously, i.e., by inserting both vacancies and interstitials in the GBs structures. High concentration of point defects evolves to an equilibrium concentration by both mechanisms i.e., vacancy-interstitial mutual recombination and elimination at the GBs represented by second and third terms respectively. The individually obtained results from previous calculations will help in disentangling these two mechanisms when they occur simultaneously, thereby determining the dominant mechanism of point-defect annihilation.

This simulation is started with a nanocrystalline GB equilibrated structure (Figure 9-6(d)). To allow both mechanisms to occur simultaneously, FPs of concentration, $c_{FP} = 1.2 \times 10^{-3}$ are added on top of the initially present vacancies of concentration, $c_v = 1.2 \times 10^{-3}$. The evolution of the FPs at $T = 2900$ K is followed. Starting with a high concentration of FPs at $t = 0$ ps, shown in Figure 9-11 (a), the system evolves by FPs elimination as shown in Figure 9-11 (b). As expected, by $t = 922$ ps (Figure 9-11(b)), all the initially added FPs have eliminated and the system is left behind with the equilibrium concentration of vacancies.

As discussed above, the vacancies and interstitials would have eliminated by two mechanisms.

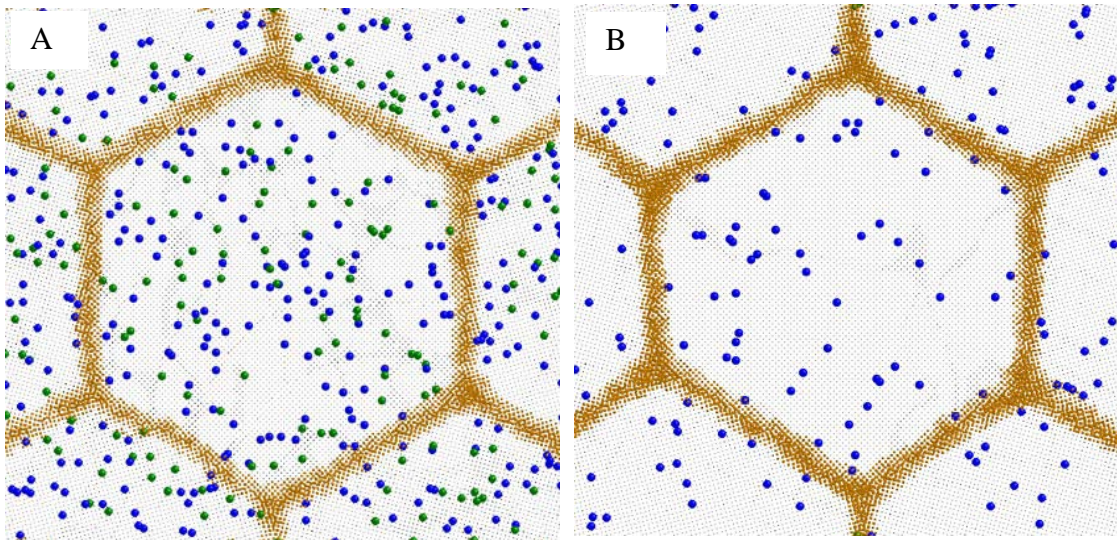


Figure 9-11. Evolving nanocrystalline structures over-saturated with the FPs. Initially, the system is annealed at 2900 K to allow equilibration of the vacancies. Then, FPs are randomly added by maintaining a recombination radius of $2.0 a_0$. A) At $t = 0$ ps, $c_{FP} = 1.2 \times 10^{-3}$, B) $t = 922$ ps, all FPs have recombined.

In order to determine the dominant mechanism, evolution of FPs in the single crystal to those in the nanocrystalline structures are compared. If the rate of elimination of FPs in

single crystal happened to be same as in GBs structure, it would illustrate that mutual recombination is the dominant mechanism.

Both systems are damaged with the same concentration of FPs. Figure 9-12 shows a comparison between the evolution of defects in two systems. Hollow circles represent data for the point defects in nanocrystalline structures, whereas, filled circles with dotted line represent data for the point defects in single crystal.

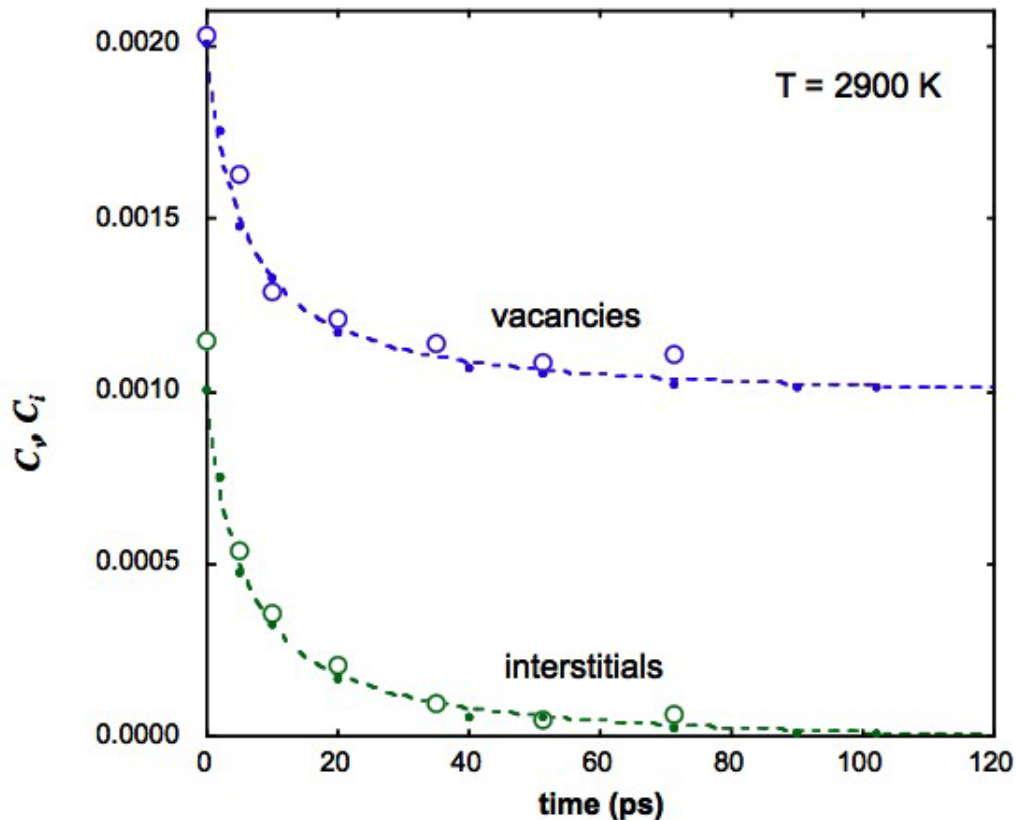


Figure 9-12. Comparison of the vacancy and interstitial concentrations throughout time for the nanocrystalline structure (hollow dots) and the single crystal (filled dots and dashed line). Initially, both the systems are equilibrated with the equilibrium concentration of the vacancies in addition to an excess concentration of FPs. As evidenced by the overlapping data sets, this plot illustrates that at this temperature and grain size, the effect of GB annihilation is negligible in comparison to FP recombination in the grain interiors.

The evolution of the vacancies (top curves) and the interstitials (bottom curve) is represented separately. The overlapping data for single crystal and nanocrystalline

structures for both vacancies and interstitials illustrates that the rate of elimination of both the vacancies and interstitials is same. This elucidates that in both systems, mutual point-defect annihilation mechanism is prevalent, and the point defects eliminate before reaching the GBs. In other words, GBs do not play significant role in the elimination of the point defects.

9.6 Conclusion

In conclusion, using MD simulations, the point-defect kinetics in model microstructures for nuclear metallic materials is elucidated. These simulations have illustrated that they are well-suited to determine the GB source/sink strengths for vacancies and interstitials in systems damaged due to irradiation. They represent a first step towards more refined simulations that can offer atomic-scale insight into the accumulation, evolution, and /or mitigation of irradiation-induced damage in nanostructured materials. By being able to capture atomistically, the formation of the vacancies at the GBs, the simulations have been able to disentangle the governing components in the rate-theory models and have elucidated the dominant point-defect elimination mechanism. At this temperature and grain size, the effect of GB annihilation is negligible in comparison to FP recombination in the grain interiors. An obvious next step will be to understand the effect of the grain size and temperature on the defect elimination process. A crossover between the mutual-recombination mechanism and GB elimination mechanism is expected. Other outstanding questions that can now be addressed include whether GB sinks can become exhausted after absorbing a high quantity of defects and the importance of defect fluxes in temperature gradients.

CHAPTER 10 SUMMARY AND FUTURE WORK

The evolution of point defects in fluorite-based materials, $\delta\text{-Bi}_2\text{O}_3$ and UO_2 , used in SOFCs and nuclear applications respectively has been elucidated. In addition, point-defect evolution in rocksalt MgO and the role of grain boundaries in BCC Mo was also illustrated.

10.1 $\delta\text{-Bi}_2\text{O}_3$

10.1.1 Cation Polarizability

In $\delta\text{-Bi}_2\text{O}_3$, the intrinsically present oxygen vacancies play significant role in oxygen diffusion. $\delta\text{-Bi}_2\text{O}_3$ has a high concentration of vacancies and has high ionic polarizability, which sustain its high oxygen diffusivity. When doped with cations that have radius and polarizability different from Bi, the diffusivity decreases. Experimentally, the effect of either is not clearly understood. Using MD simulations, it was found that ionic polarizability is key for high oxygen diffusivity and that the ionic radius does not have significant effect. Furthermore, it was found that the cation polarizability alone has an effect on oxygen diffusion; the oxygen polarizability does not effect diffusion. Moreover, a gradual increase in the cation polarizability increases oxygen diffusion. For a cation polarizability lower than a certain value, the vacancies order by aligning in combined $\langle 110 \rangle$ - $\langle 111 \rangle$ directions. Once this vacancy-ordered structure is formed, oxygen diffusion ceases. Hence, higher diffusivity can be achieved by using higher polarizable dopants.

10.1.2 Oxygen Diffusion Mechanism

In a unit cell of $\delta\text{-Bi}_2\text{O}_3$, there are multiple directions in which an oxygen atom can diffuse to occupy a vacant site. By following time-averaged path of oxygen atoms, in

agreement with experiments, it was found that oxygen diffusion preferentially occurs in $\langle 100 \rangle$ direction. However, in contrast to experiments that indicate oxygen passes through the empty octahedral site in the center of the unit cell, simulations showed that the oxygen follows predominantly a straight path. This apparent discrepancy could be due to different systems under study. While the experiments were performed on doped systems, simulations were performed on pure systems. A change in oxygen diffusion mechanism in the presence of polarizable ions might be expected.

10.1.3 Bonding

Using DFT calculations, it was found that Bi atoms surrounded by $\langle 111 \rangle$ -vacancy ordering have all six Bi-O bonds of same length, whereas, with those surrounded by $\langle 110 \rangle$ -vacancy ordering have three pairs of different bond lengths. In $\langle 111 \rangle$ -Bi, the electronic charge on the Bi is equally distributed among surrounding oxygen atoms and there is no preferential charge distribution. In contrast, $\langle 110 \rangle$ -Bi has different charge distribution among six surrounding oxygen atoms, revealed by different bond lengths. Furthermore, some of the $\langle 110 \rangle$ -Bi charge is also directed towards the vacancies: this is the $6s^2$ lone pair charge.

Different Bi-O bonds also have different bond strengths. $\langle 110 \rangle$ -Bi is predominantly ionic with valence charge of $2.84e$, whereas, $\langle 111 \rangle$ -Bi has a covalent valence charge of $2.12e$. It was speculated that this directional and difficult to break covalent bond could be the limiting factor in oxygen diffusion. Whether this bond could be tailored by adding different dopants to enhance oxygen diffusivity remains to be seen.

10.1.4 Crystallographic Analysis of Structure

Due to the ordering of vacancies and the structural distortion that it undergoes, a $1 \times 1 \times 1$ unit cell is no longer able to define the complete structure of δ -Bi₂O₃. This

structure has a lower symmetry than that of an ideal fluorite structure; the new space group is $Fm\bar{3}$ and the lattice parameter is 11.19761 Å, which is twice that of the original unit cell. The structure is highly distorted with displacements shown by both anions and cations. The anions are displaced by 0.4 Å in a direction close to but not exactly $\langle 110 \rangle$. Similarly, all $\langle 110 \rangle$ -Bi cations are displaced by 0.3036 Å in a direction opposite to the plane of the $\langle 110 \rangle$ oriented vacancies. However, due to symmetric orientation of vacancies in $\langle 111 \rangle$ direction, the $\langle 111 \rangle$ -Bi cations are not displaced.

10.2 MgO, UO₂ and Mo

10.2.1 Methodology

To understand a complete evolution of point defects that are accessible on experimental time scale, a new methodology was designed that focuses on the long-term kinetic evolution of the defects. While the conventional methodology focuses more on the point-defect creation during initial phase of radiation damage, i.e., ballistic phase, this new methodology focuses on defect annihilation during the kinetic phase. To illustrate the capability of new methodology, MgO was chosen as a model material. It was shown that this methodology reproduces interstitial clusters observed from combined conventional MD-TAD simulations, thus validating this methodology.

10.2.2 MgO Interstitial Clustering

It was found that if the FPs are present only on one sub-lattice, i.e., either Mg or O, the corresponding vacancies and interstitials recombine and annihilate. In contrast, if the FPs are present simultaneously on both sub-lattices, then instead of recombining, the interstitials segregate to form clusters. This provided a possible reasoning behind loss of radiation tolerance of MgO.

It was further found that the clusters maintain the crystal symmetry of the parent lattice, i.e., the interstitial clusters have rocksalt crystal structure. During the cluster growth, every alternating octahedral interstitial site is occupied by oppositely charged ion, forming a basic unit of $(\text{MgO})_4$. Furthermore, at any instance, if a basic unit lack an atom for completion, the lattice atoms respond by creating new FPs, thus stabilizing the cluster. Hence, it was found for the first time that there are two distinct diffusion mechanisms for cluster growth, (a) conventional atomistic diffusion involving aggregation, and, (b) formation of *new* structural FPs.

10.2.3 UO_2 Clustering

While in MgO, interstitials are the only species that are involved in the cluster formation, in UO_2 , both interstitials and vacancies form clusters. There are some characteristic similarities in clustering processes in UO_2 and MgO, despite the different crystal structures. Similar to MgO, in UO_2 , it was found that if FPs are present only on anion (O) sub-lattice, they recombined and annihilated. However, in contrast, if FPs are present only on cation (U) sub-lattice, unlike recombination in MgO, U FPs survive and nucleate new O FPs. The formation of new FPs was similar in MgO but the underlying mechanisms are completely different. In MgO, new O FPs were formed to complete $(\text{MgO})_4$ clusters, whereas in UO_2 , new O FPs were formed perhaps to balance U defects. However, the complete mechanism is not known. In both materials, if the defects are present simultaneously on both sub-lattices, very few recombination events take place. In UO_2 , while the O vacancies form Schottky defects by forming $V_o^{\bullet\bullet} - U_i^{\prime\prime\prime} - V_o^{\bullet\bullet}$ clusters, oxygen interstitials form cuboctahedral clusters (COT). The oxygen vacancies' sequestration by uranium vacancies was found to be the mechanism of COT cluster

formation. Hence, this illustrated that in the presence of defects on U sub-lattice, new defects on O sub-lattice are created, thereby elucidating that U defects are the ones that caused damage to UO₂. The radiation tolerance of UO₂ can be enhanced by controlling defects on U sub-lattice.

10.2.4 Defect Annihilation in Nanocrystalline Mo

As mentioned above, the point-defect evolution profile can change dramatically in the presence of GBs. A simple monatomic bcc Mo was chosen as a model material to elucidate the evolution of point defects in the presence of GBs. The MD simulations were found to be able to capture the formation and elimination of defects from GBs, thus illustrating the source/sink nature of GBs. By inserting a high concentration of point defects, the source/sink strength of GBs was calculated. Further, while in single crystals, point-defect elimination is only by mutual recombination, in the nanocrystalline structure, the point defects could also eliminate at the GBs. It was found that for the studied temperature and grain size, point defect elimination by mutual recombination is more prevalent and GBs do not have much significant role.

10.3 Conclusions and Future Work

10.3.1 δ -Bi₂O₃

As discussed in Chapter 4, doping with lanthanides decreases conductivity of δ -Bi₂O₃ and results in the ordering of vacancies. In the δ -Bi₂O₃ literature, it appears that focus has been placed on improving the conductivity by engineering various strategies such as double doping or varying dopant concentration.¹⁶² Little has been said about the site preference of dopants, which, is known to be one of the most significant factors in achieving high conductivity, especially in pyrochlore materials.^{163,164} The crystal

structure of pyrochlore materials closely resembles that of fluorite materials. Hence, it can be expected that dopants could prefer particular sites like in pyrochlores.

In pyrochlore materials, for example, $\text{Gd}_2\text{Ti}_2\text{O}_7$, if both cations occupy their regular sites, oxygen diffusion is limited even upon the availability of intrinsic oxygen vacancies. However, in the presence of cation antisites, oxygen diffusion is enhanced due to the creation of new vacancies, $48f$, which facilitate oxygen diffusion through a $48f$ hopping mechanism.¹⁶³ While antisite formation and the associated hopping mechanisms are characteristic features of pyrochlore materials, the underlying mechanism of site preference, i.e., preference in $\langle 110 \rangle$ or $\langle 111 \rangle$ vacancy ordered oxygen sub-lattice, could be applicable to $\delta\text{-Bi}_2\text{O}_3$. The site preference of dopants is not known, neither from experiments nor simulations.

While $\delta\text{-Bi}_2\text{O}_3$ has been excluded from such investigations, other fluorite-based materials have been studied both experimentally and theoretically. The current understanding is that the site preference strongly depends on the size of the cation. In bixbyite materials, it was found that those cation dopants with radii smaller than the host cation occupy $24b$ sites, whereas, those with radii larger than host occupy $8a$ sites.^{165,166} These two Wyckoff sites are the same as the $\langle 110 \rangle$ and $\langle 111 \rangle$ vacancy-ordered Bi environments respectively. Recently, in $\delta\text{-Bi}_2\text{O}_3$, double doping has been used as viable option to achieve high conductivity while keeping dopant concentration to minimum.¹⁶² It remains to be seen, both in single-doped and double-doped $\delta\text{-Bi}_2\text{O}_3$, which sites the dopants prefer. Based on the above observation, one would expect dopants to occupy $\langle 110 \rangle$ vacancy ordered Bi site, as all dopants, except La, are smaller than Bi. In double doped system, even though the two dopants would compete for one site, one would still

expect both dopants to be accommodated in $\langle 110 \rangle$, in part because there are three times of these sites than $\langle 111 \rangle$ sites. This indicates that, regardless of dopant concentration, all dopants would occupy $\langle 110 \rangle$ sites. Keeping this in mind, it appears that in doped Bi_2O_3 experiments, the observation of loss in conductivity corresponds to materials with dopants sited at $\langle 110 \rangle$. If this is indeed the case, it can be speculated that, with dopants occupying $\langle 110 \rangle$ and Bi occupying $\langle 111 \rangle$ (recall covalent character bonding), one of the ways that conductivity might be enhanced could be by breaking such symmetrical structure, i.e., by adding dopants in $\langle 111 \rangle$ to create structural distortions. Under such an assumption, dopants of size bigger than Bi, may hold the key in breaking such the symmetry by sitting at $\langle 111 \rangle$. Computer simulations will be very useful to clarify this process.

However, it appears that physically realizing this mechanism may not be straightforward. The Bi^{3+} cation has an ionic radius of 131 pm^{16} which is the biggest among all of the dopants of valence +3. To add larger sized dopants than Bi, one might have to look for options other than just the widely used +3 smaller lanthanide dopants.

In addition to the above questions, there are still longstanding issues that are important to resolve in order to gain a complete understanding of $\delta\text{-Bi}_2\text{O}_3$. A preferential oxygen diffusion mechanism is known from experiments. However, it would be interesting to identify any difference in the vicinity of dopants. Lanthanide dopants have lower polarizabilities than Bi; an altered diffusion direction thus may not be ruled out.

Due to uncharged vacancies and charge-balanced cation site in doped Bi_2O_3 , association of vacancies due to charge imbalance is ruled out. However, the difference in

the size of the dopants to Bi would create stresses in the system. Therefore, the effect of stress on oxygen vacancies due to different dopant size can be understood in isolation.

10.3.2 Radiation Damage

In this work on UO_2 and MgO , evolution of irradiation-induced point defects was studied in single-crystal systems. The obvious next step is to understand their evolution in the presence of GBs and their coupling to microstructure. It can be expected that GBs will tend to maintain equilibrium concentration of point defects by acting as sources and sinks. Generally, while the concentration of interstitials is negligible due to their high formation energies, there is always a vacancy concentration in bulk. In UO_2 , the U vacancy formation and migration energies are relatively higher than their O counterparts. For the temperatures of interest (1000 -1600 K), U vacancy formation from GBs is not to be expected. By contrast, GBs can frequently form O vacancies and interstitials to maintain their equilibrium concentration. In irradiation-induced point defects, it was shown in Chapter 8 that O vacancies do not annihilate if U defects survive; instead they form Schottky defects by combining with U vacancies. Under high concentration of U point defects, O vacancies and interstitials easily exceed their equilibrium concentration. To maintain equilibrium concentration of defects, GBs may emit corresponding defects. Therefore, it is anticipated that three mechanisms could operate simultaneously, (a) formation of O interstitials from GBs to eliminate excess O vacancies, (b) drive for excess interstitials (clustered in COT) from bulk towards GBs. Through these mechanisms, GBs may drive for equilibrium concentration of O defects in the bulk. Depending upon the attempt frequency, GBs may also annihilate U defects, however, higher formation energies might limit that phenomenon. Meanwhile to maintain a high concentration of O defects, another mechanism may also prevail, i.e., (c) U defects

attempting to maintain fixed concentration of O defects. Hence, two competing mechanisms, point-defect annihilation driven by GBs and point-defect creation driven by U defects could prevail; understanding which one is dominant is essential.

In MgO, the presence of GBs is also expected to affect the dynamics of the system. Diffusing Mg and O interstitials form interstitial clusters, whereas, their counterpart vacancies are essentially immobile. In the presence of GBs, in pursuit of maintaining equilibrium concentration of defects, it can be speculated that GBs may emit both Mg and O interstitials into bulk for reducing the concentration of Mg and O vacancies. However, at this point, it is difficult to foresee the fate of the already formed interstitial clusters. Due to these speculations, it is very desirable to perform such studies, which are quite possible using computer simulations.

The role of GBs can be further understood during frequent damage of material. Frequent damage would create large number of defects, to compensate for which, GBs would more frequently act as sources or sinks. It needs to be determined that under such circumstances, is the ability of GBs to act as source/sink is limited? In other words, do GBs become saturated with defects?

Not all answers can be gained from experiments; therefore, simulations play a significant role in understanding radiation damage. Conventional radiation damage PKA-MD simulation however will be incapable in unraveling all. Besides, the large system sizes required, not only are PKA simulations highly time consuming, which limits observing such cluster formation, but they also require multiple trajectories of PKA to capture global defect behavior. They have not even been able to reveal complete point-defect evolution in single crystals, thus unraveling response of GBs alone from PKA

simulations will be an enormous task. In contrast, by using the methodology described in this work, with the point defect clustering already understood from single crystals, such clusters can now be easily adapted to polycrystalline materials. Hence, while the PKA simulation methodology appears to have limited value for single crystals, in polycrystalline materials, it may be completely useless.

Apart from the above obvious questions, there are some other less understood problems, which can be understood in combination with this study. The stability of COT clusters is not known clearly. Although it was speculated previously that with higher temperatures, the COT clusters might disintegrate,¹³⁰ there is absolutely no understanding on their long-time stability. While they have been observed to be stable on MD time scale, their stability on experimentally accessible time scale needs to be established.

The effect of non-stoichiometry is another standing issue. The evolution of point defects due to formation of U^{3+}, U^{5+} , in single crystals and later in polycrystals, needs to be understood. Further, there are stress and temperature gradients inside the nuclear reactor. A complete understating of evolution of point defects, or clusters, under gradients is also lacking.

Similarly, deformation of the material under irradiation needs to be addressed. Deformation studies on un-irradiated UO_2 have been performed recently and creep mechanism has been understood.¹³⁴ It will be interesting to observe any significant change in deformation mechanism in the radiated UO_2 .

Finally, atomistic studies should be able to provide information to mesoscale level simulation methods such that evolution of large-sized defects such as voids and gas bubbles can be understood in the irradiated UO_2 .

LIST OF REFERENCES

-
- ¹ International Energy Agency (Key World Energy Statistics, IEA, Paris, 2006).
- ² Energy Information Administration (U.S. Department of Energy, International Energy Annual, Washington D.C., 2005).
- ³ V. S. Arunachalam and E. L. Fleischer, *MRS Bulletin* **33**, 264 (2008).
- ⁴ M. S. Dresselhaus, G. W. Crabtree and M. V. Buchanan, *MRS Bulletin* **30**, 518 (2005).
- ⁵ V. Vaitheeswaran, I. Carson, *Zoom: The Global Race to Fuel the Car of the Future* (Twelve Publishing, 2007).
- ⁶ D. M. Etheridge, L. P. Steele, R. L. Langenfelds and R. J. Francey, *Journal of Geophysical Research-Atmospheres* **101**, 4115 (1996).
- ⁷ The Intergovernmental Panel on Climate Change, (IPCC Fourth Assessment Report, AR4, IPCC, 2007).
- ⁸ G. A. Meehel, W. M. Washington, W. D. Collins, J. M. Arblaster, A. Hu, L. E. Buja, W. G. Strand and H. Teng, *Science* **307**, 1769 (2005).
- ⁹ J. A. Turner, *Science* **285**, 687 (1999).
- ¹⁰ Intergovernmental Panel on Climate Change, *Special Report on Carbon Dioxide Capture and Storage* (Cambridge University Press, Cambridge, 2005).
- ¹¹ L. B. Lave, *MRS Bulletin* **33**, 291 (2008).
- ¹² B. Hayman, J. W. Heinen and P. Brøndsted, *MRS Bulletin* **33**, 343 (2008).
- ¹³ D. Ginley, M. A. Green and R. Collins, *MRS Bulletin* **33**, 355 (2008).
- ¹⁴ *MRS Bulletin*, Special Issue April **33**, (2008).
- ¹⁵ Y. Chimi, A. Iwase, N. Ishikawa, A. Kobiyama, T. Inami and S. Okuda, *Journal of Nuclear Materials* **297**, 355 (2001).
- ¹⁶ M. W. Barsoum, *Fundamentals of Ceramics*, (Institute of Physics Publishing, Philadelphia, 2003).
- ¹⁷ D. R. Askeland and P. P. Phule, *The Science and Engineering of Materials*, (Fourth Edition, Thompson, USA, 2003).
- ¹⁸ T. Hahn, *International Tables for Crystallography Volume A* (Springer, Fifth Edition, Boston, 2002).

-
- ¹⁹ W. A. Goddard III, *Handbook of Materials Modeling*, Edited by S. Yip, 2707 (Springer, Netherlands, 2005).
- ²⁰ J. Lemaitre, *Journal of Engineering Materials and Technology- Transactions of the ASME* **107**, 83 (1985).
- ²¹ J. W. Evans, *Handbook of Materials Modeling*, Edited by S. Yip, 1753 (Springer, Netherlands, 2005).
- ²² L. Q. Chen, *Annual Reviews of Materials Research* **32**, 113 (2002).
- ²³ Y. Mishin, *Handbook of Materials Modeling*, Edited by S. Yip, 459 (Springer, Netherlands, 2005).
- ²⁴ J. D. Gale, *Handbook of Materials Modeling*, Edited by S. Yip, 479 (Springer, Netherlands, 2005).
- ²⁵ A. D. Mackerell, *Handbook of Materials Modeling*, Edited by S. Yip, 509 (Springer, Netherlands, 2005).
- ²⁶ C. J. Cramer, *Essentials of Computational Chemistry - Theories and Models* (Wiley, UK, 2005).
- ²⁷ L. Verlet, *Physical Review* **159**, 98 (1967).
- ²⁸ R. W. Hockney, *Methods in Computational Physics* **9**, 136 (1970).
- ²⁹ D. Potter, *Computational Physics* (Wiley, New York, 1972).
- ³⁰ D. Beeman, *Journal of Computational Physics* **20**, 130 (1976).
- ³¹ C. Gear, *Numerical Initial Value Problems in Ordinary Differential Equation* (Prentice-Hall, Englewood Cliffs, NJ, 1971).
- ³² T. Schlick, *Molecular Modeling and Simulation* (Springer, Berlin, 2002)
- ³³ M. E. Tuckerman and G. J. Martyna, *Journal of Physical Chemistry B* **104**, 159 (2000).
- ³⁴ M. P. Allen and D. J. Tildesley, *Computer Simulations of Liquids* (Oxford University Press, Oxford, 1987).
- ³⁵ J. Li, *Handbook of Materials Modeling*, Edited by S. Yip, 565 (Springer, Netherlands, 2005).
- ³⁶ C. A. Coulson, *Nature* **195**, 744 (1962).
- ³⁷ S. Khan, M. Islam and D. R. Basetb, *Journal of Materials Chemistry* **8**, 2299 (1998).

-
- ³⁸ D. Wolf, P. Keblinski, S. R. Phillpot, J. Eggebrecht, *Journal of Chemical Physics* **110**, 8254 (1999).
- ³⁹ J. E. Lennard-Jones, *Proceedings of Royal Society* **106**, 441, 463, 709 (1924).
- ⁴⁰ J. E. Lennard-Jones, *Proceedings of Royal Society* **109**, 476 (1925).
- ⁴¹ R. A. Buckingham, *Proceedings of Royal Society A* **168**, 264 (1938).
- ⁴² F. London, *Transactions of the Faraday Society* **33**, 8 (1937).
- ⁴³ B. G. Dick and A. W. Overhauser, *Physical Review* **112**, 90 (1958).
- ⁴⁴ H. C. Andersen, *Journal of Chemical Physics* **72**, 2384 (1977).
- ⁴⁵ M. Parrinello and A. Rahman, *Journal of Applied Physics* **52**, 7182 (1981).
- ⁴⁶ M. Parrinello and A. Rahman, *Physical Review Letters* **45**, 1196 (1980).
- ⁴⁷ M. Parrinello and A. Rahman, *Journal of Chemical Physics* **76**, 2662 (1982).
- ⁴⁸ S. Nosé, *Molecular Physics* **52**, 255 (1984).
- ⁴⁹ H. J. C. Berendsen, J. P. M. Postma, W. F. Vangunsteren, A. Dinola and J. R. Haak, *Journal of Chemical Physics* **81**, 3684 (1984).
- ⁵⁰ S. A. Adelman, J. D. Doll, *Journal of Chemical Physics* **64**, 2375 (1976).
- ⁵¹ S. Nosé, *Journal of Chemical Physics* **81**, 511 (1984).
- ⁵² H. J. C. Berendsen, J. P. M. Postma and W. F. Vangunsteren, *Journal of Chemical Physics* **81**, 3684 (1984).
- ⁵³ J. Skinner and J. Kilner, *Materials Today* **3**, 30 (2003).
- ⁵⁴ T. H. Etsell and S. N. Flengas, *Chemical Reviews* **70**, 339 (1970).
- ⁵⁵ N. J. Maskalick and C. C. Sun, *Journal of Electrochemical Society* **118**, 1386 (1971).
- ⁵⁶ H. Inaba and H. Tagawa, *Solid State Ionics* **83**, 1 (1996).
- ⁵⁷ S. Omar, *Enhanced Ionic Conductivity of Cerai-Based Compounds for the electrolyte Applications in SOFCs* (Dissertation, University of Florida, 2008).
- ⁵⁸ J. W. Fergus, *Journal of Power Sources* **162**, 30 (2006).
- ⁵⁹ T. Takahashi, H. Iwahara and T. Arao, *Journal of Applied Electrochemistry* **5**, 187 (1975).

-
- ⁶⁰ D. M. Smyth, *The Defect Chemistry of Metal Oxides* (Oxford University Press, New York, 2000).
- ⁶¹ A. Bogicevic and C. Wolverton, *Physical Review B* **67**, 024106 (2003).
- ⁶² N. Jiang, E. D. Wachsman and S. H. Jung, *Solid State Ionics* **150**, 347 (2002).
- ⁶³ N. Sammes, G. A. Tompsett, H. Näfe and F. Aldinger, *Journal of European Ceramic Society* **19**, 1901 (1999).
- ⁶⁴ B. Aurivillius and L. G. Sillen, *Nature* **155**, 305 (1945).
- ⁶⁵ C. N. R. Rao, G. V. S. Rao and S. Ramdas, *Journal of Physical Chemistry* **73**, 672 (1969).
- ⁶⁶ N. Jiang and E. D. Wachsman, *Journal of the American Ceramic Society* **82**, 3057 (1999).
- ⁶⁷ E. D. Wachsman, S. Boyapati and N. Jiang, *Ionics* **7**, 1 (2001).
- ⁶⁸ P. W. M. Jacobs and D. A. Mac Dönaill, *Solid State Ionics* **23**, 279 (1987).
- ⁶⁹ R. D. Shannon, *Acta Crystallographica A* **32**, 751 (1976).
- ⁷⁰ K. Shirao, T. Iida, K. Fukushima and Y. Iwodate, *Journal of Alloys and Compounds* **281**, 163 (1998).
- ⁷¹ R. D. Shannon, *Journal of Applied Physics* **70**, 348 (1993).
- ⁷² S. Boyapati, E. D. Wachsman and B. C. Chakoumakos, *Solid State Ionics*, **138**, 293 (2001).
- ⁷³ S. Boyapati, E. D. Wachsman and N. Jiang, *Solid State Ionics* **140**, 149 (2001).
- ⁷⁴ B. T. M. Willis, *Acta Crystallographica* **18**, 75 (1965).
- ⁷⁵ E. D. Wachsman, S. Boyapati, M. J. Kauffman and N. Jiang, *Journal of the American Ceramic Society* **83**, 1964 (2000).
- ⁷⁶ A. Walsh, G. W. Watson, D. J. Payne, R. G. Edgell, J. H. Guo, P. Glans, T. Learmonth and K. E. Smith, *Physical Review B* **73**, 235104-1 (2006).
- ⁷⁷ G. Kreese and J. Hafner, *Physical Review B* **49**, 14251 (1994).
- ⁷⁸ G. Kreese and J. Furthmuller, *Computational Materials Science* **6**, 15 (1996).
- ⁷⁹ G. Kreese and J. Furthmuller, *Physical Review B* **54**, 11169 (1996).

-
- ⁸⁰ J. P. Perdew and Y. Wang, *Physical Review B* **45**, 13244 (1992).
- ⁸¹ P. E. Blochl, *Physical Review B* **50**, 17953 (1994).
- ⁸² H. A. Harwig and A. G. Gerards, *Thermochemica Acta* **28**, 121 (1979).
- ⁸³ N. I. Medvedeva, V. P. Zhukov, V. A. Gubanov, D. L. Novikov and B. M. Klein, *Journal of Physics and Chemistry of Solids* **57**, 1243 (1996).
- ⁸⁴ P. D. Battle, C. R. A. Catlow, J. Drennan and A. D. Murray, *Journal of Physics C: Solid State Physics* **16**, L561 (1983).
- ⁸⁵ G. Henkelman, A. Arnaldsson, and H. Jonsson, *Computational Materials Science* **36**, 254 (2006).
- ⁸⁶ E. Sanville, S. D. Kenny, R. Smith, and G. Henkelman, *Journal of Computational Chemistry* **28**, 899 (2007).
- ⁸⁷ A. Laarif and F. Theobald, *Solid State Ionics* **21**, 183 (1986).
- ⁸⁸ F. S. Galasso, *Structure and Properties of Inorganic Solids* (Pergamon, Oxford, 1970).
- ⁸⁹ D. S. Aidhy, S. B. Sinnott, E. D. Wachsman, S. R. Phillpot and J. C. Nino, *Journal of the American Ceramic Society* **91**, 2349 (2008).
- ⁹⁰ P. D. Battle, C. R. A. Catlow, and L. M. Moroney, *Journal of Solid State Chemistry* **67**, 42 (1987).
- ⁹¹ D. J. M Bevan and R. L. Martin, *Journal of Solid State Chemistry* **181**, 2250 (2008).
- ⁹² P. D. Battle, C. R. A. Catlow, J. W. Heap, and L. M. Moroney, *Journal of Solid State Chemistry* **63**, 8 (1986).
- ⁹³ D. S. Aidhy, S. B. Sinnott, E. D. Wachsman, S. R. Phillpot and J. C. Nino, *Journal of Solid State Chemistry*, doi:10.1016/j.jssc.2009.02.019, (2009)
- ⁹⁴ E. Rutherford, *Radioactivity in The Encyclopedia Britannica* (The Encyclopedia Britannica Company, New York, Eleventh Edition, 1910).
- ⁹⁵ World Association of Nuclear Operators, *Performance Indicators* (London, UK, 2006).
- ⁹⁶ R. Ewing, W. Weber and J. Lian, *Applied Physical Reviews* **95**, 5949 (2004).
- ⁹⁷ R. Ewing, *The Canadian Mineralogist* **43**, 2099 (2005).
- ⁹⁸ I. Farhan, H. Cho and W. J. Weber, *Nature* **445**, 190 (2007).

-
- ⁹⁹ K. E. Sickafus, L. Minervini, R. W. Grimes, J. A. Valdez, M. Ishimaru, F. Li, K. J. McClellan and T. Hartmann, *Science* **289**, 748 (2000).
- ¹⁰⁰ J. A. Angelo, *Nuclear Technology* (Greenwood Press, Connecticut, 2004).
- ¹⁰¹ D. Bodansky, *Nuclear Energy – Principles, Practices, and Prospects* (Springer, New York, 2004).
- ¹⁰² Hj. Matzke, P.G. Lucuta and T. Wiss, *Nuclear Instruments and Methods in Physics Research Section B* **166-167**, 920 (2000).
- ¹⁰³ W.J. Weber, R. C. Ewing, C. R. Catlow, T. D. de la Rubia, L. W. Hobbs, C. Kinoshita, Hj. Matzke, A. T. Motta, M. Nastasi, E. K. H. Salje, E. R. Vance and S. J. Zinkle, *Journal of Materials Research* **13**, 1434 (1998).
- ¹⁰⁴ M. T. Robinson and I. M. Torrens, *Physical Review B* **9**, 5008 (1974).
- ¹⁰⁵ R. Stoller, *Journal of Materials-Journal of Minerals Metals and Materials Society* **48**, 23 (1996).
- ¹⁰⁶ T. D. de la Rubia, H. M. Zbib, T. A. Kharaiishi, B. D. Wirth, M. Victoria and M. J. Caturla, *Nature* **406**, 24 (2000).
- ¹⁰⁷ B.P. Uberuaga, R. Smith, A.R. Cleave, F. Montalenti, G. Henkelman, R.W. Grimes, A.F. Voter and K.E. Sickafus, *Physical Review Letters* **92**, 115505 (2004).
- ¹⁰⁸ Y. Matsukawa and S.J. Zinkle, *Science* **318**, 959 (2007).
- ¹⁰⁹ D.J. Bacon and T.D. de la Rubia, *Journal of Nuclear Materials* **216**, 275 (1994).
- ¹¹⁰ B.P. Uberuaga, R. Smith, A.R. Cleave, G. Henkelman, R.W. Grimes, A.F. Voter and K.E. Sickafus, *Physical Review B* **71**, 104102 (2005).
- ¹¹¹ L.V. Brutzel, J.M. Delaye, D. Ghaleb, *Philosophical Magazine* **21**, 4083 (2003).
- ¹¹² G. V. Lewis and C. R. A. Catlow, *Journal of Physics C* **18**, 1149 (1985).
- ¹¹³ R. Ferneyhough, D. Fincham, G. D. Price and M. J. Gillan, *Modelling and Simulation in Materials Science And Engineering* **2**, 1101 (1994).
- ¹¹⁴ C. J. Meechan and J. A. Brinkman, *Physical Review* **103**, 1193 (1956).
- ¹¹⁵ D. Wolf, *Physical Review Letters* **68**, 3315 (1992).
- ¹¹⁶ M. Gajdaraziaka-Josifovska, R. Plass, M. A. Schofield, D. R. Giese, R. Sharma, *Journal of Electron Microscopy* **51**, S13 (2002).

-
- ¹¹⁷ F. Finocchi, A. Barbier, J. Jupille, C. Noguera, *Physical Review Letters* **92**, 136101 (2004).
- ¹¹⁸ D. S. Aidhy, P.C. Millett, D. Wolf and S.R. Phillpot, (unpublished).
- ¹¹⁹ E. Vincent, C.S. Becquart, C. Domain, *Nuclear Instruments and Methods in Physics Research Section B* **255**, 78 (2007).
- ¹²⁰ F. Soisson, *Journal of Nuclear Materials* **349**, 235 (2005).
- ¹²¹ W. J. Pythian, R. E. Stoller, A. J. E. Foreman, A. F. Calder and D. J. Bacon, *Journal of Nuclear Materials* **223**, 245 (1995).
- ¹²² D. R. Olander, *Fundamental Aspects of Nuclear Reactor Fuel Elements*, (Technical Information Center, 1976).
- ¹²³ Hj. Matzke and J. L. Whitton, *Canadian Journal of Physics* **44**, 995 (1966).
- ¹²⁴ Hj. Matzke, *Radiation Effects* **64**, 3 (1982).
- ¹²⁵ W. J. Weber, *Radiation Effects and Defects in Solids* **83**, 145 (1984).
- ¹²⁶ L. V. Brutzel and M. Rarivomanantsoa, *Journal of Nuclear Materials* **358**, 209 (2006).
- ¹²⁷ L. V. Brutzel and E. Vincent-Aublant, *Journal of Nuclear Materials* **377**, 522 (2008).
- ¹²⁸ B. T. M. Willis, *Acta Crystallographica* **A34**, 88 (1978).
- ¹²⁹ D. J. M. Bevan, I. E. Grey and B. T. M. Willis, *Journal of Solid State Chemistry* **61**, 1 (1986).
- ¹³⁰ R. I. Cooper and B. T. M. Willis, *Acta Crystallographica* **A60**, 322 (2004).
- ¹³¹ D. S. Aidhy, P. C. Millett, D. Wolf, S. R. Phillpot and H. Huang, *Scripta Materialia*, **60**, 691 (2009).
- ¹³² Y. Ida, *Physics of the Earth Planetary Interiors* **13**, 97 (1976).
- ¹³³ C. B. Basak, A. K. Sengupta and H. S. Kamath, *Journal of Alloys and Compounds* **360**, 210 (2003).
- ¹³⁴ T. G. Desai, P. C. Millett and D. Wolf, *Acta Materialia* **56**, 4489 (2008).
- ¹³⁵ R. A. Hein and P. N. Flagella, GEMP-578. Schenectady: General Electric Company (1968).
- ¹³⁶ J. P. Hiernaut, G. J. Hyland and C. Ronchi, *International Journal of Thermophysics* **14**, 259 (1993).

-
- ¹³⁷ J. Ralph, J. Chem. Soc., Faraday Transactions II **87**, 1253 (1987).
- ¹³⁸ A. D. Murray and B. T. M. Willis, Journal of Solid State Chemistry **84**, 52 (1990).
- ¹³⁹ H. Y. Geng, Y. Chen and Y. Kaneta, Physical Review B **77**, (2008) 180101 (R).
- ¹⁴⁰ D. A. Anderson, J. Lezama, B. P. Uberuaga, C. Deo and S. D. Conradson, Physical Review B **79**, 024110 (2009).
- ¹⁴¹ K. Govers, S. Lemehov, M. Hou and M. Verwerft, Journal of Nuclear Materials **366**, 161 (2007).
- ¹⁴² R.M. German, *Sintering Theory and Practice* (John Wiley, New York, 1996).
- ¹⁴³ I.M. Robertson, R.S. Averback, D.K. Tappin and L.E. Rehn, Journal of Nuclear Materials **216**, 1 (1994).
- ¹⁴⁴ N.V. Doan and G. Martin: Physical Review B **67**, 134107 (2003).
- ¹⁴⁵ C.A. Volkert, *Encyclopedia of Materials: Science and Tech.* (Elsevier, 2001).
- ¹⁴⁶ D. J. Bacon, Journal of Nuclear Materials **323**, 152 (2003).
- ¹⁴⁷ Y. N. Osetsky, D. J. Bacon and A. Serra, Philosophical Magazine Letters **79**, 273 (1999).
- ¹⁴⁸ M. Samaras, P. M. Derlet, H. Swygenhoven and M. Victoria, Philosophical Magazine **83**, 3599 (2003).
- ¹⁴⁹ L. Malerba, C.S. Becquart and C. Domain, Journal of Nuclear Materials **360**, 159 (2007).
- ¹⁵⁰ P.C. Millett, T. Desai, V. Yamakov and D. Wolf, Acta Materialia **56**, 3688 (2008).
- ¹⁵¹ G.L. Ackland and R. Thetford, Philosophical Magazine A **56**, 15 (1987).
- ¹⁵² J.M. Harder and D.J. Bacon, Philosophical Magazine A **54**, 651 (1986).
- ¹⁵³ K. Maier, M. Peo, B. Saile, H.E. Schaefer and A. Seeger, Philosophical Magazine A **40**, 701 (1979).
- ¹⁵⁴ S.R. Phillpot, J.F. Lutsko, D. Wolf and S. Yip, Physical Review B **40** 2831 (1989).
- ¹⁵⁵ J. R. Manning, *Diffusion Kinetics for Atoms in Crystals* (Van Nostrand, Princeton, 1968).
- ¹⁵⁶ N. Soneda and T. Diaz de la Rubia, Philosophical Magazine A **78**, 995 (1998).

-
- ¹⁵⁷ J.D. Honeycutt and H.C. Andersen, *Journal of Physical Chemistry* **91** 4950 (1987).
- ¹⁵⁸ A. P. Sutton and R. W. Balluffi, *Interfaces in Crystalline Materials* (Clarendon Press, Oxford, 1995).
- ¹⁵⁹ A.D. Brailsford and R. Bullough, *Philosophical Transactions of The Royal Society of London Series A* **302**, 87 (1981).
- ¹⁶⁰ R.W. Siegel, *Journal of Nuclear Materials* **69&70**, 117 (1978).
- ¹⁶¹ T.R. Waite, *Physical Review* **107**, 463 (1957).
- ¹⁶² S. H. Jung, E. D. Wachsman and N. Jiang, *Ionics* **8**, 210 (2002).
- ¹⁶³ P. J. Wilde and C. R. A Catlow, *Solid State Ionics* **112**, 173 (1998).
- ¹⁶⁴ L. Minervini, R. W. Grimes and K. E. Sickafus, *Journal of the American Ceramic Society* **83** 1873 (2000).
- ¹⁶⁵ C. R. Stanek, K. J. McClellan, B. P. Uberuaga, K. E. Sickafus, M. R. Levy and R. W. Grimes, *Physical Review B* **75**, 134101 (2007).
- ¹⁶⁶ C. R. Stanek, K. J. McClellan, M. R. Levy and R. W. Grimes, *IEEE Transactions on Nuclear Science* **55**, 1492 (2008).

BIOGRAPHICAL SKETCH

Dilpuneet Singh Aidhy was born in 1982 at Rajpura, Punjab, India. He received his B. E. degree in metallurgical engineering from Punjab Engineering College, Chandigarh, India in 2004. He joined the Department of Materials Science and Engineering at University of Florida in Fall 2004 to pursue his Ph.D. with Prof. Simon R. Phillpot. During his graduate studies, he interned at Idaho National Laboratory for one year where he worked with Dr. Dieter Wolf. Dilpuneet is expecting his PhD in the spring of 2009 and has accepted a post-doctoral position at the Department of Materials Science and Engineering at Northwestern University.